Selected results on heavy flavour physics at LHCb

Matthew Charles

Selected results on heavy flavour physics at LHCb

Matthew Charles
LPNHE, UPMC, 4 place Jussieu, Paris.

June 29, 2016

Soutenance : le 10 June 2016

Jury :
- Jean-Bernard ZUBER (Président)
- François LE DIBERDER (Rapporteur)
- Yosef NIR (Rapporteur)
- Antimo PALANO (Rapporteur)
- Adrian BEVAN
- Tim GERSHON

Contents

1 Introduction **1**
- 1.1 Overview . . . 1
- 1.2 The LHCb detector . . . 2

2 Searches for *CP* violation in charm **4**
- 2.1 The origin of *CP* violation in the Standard Model . . . 4
- 2.2 Direct *CP* violation . . . 5
- 2.3 Mixing and indirect *CP* violation in charm . . . 7
  - 2.3.1 Mixing . . . 7
  - 2.3.2 Indirect CPV . . . 9
- 2.4 Phenomenology of direct CPV in charm . . . 11
- 2.5 Search for CPV in $D^+ \to K^-K^+\pi^+$ . . . 12
  - 2.5.1 Introduction . . . 12
  - 2.5.2 Analysis strategy . . . 14
  - 2.5.3 Data, binning, and expected sensitivity . . . 17
  - 2.5.4 Results in control samples . . . 19
  - 2.5.5 Results . . . 20
- 2.6 Search for CPV in $D^0 \to K^-K^+, \pi^-\pi^+$ (ΔA_{CP}) . . . 23
  - 2.6.1 Introduction and formalism . . . 23
  - 2.6.2 Kinematic binning and reweighting . . . 26
  - 2.6.3 Reconstruction and Selection . . . 27
  - 2.6.4 Fit procedure and results . . . 29
  - 2.6.5 Systematic uncertainties and checks . . . 33
  - 2.6.6 Conclusions . . . 34
  - 2.6.7 Afterword . . . 36
- 2.7 Other analyses of interest . . . 36
- 2.8 Summary and outlook . . . 37

3 Heavy baryon spectroscopy **38**
- 3.1 Introduction . . . 38
  - 3.1.1 Overview . . . 38
  - 3.1.2 Quark model for ground states . . . 38
  - 3.1.3 Higher states . . . 42
- 3.2 Search for Ξ_b^- resonances . . . 43
  - 3.2.1 Introduction . . . 43
  - 3.2.2 Reconstruction and selection . . . 44
  - 3.2.3 Fit to the δm spectrum . . . 45
  - 3.2.4 Systematic uncertainties and cross-checks for the δm fit . . . 47
  - 3.2.5 Angular analysis . . . 48
  - 3.2.6 Relative production rates . . . 50
  - 3.2.7 Feed-down mechanism . . . 51

3.2.8 Conclusions . . . 52
3.2.9 Afterword: Ξ_b^{*0} . . . 52
3.3 Search for Ξ_{cc}^+ . . . 52
3.3.1 Introduction and background . . . 52
3.3.2 Analysis overview . . . 54
3.3.3 Reconstruction and selection . . . 54
3.3.4 Fit to the Λ_c^+ normalisation mode . . . 55
3.3.5 Ξ_{cc}^+ yield determination method . . . 55
3.3.6 Efficiency calculation and systematic uncertainties . . . 57
3.3.7 Significance and upper limit procedures . . . 60
3.3.8 Results . . . 60
3.3.9 Conclusions . . . 61
3.4 Summary and outlook . . . 64

4 Outlook **65**
4.1 Machine and detector status . . . 65
4.2 Key LHCb results . . . 66
4.3 The longer term . . . 67
4.4 Perspectives at LPNHE . . . 68

A Acknowledgement of collaborators **70**

B Extra material **71**
B.1 Ξ_b feed-down . . . 71

Chapter 1

Introduction

1.1 Overview

At the time of writing, Particle Physics is at a very interesting juncture. Over the past 40 years the story of our field has been the triumph of the Standard Model (SM), which has successfully predicted or explained almost all laboratory data. At the same time, though, it has become increasingly clear that the SM is only an approximation and is missing key components. The list of "known unknowns" is now extensive: the origin of neutrino masses, dark matter, dark energy, the matter-antimatter asymmetry of the universe, the hierarchy problem (and of course gravity). While numerous theories of new physics (NP) beyond the SM have been proposed, there has been as yet no compelling experimental observation that vindicates a particular theory or class of theories. The main goal of our field at present is to establish the existence and nature of this NP.

Broadly speaking, there are two main approaches. One is to carry out direct searches for on-shell NP particles. Since we have not yet observed them, such particles must be either too heavy to have been produced in previous experiments, or have couplings to SM particles that are too small for them to have been produced and detected. Several popular theories of NP, notably SuperSymmetry (SUSY), require the existence of a spectrum of heavy particles, with masses in the TeV range often being favoured[1]. To search for such particles requires an efficient, precise detector at a high-energy, high-luminosity collider. This is the main motivation behind the ATLAS and CMS general-purpose detectors at the Large Hadron Collider (LHC).

A second approach is to make indirect tests, measuring observables that could plausibly be affected by the presence of NP and for which the SM value is well predicted, so that a deviation from the SM value would be evidence for NP. The nature of such deviations (or, inverting the argument when observables are found to be consistent with the SM, the lack of them) in general constrain the parameter space available to NP models and in some cases[2] exclude them entirely. Since virtual particles may contribute to Feynman diagrams even when far off-shell, an important advantage of this approach is that the effects of heavy new particles may be seen at energy scales much lower than their mass. Thus, the LHC can have sensitivity to NP even if the NP mass spectrum begins above the LHC centre-of-mass (CM) energy.

The main focus of the LHCb experiment is on this second, indirect class of searches for NP—and, more specifically, on studies of heavy flavour physics. There is a wide range of measurements that can be made with b- and c-hadrons, but most of those with sensitivity to NP fall into one of two categories: measurements of CP violation (CPV), or measurements of very rare decays. This document will describe results from certain CPV studies.

In addition, there are a variety of analyses in heavy flavour physics (and beyond, e.g. forward electroweak) at LHCb that are not directly sensitive to NP but are of interest nonetheless—both

[1] Though this feature is not universal, e.g. axions are predicted to be much lighter [1, 2].

[2] For example, the recent BABAR results on $\overline{B} \to D^{(*)}\tau^-\overline{\nu}_\tau$ are inconsistent with any type II two Higgs doublet model [3].

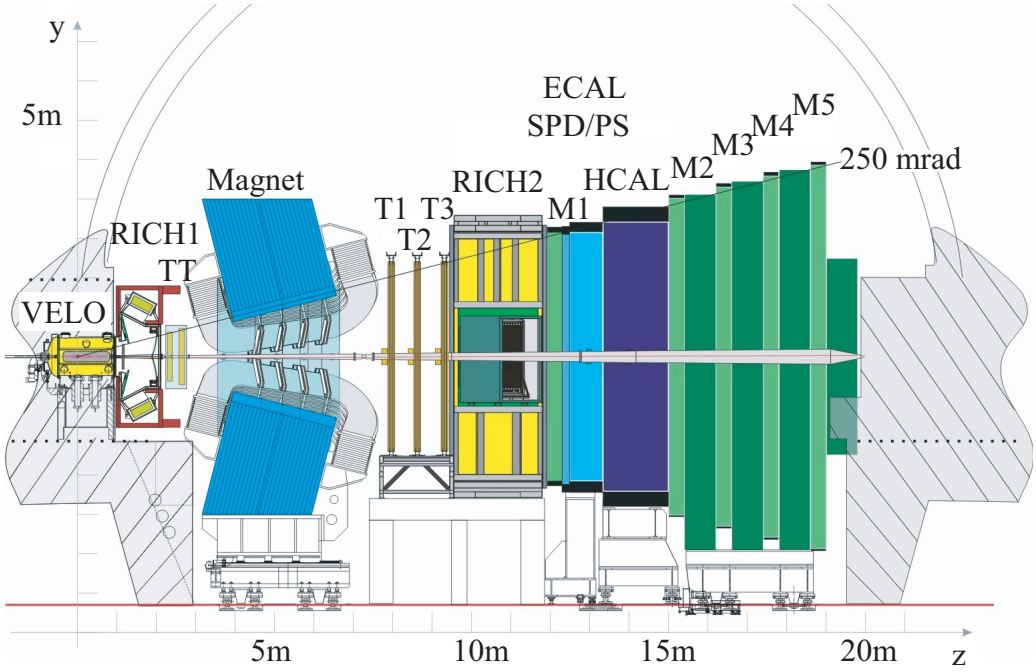

Figure 1.1: Side view of the LHCb detector.

in and of themselves, and often also because they improve our understanding of the experimental or phenomenological environment. For example, it is directly useful for LHCb analyses to measure hadron production asymmetries, since they are difficult to calculate from first principles and can contaminate time-integrated measurements of CP asymmetries. More broadly, measurements of quantities such as mass splittings in hadron spectra can be used as constraints or inputs for phenomenlogical models of QCD and lattice calculations. This document will describe two recent results in baryon spectroscopy.

1.2 The LHCb detector

All of the analyses presented in this document were carried out with data taken at LHCb. I will not describe the detector in detail here, since there are existing publications on the detector as a whole [4, 5] and on its subsystems and their performance [6, 7, 8, 9, 10, 11, 12]. A short guide follows for those who are unfamiliar with it.

LHCb is a single-arm spectrometer, instrumenting the forward region (approximate pseudorapidity range $2 < \eta < 5$) at interaction point 8 of the LHC. The detector is illustrated in Fig. 1.1, with the interaction region at $z = 0$. From left (innermost) to right (outermost), the detector subsystems are: the silicon microstrip vertex detector (VELO), the first ring imaging Cherenkov detector with C_4F_{10} and aerogel radiators (RICH1), the upstream silicon tracking stations (TT), the dipole magnet with an integrated field of 4Tm, the downstream tracking stations (T1–T3) which are equipped with silicon strips in the inner region (IT) and straw tubes in the outer region (OT), the second RICH detector with a CF_4 radiator (RICH2), the first muon station with multi-wire proportional chambers and triple gas electron multipliers (M1), the calorimeter system consisting of scintillating pad detectors (SPD), a preshower detector (PS), electromagnetic (ECAL) and hadronic (HCAL) calorimeters, and the remaining muon stations (M2–M5).

The detector is, in short, a fully equipped general-purpose detector—but covering the forward instead of the central region. This design is natural for a heavy flavour experiment at a high-energy collider. It is not a coincidence that the layout resembles that of a fixed-target experiment: the most probable way for a $b\bar{b}$ or $c\bar{c}$ pair to be produced in the initial pp collision is from the interaction of one

hard and one soft parton, so that the resulting b- or c-hadrons are produced with a large forward (or backward) boost. Compared with the ATLAS and CMS detectors, LHCb puts a greater emphasis on charged particle tracking and identification. The momentum resolution is approximately 0.5% for the range 2–100 GeV/c, and the VELO provides an impact parameter resolution of approximately 20 μm for high-$p_{\rm T}$ tracks, with the latter being important both for time-dependent measurements and for separating products of b/c-hadron decays from the more copious prompt tracks that originate at the event primary vertex. Hadron identification from the RICH systems provides kaon-pion[3] separation for tracks from a few GeV/c up to around 100 GeV/c. On the other hand, the calorimeter energy resolution is not competitive with that of ATLAS and CMS—especially the hadronic calorimeter, which is almost only used in the hardware trigger.

LHCb's trigger is central to the operation of the detector. It consists of a hardware stage known as Level 0 (L0) followed by a software stage known as the Higher Level Trigger (HLT). L0 operates at the LHC 40 MHz clock and must reduce the bandwidth to 1 MHz, which is the maximum readout rate that can be sustained with the present DAQ electronics. Only very limited information can be used at this stage (mainly $E_{\rm T}$ in the calorimeters and $p_{\rm T}$ in the muon system, plus hit counts in certain silicon subdetectors), so the trigger algorithms are of necessity very simple. In the HLT, however, more time is available and the reconstruction quality is not far from that used offline. In HLT2, in particular, full track vertexing and even RICH pattern recognition can be used. For many b-hadron decays, an inclusive trigger based on a sophisticated partial reconstruction strategy and multivariate selector is typically used. Charm triggers have to be more selective because of the very high production cross-section, and generally require a fully reconstructed decay of the appropriate final state[4].

[3] The threshold for Cherenkov radiation of kaons in C_4F_{10} is 9.3 GeV/c. Below this momentum there is in principle information from the aerogel, but in practice most of the discriminating power comes from the *absence* of photon hits which would be present for a pion. The pion threshold in C_4F_{10} is about 2.6 GeV/c, comparable to the momentum needed to traverse the dipole magnet without being swept out of the acceptance.

[4] An inclusive trigger for decays of the form $D^{*+} \to D^0\pi$, $D^0 \to h^+h'^-X$ was used for part of the 2012 data, where h is any track and X represents zero or more additional particles not used in the trigger reconstruction.

Chapter 2

Searches for *CP* violation in charm

In this chapter I will discuss the results of a few analyses at LHCb, each of which consists of a search for CPV in the decays of charmed hadrons, and each of which I worked on as one of the main authors. They are part of LHCb's broader programme of charm physics, which I helped lead as convenor of the Charm *CP* & Mixing subgroup (2010–2012) and as convenor of the Charm working group (2012–2014). To set the stage, the chapter begins with a summary of the origin of *CP* violation in the quark sector in the SM (Sec. 2.1), followed by a brief discussion of the theory expectations for CPV in charm (Sec. 2.2, 2.3, and 2.4). We then dive into the analyses, first with a search for CPV in the phase space of $D^+ \to K^-K^+\pi^+$ in Sec. 2.5, and then a study of the decays $D^0 \to K^-K^+$ and $D^0 \to \pi^-\pi^+$ in Sec. 2.6 using the ΔA_{CP} technique to search for CPV. I will mention in passing a few other analyses that I worked on in Sec. 2.7, then finally summarise the current state of play in Sec. 2.8, commenting on what we have learned from the LHCb charm data and what we might expect for the near future.

2.1 The origin of *CP* violation in the Standard Model

A brief overview of the origin of CPV is given below. For more detail on the formalism, the reader is encouraged to consult one of the many CPV primers which may be found, *e.g.* in [13].

In the SM, the $SU(2)$ weak interaction couples only to left-handed fermions. Each generation of quarks can therefore be represented as a doublet of left-handed particles (which can be transformed into one another via $SU(2)$ interactions) and two singlets of right-handed particles. The quarks in the three doublets are weak flavour eigenstates and form a basis that spans the space of left-handed quarks. However, this choice of basis is not unique. In particular, there are irreducible differences between the weak flavour eigenstates and the mass eigenstates, which form a second natural basis for describing the left-handed quarks. The convention normally used is that the up-type quarks are aligned in the two bases (without loss of generality) but the down-type quarks differ. The relation between the two bases is expressed as:

$$\begin{pmatrix} d' \\ s' \\ b' \end{pmatrix} = V_{\text{CKM}} \begin{pmatrix} d \\ s \\ b \end{pmatrix} \tag{2.1}$$

where (d, s, b) are the mass eigenstates, (d', s', b') are the flavour eigenstates, and V_{CKM} is a 3×3 complex matrix referred to as the Cabibbo-Kobayashi-Maskawa matrix[1]. It is written in the following form:

$$V_{\text{CKM}} = \begin{pmatrix} V_{ud} & V_{us} & V_{ub} \\ V_{cd} & V_{cs} & V_{cb} \\ V_{td} & V_{ts} & V_{tb} \end{pmatrix} \tag{2.2}$$

The elements of this matrix are free parameters in the SM, subject to condition of unitarity (i.e. that the net quark content of a system be the same irrespective of the basis in which it is expressed). The

[1] V_{CKM} is ultimately determined by the Yukawa couplings between the quarks and the Higgs field. See, *e.g.*, review 12 of Ref. [14].

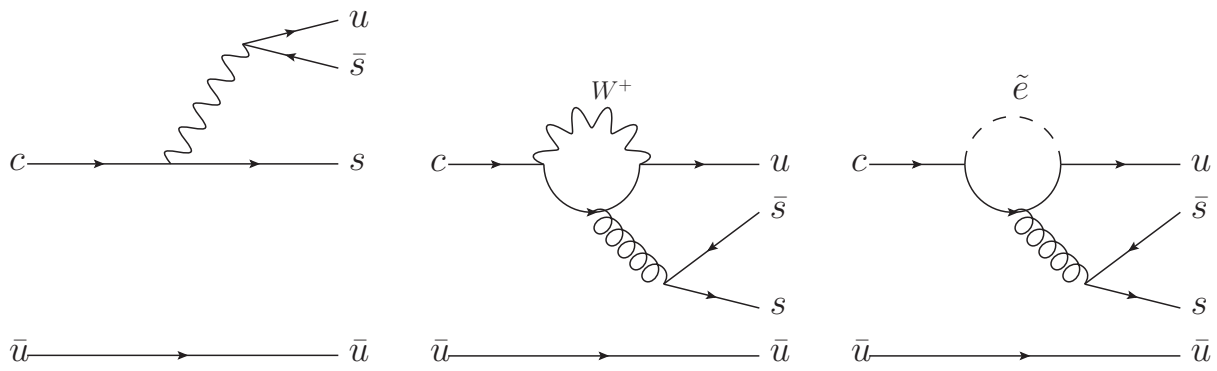

Figure 2.1: Diagrams that could contribute to $D^0 \to K^-K^+$. The first two diagrams are the SM tree (left) and penguin (centre) contributions. The third diagram is one possible NP contribution (in this case, another penguin diagram from R-parity-violating supersymmetry [15]).

unitarity condition is expressed as:

$$V_{CKM}V_{CKM}^{+} = I \tag{2.3}$$

and corresponds to nine separate constraints of the form

$$V_{ik}V_{jk}^{*} = \delta_{ij}. \tag{2.4}$$

Six of these relations are sums to zero, which can be expressed graphically as triangles in the complex plane; the unitarity condition is then equivalent to the requirement that the triangle close. After taking into account these nine constraints, there remain nine free parameters in V_{CKM}. Five of these are relative phases between quarks which have no physical significance, leaving four free, physically meaningful parameters. These can be expressed as three angles that mix between generations and one complex phase δ, which must take a non-zero value for CPV to occur.

Experimentally, we find that V_{CKM} is almost but not quite diagonal, and that the irreducible imaginary part is small but not quite zero. In particular, the far off-diagonal terms V_{ub} and V_{td} are both the smallest (being approximately 4×10^{-3} and 9×10^{-3}, respectively) and also the elements with the largest complex phases[2] (when working in the standard phase convention). Consequently, amplitudes involving ub and td couplings can contribute to *CP* violation—but are also strongly suppressed. Amplitudes involving off-diagonal terms are referred to as Cabibbo-suppressed (CS), as compared to Cabibbo-favoured (CF) amplitudes with on-diagonal terms. The degree of suppression in terms of powers of λ may also be given: singly CS for $\mathcal{O}(\lambda)$, doubly CS for $\mathcal{O}(\lambda^2)$.

There are a number of mechanisms by which *CP* violation can occur in hadrons, all of which are fundamentally due to interference between amplitudes with different contributing CKM elements. Despite this common origin, the mechanisms and their phenomenology differ greatly. We will discuss them in the following sections.

2.2 Direct *CP* violation

Direct *CP* violation occurs when[3]

$$\Gamma(D \to f) \neq \Gamma(\overline{D} \to \bar{f}) \tag{2.5}$$

[2] It should be emphasised that V_{ub} and V_{td} are not the only elements with non-zero complex phases in the CKM matrix. For example, the element V_{cs} has an imaginary component at order λ^4, where $\lambda = \sin\theta_C \approx 0.23$ and θ_C is the Cabibbo angle.

[3] As pointed out by Prof. Nir, the definition of direct CPV as used by the PDG is broader than this, and includes the case of time-dependent CPV that is not universal between different final states.

where D is a weakly decaying hadron[4] with CP conjugate $\overline{D}$, and f is a final state with CP conjugate $\bar{f}$. To produce direct CPV we need two or more amplitudes with different strong and weak phases that interfere, as we will show below. For example, in the SM the decay $D^0 \to K^-K^+$ can proceed via a tree or a penguin decay[5], as illustrated in Fig. 2.1. We can express these SM amplitudes as:

$$a(D^0 \to K^-K^+) = T + P \tag{2.6}$$
$$a(\overline{D}^0 \to K^+K^-) = \overline{T} + \overline{P}. \tag{2.7}$$

The tree (T) and penguin (P) components can be expressed as:

$$T = |T|\, e^{i\theta_t}\, e^{i\phi_t} \tag{2.8}$$
$$P = |P|\, e^{i\theta_p}\, e^{i\phi_p} \equiv r\,|T|\, e^{i(\theta_t+\Delta\theta)}\, e^{i(\phi_t+\Delta\phi)} \tag{2.9}$$

where θ_t and θ_p are the strong phases for the tree and penguin diagrams and $\Delta\theta$ is the difference between them, ϕ_t and ϕ_p are likewise the weak phases and $\Delta\phi$ their difference, and $r = |P/T|$ is the ratio of magnitudes[6]. The key distinction between the strong and weak phases is in how they transform under CP:

$$\overline{T} = |T|\, e^{i\theta_t}\, e^{-i\phi_t} \tag{2.10}$$
$$\overline{P} = |P|\, e^{i\theta_p}\, e^{-i\phi_p} = r\,|T|\, e^{i(\theta_t+\Delta\theta)}\, e^{-i(\phi_t+\Delta\phi)}. \tag{2.11}$$

Using this notation, we can write the combined amplitudes of eq. 2.6–2.7 as

$$a(D^0 \to K^-K^+) = |T|\, e^{i(\theta_t+\phi_t)}\,(1 + r\, e^{i(\Delta\theta+\Delta\phi)}) \tag{2.12}$$
$$a(\overline{D}^0 \to K^+K^-) = |T|\, e^{i(\theta_t-\phi_t)}\,(1 + r\, e^{i(\Delta\theta-\Delta\phi)}). \tag{2.13}$$

It follows that the difference in the mod-amplitudes-squared (to which the difference in decay rates is proportional[7]) is:

$$|a(D^0 \to K^-K^+)|^2 - |a(\overline{D}^0 \to K^+K^-)|^2 = -4\, r\,|T|^2 \sin\Delta\theta\, \sin\Delta\phi \tag{2.14}$$

Note that this is not time-dependent. The difference is more conveniently expressed as an asymmetry[8]:

$$A \equiv \frac{|a(D^0 \to K^-K^+)|^2 - |a(\overline{D}^0 \to K^+K^-)|^2}{|a(D^0 \to K^-K^+)|^2 + |a(\overline{D}^0 \to K^+K^-)|^2} \tag{2.15}$$
$$= \frac{-4\, r \sin\Delta\theta\, \sin\Delta\phi}{2 + \mathcal{O}(r)} \tag{2.16}$$
$$\simeq -2\, r \sin\Delta\theta\, \sin\Delta\phi \quad \text{if } r \ll 1. \tag{2.17}$$

From this it is immediately clear that the asymmetry vanishes if there is only one contributing amplitude ($r = 0$), or if the strong phases of the two amplitudes are equal[9] ($\Delta\theta = 0$), or if the weak phases are equal ($\Delta\phi = 0$). Conversely, for cases where there are non-trivial phase differences, the asymmetry is largest when the two contributions are of comparable size. This is one reason why suppressed modes

[4] The notation is chosen to suggest charm, but the same apples to hadrons with strangeness or beauty.

[5] The topologies are illustrated in Fig. 2.1: tree diagrams have no loops and exactly one interaction of an initial state quark, and penguin diagrams contain a loop from which a boson is emitted. In the gritty reality of QCD there is never just one diagram, of course, so when we say "tree" and "penguin" what we mean in practice is a set of amplitudes with a common CKM phase.

[6] We usually consider the case $r \ll 1$, i.e. that the tree diagram dominates, but the same conclusions hold if $r \gg 1$: one simply swaps P and T.

[7] We ignore for the moment the possible complication of indirect CPV in D^0 decays.

[8] Here we quote an asymmetry with $(D^0 - \overline{D}^0)$ in the numerator, but it is also legitimate to define asymmetries as $(\overline{D}^0 - D^0)$, *i.e.* with the opposite sign; this is quite often done in the B sector. In short, pay close attention to sign conventions when comparing asymmetries.

[9] Strictly, the condition is that the phase difference is zero modulo π.

can be more sensitive to direct *CP* asymmetries: in favoured modes the tree diagram dominates all other contributions.

Experimentally, the asymmetry of eq. 2.15 is usually measured as

$$A = \frac{\mathcal{B}(D^0 \to K^-K^+) - \mathcal{B}(\overline{D}^0 \to K^+K^-)}{\mathcal{B}(D^0 \to K^-K^+) + \mathcal{B}(\overline{D}^0 \to K^+K^-)} \tag{2.18}$$

where $\mathcal{B}$ represents a branching fraction. The same formalism applies for measurements of direct CPV in other decay modes[10].

We have now introduced the mechanism by which direct CPV occurs. We will move on to cover mixing and indirect CPV in Sec. 2.3, then return to direct CPV in charm for a more phenomenological discussion in Sec. 2.4.

2.3 Mixing and indirect *CP* violation in charm

In the preceeding section, we discussed direct CPV. We now consider the other class of CPV, indirect, which is induced by D^0-$\overline{D}^0$ mixing and is characterised by a time-dependent asymmetry. We begin by introducing mixing.

2.3.1 Mixing

Mixing occurs in weakly-decaying neutral mesons for which the flavour eigenstates (*e.g.* D^0 and $\overline{D}^0$) are distinct but are not distinguished by any conserved quantum number. Since the flavour eigenstates are not (in general) eigenstates of the Hamiltonian, and since there exist Feynman diagrams allowing D^0 to be transformed into $\overline{D}^0$, mixing must occur[11]. For example, if a state is initially pure D^0 (*e.g.* produced in the strong decay $D^{*+} \to D^0\pi^+$) its wavefunction at some later time will have a component of $\overline{D}^0$.

We quantify mixing with the normalised parameters x and y (Table 2.1), defined as[12]

$$\Gamma = \frac{\Gamma_2 + \Gamma_1}{2} \tag{2.19}$$

$$x = \frac{m_2 - m_1}{\Gamma} \tag{2.20}$$

$$y = \frac{\Gamma_2 - \Gamma_1}{2\Gamma} \tag{2.21}$$

where m_i and Γ_i are the masses and widths of the eigenstates of the Hamiltonian. These mass eigenstates are related to flavour eigenstates $|D^0\rangle$ and $|\overline{D}^0\rangle$ by:

$$|D_1\rangle = p|D^0\rangle - q|\overline{D}^0\rangle, \tag{2.22}$$

$$|D_2\rangle = p|D^0\rangle + q|\overline{D}^0\rangle, \tag{2.23}$$

where $|p|^2 + |q|^2 = 1$. The mixing rate[13] R_M is given by $R_M = (x^2 + y^2)/2$. For each of the mesons able to mix, this rate is of order 1 or more—except for charm, where it is approximately 3×10^{-5}.

[10] The example given here, K^+K^-, happens to be a self-conjugate, *CP*-even final state, but the same formalism applies in general. For a final state f, the asymmetry would be $A = \left[\mathcal{B}(D \to f) - \mathcal{B}(\overline{D} \to \bar{f})\right] / \left[\mathcal{B}(D \to f) + \mathcal{B}(\overline{D} \to \bar{f})\right]$.

[11] As ever: "Anything which is not forbidden is mandatory."

[12] The equations given are not quite enough to uniquely define the mixing parameters: there is one free phase as well. Here we are using the HFAG convention in which, in the limit of no indirect *CP* violation, $q/p = +1$ and $|D_1\rangle$ is the *CP*-odd eigenstate. But this is a detail which is only relevant to those making or combining mixing measurements.

[13] In concrete terms, this comes into play in meson oscillations with decays to semileptonic or to flavour-specific hadronic final states (*e.g.* $D^0 \to K^+\mu^-\overline{\nu}_\mu$ or $D^0 \to K^+\pi^-$). For small mixing and CPV, the lowest-order term in the time-dependent rate for semileptonic final states has a quadratic-times-exponential time dependence ($t^2\, e^{-\Gamma t}$) and a coefficient proportional to R_M. For hadronic final states the time distribution is more complicated due to interference with doubly CS decays, but the quadratic-times-exponential term is again proportional to R_M. Here, though, we use it more as a shorthand for the overall mixing scale.

Table 2.1: Mixing parameters x and y for neutral mesons. Data from HFAG [24] and the PDG [14]. (Parabolic errors given for D^0.)

Meson	x	y
K^0	0.95	almost 1
D^0	0.0037 ± 0.0016	0.0066 ± 0.0008
B^0	0.774 ± 0.006	0.0005 ± 0.005
B_s^0	26.85 ± 0.13	0.069 ± 0.006

This small rate is why it took about three decades from the discovery of charm to the first evidence of mixing [16, 17].

Although the relative uncertainties on the charm mixing parameters are still fairly large, we are now in a regime where the experimental uncertainties are much smaller than the theory uncertainties. The charm mixing rate is notoriously difficult to calculate theoretically, because charm occupies an awkward intermediate place in the hierarchy of masses (see, *e.g.*, [18] for more discussion). Charm is not heavy compared to the QCD mass scale and so mixing effects cannot easily be calculated perturbatively within the heavy-quark approximation (unlike for the B^0 and B_s^0 [19]). But charm is not light either, so that an exclusive calculation summing over all possible final states would be an enormous undertaking (unlike for the K^0). Current theory estimates for the charm mixing parameters are at best good to the order-of-magnitude level, and find that within the SM values of x and y up to $\mathcal{O}(10^{-2})$ are plausible [20, 18]. Note that the experimental values are at the upper end of this range: they may be small in an absolute sense, but they are perhaps also surprisingly large. An interesting implication of the current order-of-magnitude theory uncertainties is that, for all we know, the mixing rates observed could actually be dominated by NP effects. Inverting the argument, the observed level of mixing in charm can be used to constrain models of NP by requiring that they at most saturate it[14] [21].

Within the SM, it is long-distance effects (rescattering processes such as $D^0 \to K^-K^+ \to \overline{D}^0$) that dominate. Short-distance effects (box diagrams of the type that dominate mixing in the B^0 system) would be much smaller, with a simple estimate indicating they should enter at the 10^{-5} level [22]; more sophisticated calculations give numbers that are larger but not dramatically so [23].

On the experimental side, there have been numerous measurements of charm mixing, most of which can be divided into four categories. Because of the smallness of x and y, and because of the complementarity of these different types of measurements, it was the case for several years that no individual result had a significance exceeding 5σ, but that the combination of these measurements (as calculated by HFAG) excluded the no-mixing hypothesis at a high level of significance[15]. The four main classes of analysis contributing to the mixing combination are:[16]:

- Measurements of the time dependence of the ratio of wrong-sign (WS) to right-sign (RS) hadronic decays for a particular final state. Here WS and RS refer to the charge configurations of the final state, *e.g.* $D^0 \to K^\pm\pi^\mp$. The RS decay, $D^0 \to K^-\pi^+$, proceeds through a simple, unsuppressed, Cabibbo-favoured tree diagram. To a good approximation, its decay rate follows an exponential time distribution, $e^{-\Gamma t}$. By contrast, its WS partner decay, $D^0 \to K^+\pi^-$, receives contributions from two suppressed processes: the doubly CS tree diagram ($D^0 \to K^+\pi^-$), and mixing followed by a CF decay ($D^0 \to \overline{D}^0 \to K^+\pi^-$); there is also an interference term, of course. In the absence

[14] In crude terms, suppose that we measure the mixing parameters, obtaining $x_{\rm meas}$. We know that the total mixing contains SM and NP contributions, $x = x_{\rm SM} + x_{\rm NP}$. If we knew the SM contribution well, we could subtract it off and say that whatever remains is the NP contribution. But because of the large SM uncertainty, we instead use the much weaker constraint that the NP contribution at most satures x and so $|x_{\rm NP}| \lesssim |x_{\rm meas}|$, thereby constraining the size of NP contributions. (Here I ignore a factor of up to 2 that could arise in pathological cases.)

[15] Three experiments have now published analyses that by themselves exceed 5σ [25, 26, 27, 28].

[16] This list is not exhaustive. For example, it omits time-integrated measurements of wrong-sign semileptonic decays.

of mixing, only the doubly CS term is present and produces a decay time distribution of the form $e^{-\Gamma t}$, so that the WS/RS ratio is constant. However, mixing changes the time distribution. In the limit of small mixing, the ratio of WS/RS decay rates acquires a quadratic time dependence of the form $[R_D + y'\Gamma t + (x'^2 + y'^2)\Gamma^2 t^2]$, where R_D quantifies the DCS contribution and where x' and y' are related to the mixing parameters x and y by rotation through the strong phase δ between the DCS and CF decays to that final state[17]. The reason for measuring the WS/RS ratio, rather than the WS time-dependence itself, is simply to cancel out experimental systematic effects such as the overall decay time scale.

- Measurements of the ratio of the mean lifetime seen in CP eigenstates (*e.g.* $D^0 \to K^-K^+, \pi^-\pi^+$) to that seen in CP-mixed states (*e.g.* $D^0 \to K^-\pi^+$). For small mixing, the decay time distribution of CF, *CP*-mixed states can be described to a good approximation as a single exponential of the form $e^{-\Gamma t}$, with $\tau = 1/\Gamma \simeq 410\,\text{fs}$ being the average D^0 lifetime. Similarly, *CP* eigenstates of eigenvalue ± 1 can be described by an exponential of the form $e^{-[\Gamma \mp \Delta\Gamma]t}$, where the lifetime difference $\Delta\Gamma$ is related to the mixing parameter y (eq. 2.21). The observable $y_{CP} = [\tau(K^-\pi^+)/\tau(K^-K^+)] - 1$ is equal to y to a good approximation in the limit of small CPV.

- Time-dependent amplitude analyses of Dalitz plots of self-conjugate final states, primarily $D^0 \to K^0_S\pi^+\pi^-$, which measure x and y. These have similarities to the above two methods, and in addition have the powerful feature that the strong phases between CF and DCS decays can be obtained from amplitude analysis of the Dalitz plot[18]. This means that the mixing parameters (x, y) may be extracted directly, as opposed to parameters (x', y') rotated through an *a priori* unknown phase δ.

- Measurements of relative strong phases δ between doubly Cabibbo-suppressed (DCS) and Cabibbo-favoured (CF) decays, carried out at charm-at-threshold experiments (CLEO-c, BESIII). While these are not directly sensitive to mixing, they add information to the HFAG combination.

Other than the time-dependent amplitude analyses, these do not grant direct access to (x, y) but rather combinations of physics parameters (x, y, relative strong phases, indirect CPV), such that the world-average is not dominated by any one type of measurement but rather by their combination.

The most recent world average results on x and y from HFAG are illustrated in Fig. 2.2(a). Allowing for CPV, the central values are:

$$\begin{aligned} x &= \left(0.37^{+0.16}_{-0.16}\right)\% \\ y &= \left(0.66^{+0.07}_{-0.10}\right)\% \end{aligned}$$

As discussed above, the size of mixing in charm is a powerful constraint on models of NP. However, because the theory uncertainties are so large, there is at present not much more to be learned on this front from experiment; improving the precision on the mixing parameters will not move the upper bounds on x and y significantly. Measuring them precisely is important for another reason, though: we need to know x and y in order to go from measurements of CPV observables, such as time-dependent CP asymmetries, to the underlying physics parameters. The precision on x and y thus affects how well we can measure or constrain those parameters.

2.3.2 Indirect CPV

Indirect CPV in charm may be characterised by the magnitude and phase of q/p, with deviation from $|q/p| = 1$ and $\phi \equiv \arg(q/p) = 0$ indicating CPV (see eq. 2.22–2.23). In the HFAG phase convention [24],

[17] $x' = x\cos\delta + y\sin\delta$; $y' = y\cos\delta - x\sin\delta$. Note that $x'^2 + y'^2 = x^2 + y^2$.
[18] Or from charm-at-threshold experiments in a model-independent way.

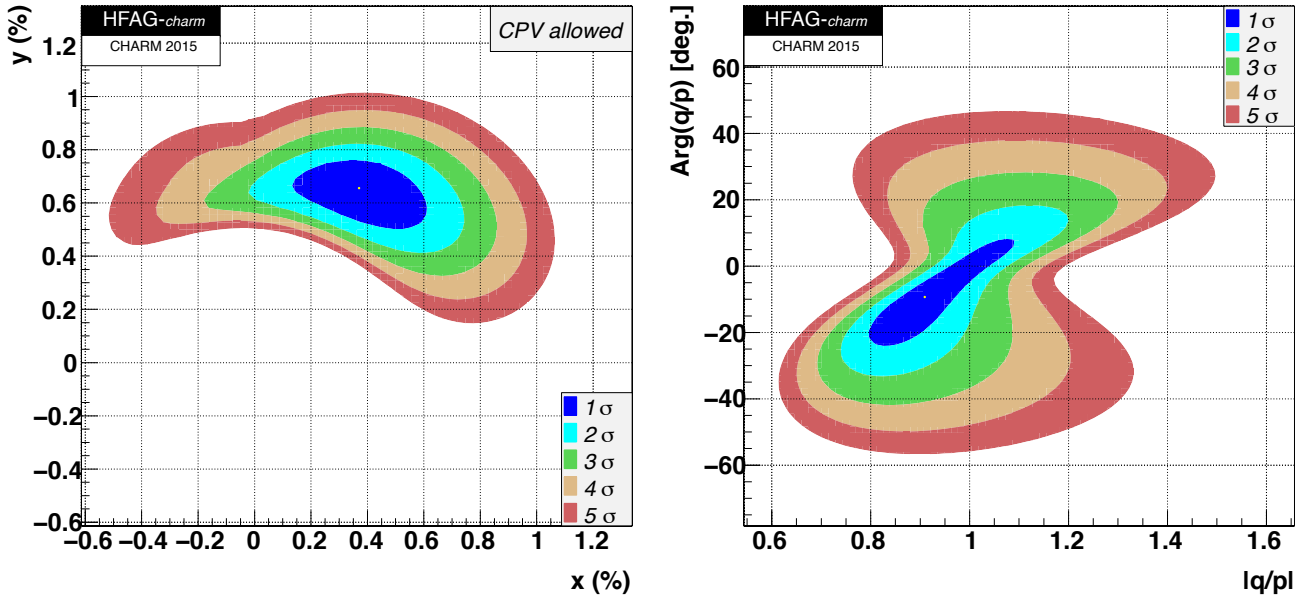

(a) (b)

Figure 2.2: World-average results from HFAG [24], as of 28 July 2015. In (a): the mixing parameters x and y, with the no-mixing point at $(0,0)$ now excluded with high significance. In (b): the indirect CPV parameters $\phi \equiv \arg(q/p)$ and $|q/p|$, with the no-CPV point at $(1,0)$ still allowed within the 1σ contour.

these are related to experimental observables as follows:[19]

$$
\begin{aligned}
2y_{CP} &= (|q/p| + |p/q|)\, y\cos\phi - (|q/p| - |p/q|)\, x\sin\phi \\
2A_\Gamma &= (|q/p| - |p/q|)\, y\cos\phi - (|q/p| + |p/q|)\, x\sin\phi \\
x'^{\pm} &= \left(\frac{1 \pm A_M}{1 \mp A_M}\right)^{1/4} \left(x'\cos\phi \pm y'\sin\phi\right) \\
y'^{\pm} &= \left(\frac{1 \pm A_M}{1 \mp A_M}\right)^{1/4} \left(y'\cos\phi \mp x'\sin\phi\right)
\end{aligned}
$$

where

$$
A_M = \frac{|q/p|^2 - |p/q|^2}{|q/p|^2 + |p/q|^2}.
$$

Here y_{CP} is the mixing parameter obtained from the ratio of CP-even[20] to CP-mixed lifetimes, discussed in the previous section. A_Γ is a related asymmetry:

$$
A_\Gamma = \frac{\tau(\overline{D}^0 \to f_{CP,+}) - \tau(D^0 \to f_{CP,+})}{\tau(\overline{D}^0 \to f_{CP,+}) + \tau(D^0 \to f_{CP,+})}, \tag{2.24}
$$

with the most precise results coming from $D^0 \to K^+K^-$ and $\pi^+\pi^-$. The observables $x'^{\pm}$ and $y'^{\pm}$ are simply the values of x' and y' measured with D^0 and $\overline{D}^0$ events, respectively; a difference between x'^{+} and x'^{-} or y'^{+} and y'^{-} would indicate CPV.

[19] Direct CPV is neglected in these expressions. This is a good approximation at present, but when the precision on A_Γ improves it may need to be taken into account [29].

[20] CP-odd final states can also be used, with suitable changes to the formulae.

Two key points follow directly from these expressions. First, the observable A_Γ is scaled down by a factor of x or y, such that even if indirect CPV is maximal A_Γ will be limited in magnitude to approximately x or y, i.e. $\mathcal{O}(\frac{1}{2}\%)$. We have only recently entered a regime where the uncertainty on A_Γ is smaller than this. Second, while a non-zero value of A_Γ would necessarily imply CPV, extracting values or limits on the physics parameters ϕ and $|q/p|$ would require x and y as inputs. Similar considerations apply to $x'^{\pm}$ and $y'^{\pm}$. The relative uncertainties on the mixing parameters are still substantial, although the situation is much better now than a few years ago. Thus, improving the precision with which x and y is known translates directly to improved constraints on the underlying CPV parameters.

Some of the recent mixing measurements noted in Section 2.3.1 included measurements of CP asymmetries [30, 26], and in addition LHCb has published a measurement of A_Γ with $1\,\text{fb}^{-1}$ of data [31]. Including these, the current world-average results with CPV fully allowed are shown in Fig. 2.2(b), and correspond to:

$$|q/p| = 0.91^{+0.12}_{-0.08} \tag{2.25}$$

$$\phi = \left(-9.4^{+11.9}_{-9.8}\right)^\circ . \tag{2.26}$$

Those values allow for the presence of direct CPV in suppressed decays. If it is assumed that there is no direct CPV in DCS decays[21] [32], these constraints are strengthened considerably:

$$|q/p| = 1.002 \pm 0.014 \tag{2.27}$$

$$\phi = (-0.07 \pm 0.6)^\circ. \tag{2.28}$$

The world-average values for $|q/p|$ and ϕ shown in eq. 2.25–2.26 indicate that CPV of more than 10–20% is excluded, so it is now clear that we do not have $\mathcal{O}(1)$ indirect CPV in charm. If direct CPV is negligible in DCS decays—and the excellent agreement with the null hypothesis of eq. 2.27–2.28 seems to back this up—then $\mathcal{O}(10^{-1})$ is also excluded and even $\mathcal{O}(10^{-2})$ is not far away. We have not yet reached the SM level, which is estimated to be $\mathcal{O}(10^{-4})$ to $\mathcal{O}(10^{-3})$ [33, 34, 35], but it looms ahead in the distance. On the plus side, the SM estimate of indirect CPV is dominated by short-distance physics so it is a reasonably tractable problem for theory, unlike direct CP violation.

2.4 Phenomenology of direct CPV in charm

Indirect CPV, discussed in Sec. 2.3.2, is described in the SM by a small number of parameters. It is not quite universal (since CPV in the interference between mixing and decay in general depends on the final state) but, as with mixing, measurements from different final states all help constrain the same underlying phenomenon. The story is very different for direct CPV, where the asymmetry can vary greatly from one decay mode to another.

Both within the SM and in general models of NP, the largest direct *CP* asymmetries are expected to be found in singly CS modes [36] where interference between penguin and tree diagrams can be substantial. Consequently, this is where most experimental and theoretical interest has been focused, and the analyses presented later in this chapter will search for CPV in singly CS decays. But it is not the only place where direct CPV could conceivably arise: direct CPV in doubly CS charm decays is negligible in the SM but possible in certain models of NP. Because double CS decays have branching fractions roughly a factor of $\sin^2\theta_C \sim 0.05$ smaller than comparable singly CS decays, the yields are necessarily poorer and so there are few experimental measurements of direct *CP* asymmetries in doubly CS decays with any useful precision at the moment. (CF modes have much higher BFs, of course, but there direct CPV would be negligible even in the presence of NP because the favoured tree diagram dominates—remember from eq. 2.17 that the asymmetry is proportional to r, the ratio of suppressed to dominant amplitudes.)

[21] This is certainly true for charm in the SM, and is also true in many but not all models of NP on the market. However, we should be a little cautious simply because there have been few experimental tests of this.

There has been a great deal of experimental progress in measurements of direct CPV in recent years, with multiple two-body decay modes reaching precisions on *CP*-violating asymmetries of well below 1% and closing in on 10^{-3}, and searches for CPV in the phase space of multi-body decays with signal yields in the millions. (Some of these searches will be discussed in detail later in this chapter.) The theoretical side, however, is murky: thanks to advances in the understanding of the SM gluonic penguin contributions (or, more precisely, to advances in the understanding of the theory uncertainties which turn out to be larger than naively expected) we now know that direct CP asymmetries can arise at the $\mathcal{O}(10^{-3})$ level in the SM, and as much as $\mathcal{O}(\text{few} \times 10^{-3})$ can be accommodated. We have already reached this level of precision experimentally, so in the absence of a major advance in theoretical engineering it seems like we would not be able to say whether some future observation of direct CPV in a generic singly CS mode at the 0.1%-level is SM physics or not. Therefore, we have no chance[22] of discovering NP with this kind of brute-force approach. But all is not lost: we can still test the SM by combining information from $SU(3)$-related final states, testing whether the overall pattern is consistent [37]. Another path forward is to focus effort on modes where the SM contribution to the asymmetry is suppressed (*e.g.* SCS modes with $\Delta I = 3/2$ [38]).

One last note: charmed baryons are also produced at significant rates at LHCb [39], and good-sized samples have been accumulated at the B-factories. Their decays are also sensitive to direct CPV, but measurements of this are sorely lacking.

2.5 Search for CPV in $D^+ \to K^-K^+\pi^+$

This section summarises the analysis published in [40]. This was the first LHCb result on CP violation.

2.5.1 Introduction

As discussed in Section 2.4, singly Cabibbo-suppressed decays such as $D^+ \to K^-K^+\pi^+$ are good candidates to search for *CP* violation, which may occur through SM processes (interference of the tree diagram with a gluonic penguin) and could be enhanced by NP. This particular channel has a three-body final state, which makes the analysis more complicated but in the end adds to the sensitivity.

The asymmetry observable in eq. 2.18 is expressed in terms of branching fractions. It's possible to make an equivalent measurement for a three-body decay, constructing an asymmetry from the branching fraction integrated across the phase space:

$$A = \frac{\mathcal{B}(D^+ \to K^-K^+\pi^+) - \mathcal{B}(D^- \to K^+K^-\pi^-)}{\mathcal{B}(D^+ \to K^-K^+\pi^+) + \mathcal{B}(D^- \to K^+K^-\pi^-)}. \tag{2.29}$$

Measurements of this overall asymmetry have been performed at CLEO-c [41] and BABAR [42] (and, with smaller statistics, at E791 and FOCUS), with no significant asymmetry found. However, this is only part of the story.

A multi-body hadronic decay amplitude is really the quantum mechanical sum of many interfering amplitudes—for example, $D^+ \to \phi(1020)\pi^+$, $D^+ \to K^*(892)^0K^+$, $D^+ \to a_0(1430)^0\pi^+$, *etc.*. In charm decays, where the available phase space is small (i.e. final-state particles and resonances are not that much lighter than the parent) and crowded, these resonances overlap and interfere a lot. The same arguments given previously about CPV arising from diagrams with different strong and weak phases (*e.g.* tree *vs.* penguin) apply, but now we have additional sources of phase variation: between resonances, and within each resonance.

To help us visualise this structure, the phase space of a decay of this type—a pseudoscalar into three pseudoscalars—can be represented as a two-dimensional distribution known as a Dalitz plot (DP). An example is shown[23] in Fig. 2.3. The axes of a DP are the squares of the invariant masses of two of

[22] Strictly speaking the door is not completely shut: we could observe direct CPV at some huge level like 10% in an obscure decay mode which has not yet been tested. But realistically, no.

[23] More details on the dataset and selection used for this plot will be given below.

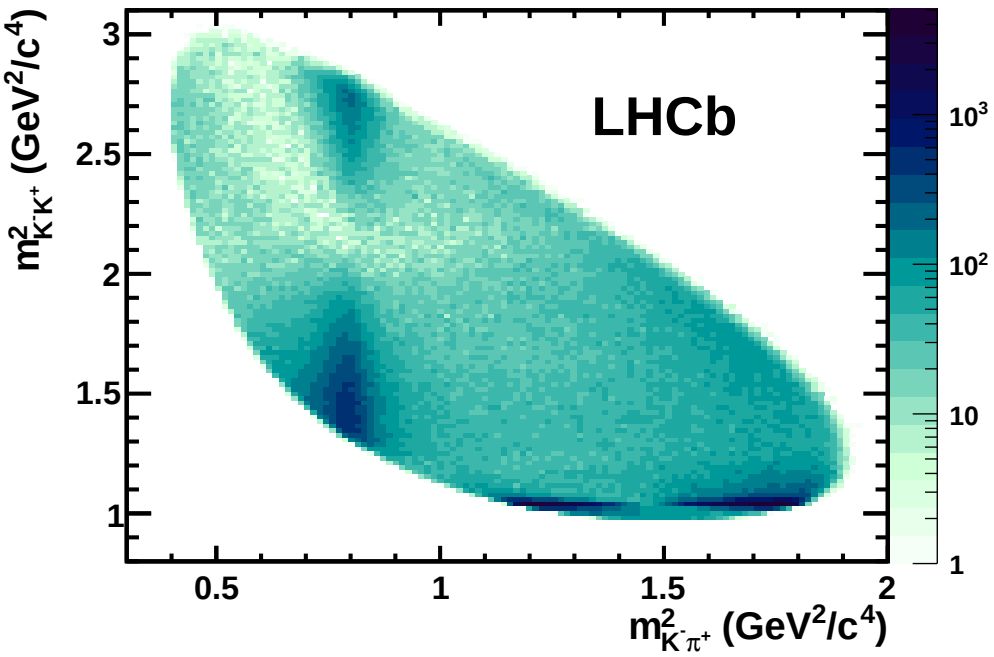

Figure 2.3: Dalitz plot of $D^+ \to K^-K^+\pi^+$ with $0.35\,\text{pb}^{-1}$ of LHCb data. The plot is not efficiency-corrected or background-subtracted.

the three daughters, *e.g.* $m^2(K^-\pi^+)$ and $m^2(K^-K^+)$. This choice is motivated by the decay rate for $D \to 123$ being[24]

$$\Gamma = \frac{1}{32\,(2\pi)^3\,s^{3/2}}\,|\mathcal{M}|^2\,\mathrm{d}m^2_{12}\,\mathrm{d}m^2_{13} \tag{2.30}$$

where $\mathcal{M}$ is the matrix element and $\sqrt{s}$ is the mass of the parent D. The phase space density is proportional to $(\mathrm{d}m^2_{12}\,\mathrm{d}m^2_{13})$ and is uniform within the physically allowed region of the Dalitz plot. As a result, all of the structure seen can be attributed solely to variation in $\mathcal{M}$ (i.e. our amplitude). In this representation, a narrow resonance will appear as a band that is horizontal (for K^-K^+ resonances in our example), vertical (for $K^-\pi^+$), or diagonal (for a hypothetical $K^+\pi^+$ resonance). Such a band will have internal structure, notably variation in intensity along the band that is associated with the helicity angle and has J minima for a spin-J resonance. This can be seen clearly in Fig. 2.3 for the dominant horizontal $\phi(1020)$ and vertical $K^*(892)^0$ bands, both of which are spin 1 and so have two lobes with a single node in between. Since all structure is due to variation in $\mathcal{M}$, and direct *CP* violation is a non-trivial difference between $\mathcal{M}$ for D^+ and for D^-, *CP* violation will show up as a difference between the distributions in the D^+ and D^- Dalitz plots and/or as a difference in their overall rates.

We now have a tool to visualise variation across the phase space of the decay, and can to a degree associate regions of the DP with contributing resonances[25]. There is a good deal of interesting physics in understanding and modelling this structure [44, 42] but that is not our main focus here: we want to search for CPV. However, the resonant structure does affect how CPV might manifest itself and therefore what strategy we should use to look for it. To investigate this, we will take a model of the DP published by CLEO-c (fit B of [44]). They use what is known as the Isobar approach in which the amplitude is expressed as a sum of interfering resonances each of which has a clear physical origin and

[24] See [14], and in particluar the Dalitz Plot Analyais Formalism review.

[25] This is obviously imperfect, since the resonances overlap and can have long tails, but nonetheless observing CPV in one region of the DP would give us clues about the mechanism [43].

varies in a predictable way across the Dalitz plot:

$$a(m^2_{12}, m^2_{13}) = \sum_k c_k \, F_k(m^2_{12}, m^2_{13}), \tag{2.31}$$

where $a(m^2_{12}, m^2_{13})$ is the total amplitude at a point in the DP, k is an index that runs over the different resonant components, c_k is a complex coefficient giving the relative magnitude and phase of a component, and $F_k(m^2_{12}, m^2_{13})$ is a form factor describing the variation of a component across the DP. We simplify the model by eliminating resonant contributions whose fit fraction[26] is less than 2%. We then generate toy events based on this model (with no inherent CPV), and variants of it with CPV introduced. The asymmetry patterns in the DP are illustrated in Fig. 2.4 and summarised below.

When a *CP* asymmetry in the *magnitude* ($|c_k|$) of a resonance is introduced[27], we see an asymmetry within the band of that resonance and, to a lesser degree, in the immediately adjacent tail/interference regions, with the observed asymmetry having the same sign throughout.

When an asymmetry in the *phase* ($\arg c_k$) of a resonance is introduced, we see comparatively small effects in the resonance band itself but much larger asymmetries in the nearby tail/interference regions (with some effects still being visible quite far away even for a narrow resonance like the $\phi(1020)$). These effects are driven by the rapid variation in strong phase of the form factor of the resonance in question (*vs.* via interference with other components whose phases are varying much more slowly). This variation is illustrated in Fig. 2.5, showing the phase of the total amplitude in the $\phi(1020)$ region. The combination of an asymmetry in the weak phase ($\arg c_k$) and the variation of the strong phase drives the pattern of local rate asymmetries seen in Fig. 2.4. In particular, we see that the rate asymmetries change sign from one side of the resonance to the other[28]. We will discuss the implications for the analysis strategy in the following section.

2.5.2 Analysis strategy

We now start to have some idea of how *CP* asymmetries might manifest themselves[29]. In particular, we see the importance of searching for local asymmetries. In the examples discussed above—a change in the magnitude or phase of c_k for a single resonance between D^+ and D^-—the asymmetries were localised in particular regions of the DP, so that a measurement of the asymmetry integrated across the whole DP would at best have diluted the asymmetry with a lot of zero-asymmetry events, and at worst would have combined regions whose asymmetries have different signs and thereby cancelled them out. This suggests a strategy of looking for local asymmetries across the DP. There are a number of methods that could be used for this, including unbinned techniques [46]. We use instead a straightforward binned approach in which we divide the DP into a number of bins which do not overlap and which between them cover the entire DP. For each bin i we measure the yield of D^+ events n_{i+} and of D^- events n_{i-} in that bin. We also measure the total yields summed across all bins, $N_+ = \sum_i n_{i+}$ and $N_- = \sum_i n_{i-}$.

We can then obtain the difference Δ_i in normalised yields and the significance S^i_{CP} of that difference:

$$\Delta_i = \frac{n_{i+}}{N_+} - \frac{n_{i-}}{N_-} \tag{2.32}$$

$$S^i_{CP} = \frac{\Delta_i}{\sigma(\Delta_i)} \tag{2.33}$$

[26] Defined as: $FF_j \equiv \left[\int |c_j F_j(m^2_{12}, m^2_{13})|^2 \, \mathrm{d}m^2_{12} \, \mathrm{d}m^2_{13}\right] / \left[\int |\sum_k c_k F_k(m^2_{12}, m^2_{13})|^2 \, \mathrm{d}m^2_{12} \, \mathrm{d}m^2_{13}\right]$. In the limit of non-interfering resonances, this would be the yield fraction.

[27] That is, for some particular resonance k, $|c_k|$ for D^+ is different from $|c_k|$ for D^- (ignoring the pathological case of an overall normalisation change in which c_k for every resonance is scaled by a common factor).

[28] The type of resonance plays a role here: the $\phi(1020)$ is a vector, so the amplitude is P-wave implying a sign change along the resonance.

[29] The examples above are simplistic, of course: CPV is very unlikely to show up in the $\phi(1020)$ alone, and could appear associated with a broader S-wave component. But they illustrate the point.

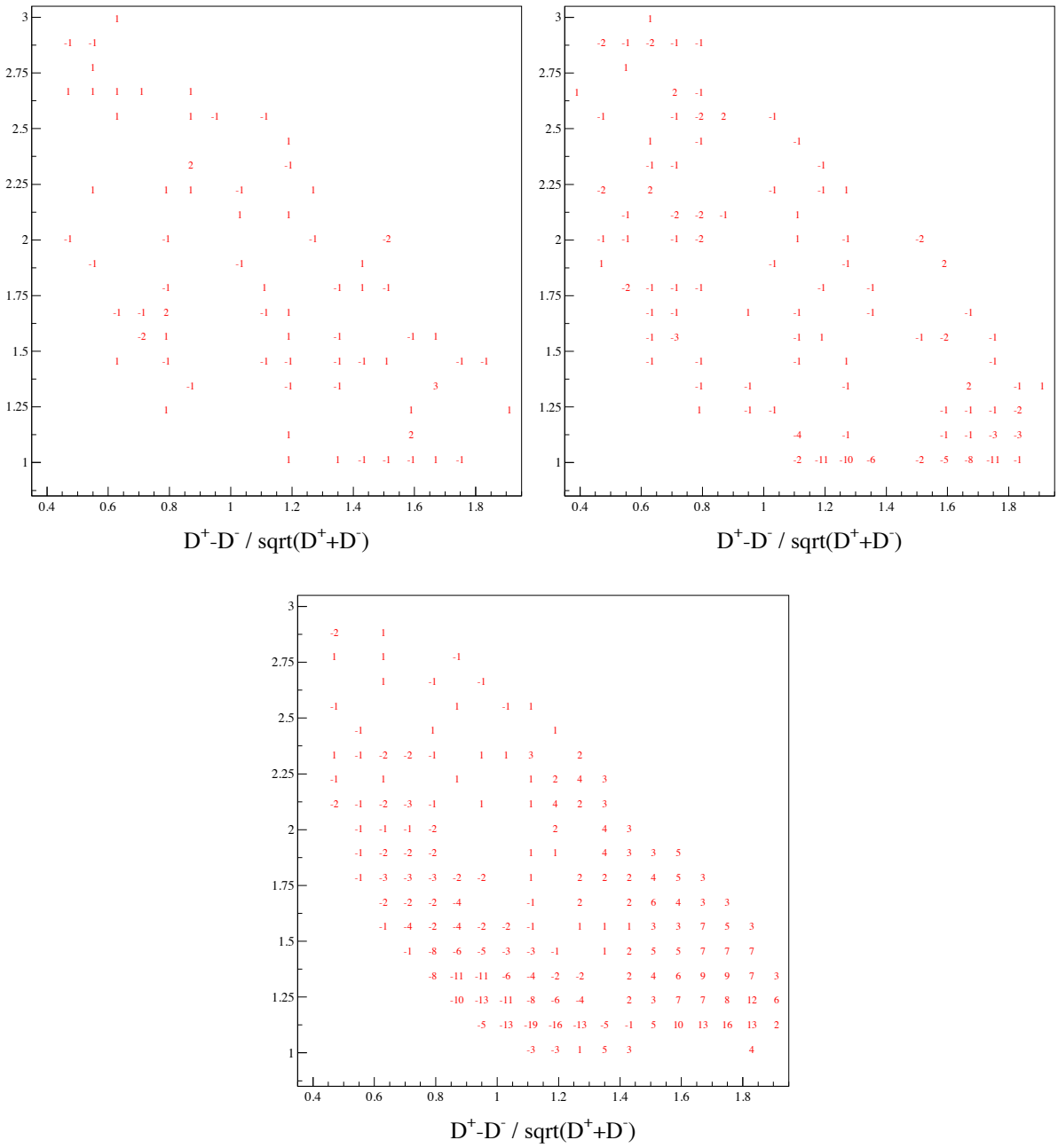

Figure 2.4: Local asymmetry significance for samples of toy events according to a model of the $D^+ \to K^-K^+\pi^+$ Dalitz plot based on a CLEO-c analysis, with $m^2_{K^-\pi^+}$ along the x-axis and $m^2_{K^-K^+}$ along the y-axis. The samples each contain 4M D^+ and 4M D^- events. Each DP is divided into bins and the asymmetry significance calculated in each bin (red numbers); where it is less than 1σ the bin is left blank. Upper left: no *CP* violation. Upper right: a 1% asymmetry in magnitude of the $D^+ \to \phi(1020)\pi^+$ component, generating large asymmetries along the narrow resonance band. Lower: a 10° asymmetry in the phase of the $D^+ \to \phi(1020)\pi^+$ component, generating asymmetries in the tails (interference regions) near the resonance band. **Acknowledgement:** This figure was the work of Alberto Reis from CPBF.

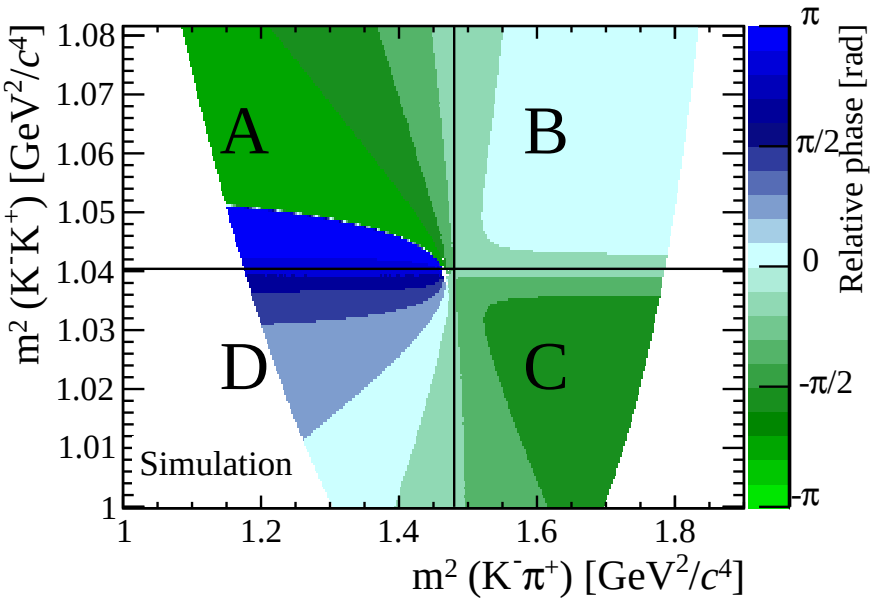

Figure 2.5: Phase of the decay amplitude according to a model of the $D^+ \to K^-K^+\pi^+$ Dalitz plot based on a CLEO-c analysis, with no *CP* violation. The $\phi(1020)$ region is shown. The phase is seen to change by approximately π along the resonance (A→B or D→C), and there are also large changes in phase across the resonance (A→D or B→C). **Acknowledgement:** This figure was the work of Hamish Gordon, from Oxford (later CERN), and was published in [45]

where $\sigma(\Delta_i)$ is the statistical uncertainty[30] on Δ_i. This gives us a signed asymmetry significance in each bin; if there is no *CP* asymmetry and sufficient statistics in each bin, it will form a Gaussian distribution with mean of zero and sigma of one. With numerous bins we expect some fraction of them to fluctuate away from zero even in the absence of CPV, so to assess whether we found genuine asymmetry we perform a χ^2 test, with

$$\chi^2 = \sum_i \left(S^i_{CP}\right)^2 \tag{2.34}$$

and the number of degrees of freedom equal to the number of bins minus one (for the normalisation N_+/N_-).

This brings us to a second, key point about the search strategy: having too many bins reduces our sensitivity. To illustrate this, consider a region of the DP with a constant asymmetry throughout the region such that the yields of D^+ and D^- are m_+ and m_-, with $m_- = r\,m_+$. Suppose that we divide the region into q bins of equal size. In each bin, the expected yield difference is

$$\frac{m_+}{q} - \frac{m_-}{q} = \frac{m_+(1-r)}{q}.$$

For simplicity, let's assume that $N_+ \simeq N_-$ (meaning that there is a balancing asymmetry of the opposite sign somewhere else in the DP, or that the region with the asymmetry represents a small fraction of the overall yield) so that we're not distracted by normalisation factors, and as usual we treat N_+ and N_- as fixed while calculating the χ^2. Then for each bin in our region of interest, the expected difference in normalised yields is

$$\bar{\Delta}_i = \frac{m_+(1-r)}{qN_+}, \tag{2.35}$$

[30] The per-bin statistical uncertainties on n_{i+} and n_{i-} enter this calculation but the totals N_+ and N_- are treated as constants. This is taken into account later in the count of the number of degrees of freedom (NDF).

and the expected uncertainty on this will be

$$\bar{\sigma}(\Delta_i) = \sqrt{\frac{m_+(1+r)}{q}}\,\frac{1}{N_+}. \tag{2.36}$$

Dividing eq. 2.35 by 2.36, we obtain an expected significance in each bin:

$$\bar{S}^i_{CP} = \sqrt{\frac{m_+}{q}}\,\frac{1-r}{\sqrt{1+r}} \tag{2.37}$$

and, roughly, the expected χ^2 sum for that region[31] is

$$\bar{\chi}^2 = \sum_i (\bar{S}^i_{CP})^2 = q(\bar{S}^i_{CP})^2 = m_+\,\frac{(1-r)^2}{1+r}. \tag{2.38}$$

The important thing here is that increasing q does not increase the expected total χ^2 for the region—but it *does* increase the number of degrees of freedom. What this means is that having too fine a binning actually hurts our sensitivity, because the extra bins don't bring any new information but they increase the number of times we could see a fluctuation under the null hypothesis. This runs counter to the normal intuition for a Dalitz plot amplitude analysis, where (if binning at all) one tries to use bins that are as fine as possible to resolve all of the substructure in the plot. Here we want just enough bins to separate regions of different asymmetry but no more.

Of course, the problem is that we don't know *a priori* how and where CPV might manifest itself. We will hedge our bets by using four different binning schemes: two with a uniform binning (with 199 and 530 bins) and two with an "adaptive" binning (with 25 and 106 bins). The adaptive binnings were chosen to reflect the structure of the DP and the insights about the structure of asymmetries discussed above[32]. The uniform binnings offer a more agnostic alternative, making no explicit assumption about the form taken by NP. If a CPV asymmetry is present but varies only slowly across the DP, a uniform scheme with few bins may offer a better chance of finding it. (But after discussion these various scenarios, it is worth emphasising that the method itself is model-independent: there will be no model systematic uncertainty. We will be more sensitive to some CPV scenarios than others—but this is true no matter what you do.)

2.5.3 Data, binning, and expected sensitivity

With a method in hand, we now turn to the data. The selection is described in [40] and requires that the $D^+ \to K^-K^+\pi^+$ candidate fire the software trigger and pass a variety of geometrical and kinematic selection cuts after being reconstructed offline. In particular, the D^+ decay vertex is required to be well-separated from the event primary vertex (or from all such vertices, if there is more than one), and the D^+ candidate is required to originate at a primary vertex (PV). Hadronic particle identification requirements based on RICH information are imposed to separate pions from kaons. The same selection is used to select candidates for two Cabibbo-favoured control modes: $D_s^+ \to K^-K^+\pi^+$ and $D^+ \to K^-\pi^+\pi^+$. The resulting mass spectra are shown in Fig. 2.6. The signal yields are approximately 370k for $D^+ \to K^-K^+\pi^+$, 515k for $D_s^+ \to K^-K^+\pi^+$, and 3760k for $D^+ \to K^-\pi^+\pi^+$, with purities of 91% for each of the $K^-K^+\pi^+$ modes and 98% for the $K^-\pi^+\pi^+$ mode.

Having fixed the binning and knowing the expected yield, we can use the DP model discussed above to estimate our sensitivity to various CPV scenarios (and to check that the analysis finds no

[31] This is an illustrative sketch rather than a proof—there are quite a few implicit assumptions here, such as m_+/q being large.

[32] In previous DP analyses, adaptive binning algorithms were used to produce bins of approximately uniform population. While this algorithm does aim to do that, it is also constrained to follow certain physical features of the DP. Without going into fine detail, it will cut the dominant $\phi(1020)$ and $K^*(892)^0$ bands in half transversely and is likely to split their lobes in half longitudinally. It also compartmentalises a region in the upper-right of the plot, away from these dominant bands, where broad/non-resonant contributions are more important.

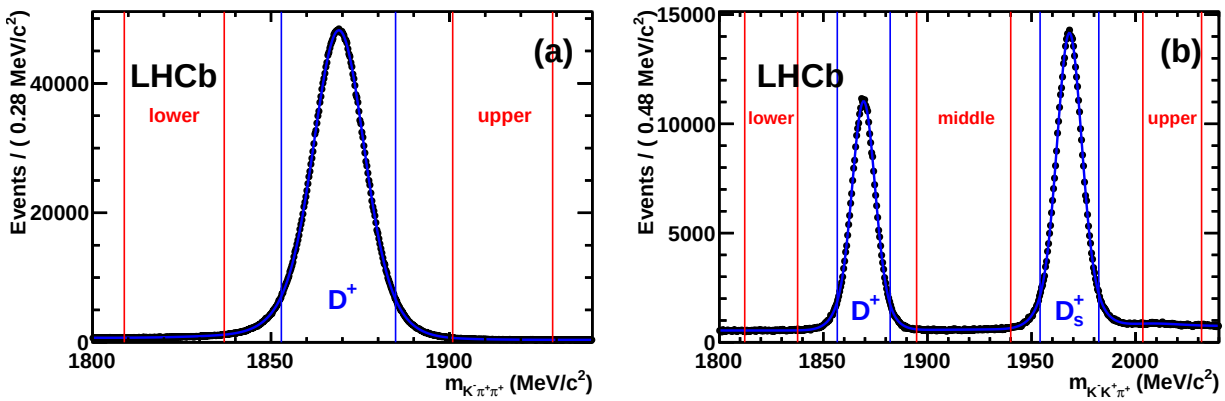

Figure 2.6: Mass spectra from most of the 35/pb data set. The plots show (a) $K^-\pi^+\pi^+$, with the D^+ peak visible; (b) $K^-K^+\pi^+$, with the D^+ and D_s^+ peaks visible. For technical reasons related to the trigger mass windows, about 17% of the data are not included in these plots but are used for the CPV searches.

CPV when none is present). The decay kinematics are simulated in two steps: the D^+ momentum p and transverse momentum $p_{\rm T}$ in the lab frame are sampled randomly from the 2D distribution found in data, and the daughter momenta in the D^+ rest frame are generated according to the DP model. As before, we use a toy MC that does not simulate the detector response in detail (whereas the full MC does, using GEANT4). Instead, we use a parameterised model of the detector efficiency as a function of position in the DP. We also include a momentum-dependent efficiency asymmetry between K^- and K^+ which arises because the interaction cross-sections in matter differ between the two[33]. The momentum dependence of the latter is key: the mode $D^+ \to K^-K^+\pi^+$ and its conjugate $D^- \to K^+K^-\pi^-$ have the same numbers of K^+ and of K^- in the final state, but their momentum distributions can differ. Table 2.2 summarises the sensitivity of the two adaptive binnings used under various CPV hypotheses, evaluated by running sets of 100 toy experiments. For each toy experiment, the χ^2 and NDF for the whole DP are obtained and converted into a p-value[34] and hence an unsigned significance measured in σ. For each set of 100 toys, we quote two figures of merit: the fraction of toy experiments for which the overall significance was at least 3σ, denoted $p(3\sigma)$; and the mean significance, denoted $\langle S \rangle$. The behaviour when generating events without CPV was as expected: a mean significance of approximately 1σ and a small fraction of toys with a 3σ signal consistent with the expected rate of 0.3%. (Additional toy studies of $D^+ \to K^-K^+\pi^+$ with no CPV showed no significant excess, and neither did a study of $D^+ \to K^-\pi^+\pi^+$ with a total of 10^9 toy events.) When inserting a real CP asymmetry into the model used to generate the toy experiments, these numbers increase. As expected, the sensitivity depends on the size of the asymmetry: we see this clearly when varying the phase asymmetry of the $\phi(1020)$ from 2° to 6°. We also see that which binning is more sensitive depends on the CPV hypothesis: between the two adaptive binnings, the first is the more sensitive for the $\phi(1020)$ phase asymmetry but the second binning does better for a $\kappa(800)$ magnitude asymmetry.

We have checked the sensitivity of the method under a few hypotheses and verified that it doesn't produce false positivies with toy MC that includes parameterisations of the detector efficiency and kaon detection asymmetry. However, there could be some other effect that produces fake local[35] asymmetries in real data. We will now use control samples of data to establish that there is no such effect at the level of our sensitivity.

[33] This effect has since been studied extensively at LHCb with control samples of data, but at the time we had only information from GEANT simulation studies.

[34] A measure of how frequently a result of this size or larger would be expected under the null hypothesis.

[35] Remember, effects which produce a D^+/D^- asymmetry that's constant across the DP will drop out in our normalisation and don't bother us.

Table 2.2: Results from sets of 100 toy experiments with sample size corresponding to the $D^+ \to K^-K^+\pi^+$ signal yield for different *CP* asymmetries, analysed with the Adaptive I and II binnings. $p(3\sigma)$ is the fraction of toys with a 3σ or larger CPV significance. $\langle S \rangle$ is the mean significance with which CPV is seen.

CPV	Adaptive I		Adaptive II	
	$p(3\sigma)$	$\langle S \rangle$	$p(3\sigma)$	$\langle S \rangle$
no CPV	0%	0.84σ	1%	0.84σ
2° in $\phi(1020)$ phase	5%	1.6σ	2%	1.2σ
3° in $\phi(1020)$ phase	38%	2.8σ	12%	1.9σ
4° in $\phi(1020)$ phase	76%	3.8σ	41%	2.7σ
5° in $\phi(1020)$ phase	97%	5.5σ	79%	3.8σ
6° in $\phi(1020)$ phase	99%	7.0σ	98%	5.2σ
6.3% in $\kappa(800)$ magnitude	16%	1.9σ	24%	2.2σ
11% in $\kappa(800)$ magnitude	83%	4.2σ	95%	5.6σ

One potentially dangerous source of such asymmetries consists of left-right differences in the detector itself. These are relevant because, as they pass through LHCb's dipole magnet, tracks of one charge are pushed towards the left and tracks of the other charge towards the right. There is overlap in the parts of the detector seen by the two charges, but for final states with a net charge such as ours there will necessarily be some difference in the subdetector elements used for D^+ and D^-. Of course, the detector is designed to be as left-right symmetric as possible, but nonetheless we can imagine small differences in material, misalignments, inefficiencies at the level of individual channels, *etc.*. To reduce the potential effect of such differences, the polarity of LHCb's magnet was changed several times during the data-taking period, with roughly equal amounts of integrated luminosity for each of the two polarities. This is important because such effects would flip around when the magnet polarity is changed (i.e. the fake asymmetries they generate would change sign). We therefore treat the magnet polarity up (MagUp) and down (MagDown) samples separately, so that for each Dalitz plot bin we have a measured asymmetry for each. We then take the average of the two asymmetries for that bin, cancelling out effects which change sign. As we will show with control samples below, this suppresses left-right effects below the level of our sensitivity.

2.5.4 Results in control samples

As explained in Sec. 2.4, we expect that CPV should be much too small to observe in Cabibbo-favoured charm decays even in the presence of NP. We can therefore use CF decay modes as a check: we should see no significant *CP* asymmetry when we apply our method to them. The two modes of interest are shown in Fig. 2.6 along with the signal. The first is $D_s^+ \to K^-K^+\pi^+$, which has the same final state as our signal mode and a larger yield (515k vs 370k), allowing us to make tests under conditions which closely mimic the final measurement. The second is $D^+ \to K^-\pi^+\pi^+$, which is much more sensitive to fake asymmetries than our signal for two reasons: first, its yield is an order of magnitude larger (3760k); second, its final state contains only one kaon. As discussed earlier, we know that there is a momentum-dependent charge asymmetry in kaon efficiency that arises from the different material interaction cross-sections; we would expect at least partial cancellation between the K^+K^- pair in our signal mode but there is no equivalent cancellation in $D^+ \to K^-\pi^+\pi^+$. This makes for a powerful control: if we obtain a null result in $D^+ \to K^-\pi^+\pi^+$, that will imply that many potentially nasty effects are negligible in $D^+ \to K^-K^+\pi^+$. The main exception will be effects that are specific to the final state, such as from backgrounds. We will use $D_s^+ \to K^-K^+\pi^+$, and the mass sidebands to account for those.

For each of the control modes, we try a range of binnings using both the uniform and adaptive

Table 2.3: Results of consistency tests for the $D^+ \to K^-\pi^+\pi^+$ control mode for a variety of binning schemes. The table shows the p-values obtained for the individual magnet polarities (MagUp, MagDown) and for the bin-wise average of the two (MagAvg). The numbers for individual magnet polarities with 25 uniform bins are not available.

Binning scheme	MagUp	MagDown	MagAvg
25 adaptive	49%	0.1%	12%
100 adaptive	57%	7.9%	30%
400 adaptive	93%	58%	66%
900 adaptive	75%	35%	57%
1300 adaptive	70%	61%	82%
25 uniform			1.7%
100 uniform	96%	4.4%	55%
400 uniform	63%	38%	73%
900 uniform	46%	2.5%	18%
1300 uniform	53%	44%	74%

binning schemes. The results for $D^+ \to K^-\pi^+\pi^+$ are shown in Table 2.3. We see that the average of the magnet polarities is more robust than each individually; this is expected since the polarity flip leads to the cancellation of systematic effects associated with left-right asymmetries as discussed earlier. The p-values for the averaged data are generally consistent with a null result. The most significant of these, 1.7% seen for 25 uniform bins, is small but not dangerously small, considering that (a) the yield for this mode is an order of magnitude larger than for the signal, (b) this mode is less robust than the signal against systematic effects related to kaon asymmetries, and (c) we have made ten different statistical tests[36].

The results for $D_s^+ \to K^-K^+\pi^-$ are shown in Table 2.4. Adaptive binnings with 25 and 129 bins are tested. Because the structure of the DP is highly non-uniform, the uniform binnings are tested within sub-regions of the DP, referred to as the ϕ region with $m^2(K^-K^+) < 1.1\,\mathrm{GeV}^2/c^4$, the $\overline{K}^{*0}$ region with $0.7 < m^2(K^-\pi^+) < 0.95\,\mathrm{GeV}^2/c^4$, and the middle region with $m^2(K^-K^+) > 1.1\,\mathrm{GeV}^2/c^4$ and $m^2(K^-\pi^+) > 0.95\,\mathrm{GeV}^2/c^4$. All of the values are fully compatible with the null hypothesis.

The sideband data are also analysed to search for asymmetries in the backgrounds that might affect the signal regions[37]. Five subsamples are used, as illustrated in Fig. 2.6: the lower and upper $K^-\pi^+\pi^+$ sidebands, and the lower, middle, and upper $K^-K^+\pi^+$ sidebands. Localised backgrounds from D^{*+} decays are removed: fully reconstructed $D^{*+} \to D^0(K^-K^+)\pi^+$ decays in the upper $K^-K^+\pi^+$ sideband, and partially reconstructed or misidentified $D^{*+} \to D^0\pi^+$ decays in the lower $m(K^-\pi^+\pi^+)$ sideband. No significant asymmetries are seen in the magnet-averaged data, with the lowest p-value being 9%. Other cross-checks are also carried out, notably: tightening kaon PID cuts (to check for misidentified charm backgrounds), imposing a cut requiring the D^+ to point to the PV (to check the effect of secondary charm), carrying out the analysis on simulated data, and investigating the effect of different trigger requirements. No false positives are seen.

2.5.5 Results

The results of the analysis are shown in Table 2.5 and Fig. 2.7 with four binning schemes, two adaptive and two uniform. No statistically significant asymmetry is seen. As a further check, the analysis is repeated with a range of other binning schemes; in all cases the data are consistent with no CPV.

[36] They are not statistically independent, of course—but the binnings are substantially different and will tend to pick up different fluctuations.

[37] A separate procedure was also defined to check for second-order effects from interactions between a global background asymmetry and different global signal asymmetry in the event of a significant signal, but was not needed.

Table 2.4: Results of consistency tests for the $D^+ \to K^-K^+\pi^+$ control mode for a variety of binning schemes and in regions of the DP. The table shows the p-values obtained for the individual magnet polarities (MagUp, MagDown) and for the combination of the two samples (Combined). The combined number for the whole DP with 129 bins is not available.

Region	Binning scheme	MagUp	MagDown	Combined
All	25 adaptive	89%	16%	34%
All	129 adaptive	25%	94%	
ϕ	≈ 30 uniform	65%	40%	66%
ϕ	≈ 100 uniform	11%	16%	42%
ϕ	≈ 300 uniform	31%	53%	20%
$\overline{K}^{*0}$	≈ 30 uniform	44%	58%	63%
$\overline{K}^{*0}$	≈ 100 uniform	22%	93%	85%
$\overline{K}^{*0}$	≈ 300 uniform	44%	53%	25%
middle	≈ 30 uniform	84%	10%	25%
middle	≈ 100 uniform	80%	83%	90%
middle	≈ 300 uniform	25%	88%	15%

Binning scheme	χ^2/ndf	p-value (%)
25 adaptive	32.0/24	12.7
106 adaptive	126.1/105	7.9
199 uniform	191.3/198	82.1
530 uniform	519.5/529	60.5

Table 2.5: Results of the CPV search in $D^+ \to K^-K^+\pi^+$ for four different binning schemes.

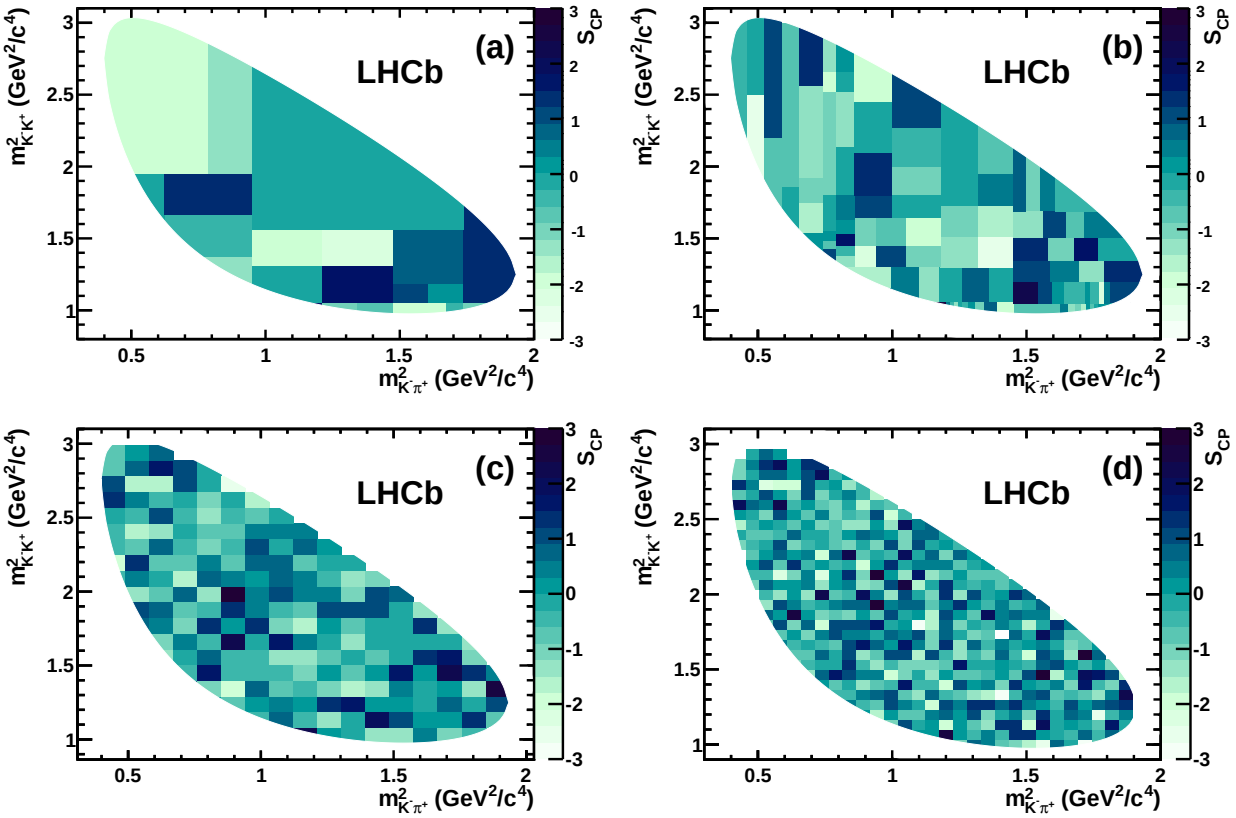

Figure 2.7: Distribution of the local asymmetry significance, S^i_{CP}, for $D^+ \to K^-K^+\pi^+$ for four binning schemes: (a) 25-bin adaptive, (b) 106-bin adaptive, (c) 199-bin uniform, (d) 530-bin uniform.

It is worth emphasizing that even with a small fraction of the LHCb data, this result implies strong constraints on direct CPV in charm decays. As we saw in eq. 2.17, direct CP asymmetries are approximated by $-2\,r\sin\Delta\theta\,\sin\Delta\phi$. Each of these three components (r, $\Delta\theta$, $\Delta\phi$) varies in a different way across the DP. Scanning the entire DP for local asymmetries lets us see the points in phase space where the three pieces align to give the largest effect, maximising the overall sensitivity. This was illustrated dramatically in subsequent studies of charmless B decays performed by other members of the LHCb collaboration, which found local asymmetries of up to $\approx 80\%$ [47]. The absence of signals in this analysis implies that the penguin amplitudes in $D^+ \to K^-K^+\pi^+$ are either heavily suppressed or closely aligned in phase with the tree amplitudes.

2.6 Search for CPV in $D^0 \to K^-K^+, \pi^-\pi^+$ (ΔA_{CP})

This section summarises three analyses: one with $35\,pb^{-1}$ of data from 2010 [48], one with $0.6\,fb^{-1}$ of data from 2011 [49], and one with $1.0\,fb^{-1}$ of data from 2011 [50]. Since all three use similar methodology, they are presented together. After this thesis had been written, a fourth analysis on $3.0\,fb^{-1}$ was made public, and is discussed briefly in Sec. 2.6.7.

2.6.1 Introduction and formalism

We turn to another search for CPV in singly Cabibbo-suppressed charm decays, this time considering two decay modes: $D^0 \to K^-K^+$ and $D^0 \to \pi^-\pi^+$. These are two-body decays of a pseudoscalar, so the situation is conceptually simpler than in Sec. 2.5: instead of a local asymmetry that varies across the phase space, we simply have an overall decay asymmetry for each final state. This was introduced previously in eq. 2.15 for direct CPV. We now extend it to allow for the presence of a time-dependent indirect asymmetry. For D^0 decays to a final state f (which for us will be a *CP* eigenstate accessible to both D^0 and $\overline{D}^0$),

$$A_{CP}(f;\,t) \equiv \frac{\Gamma(D^0(t) \to f) - \Gamma(\overline{D}^0(t) \to f)}{\Gamma(D^0(t) \to f) + \Gamma(\overline{D}^0(t) \to f)}. \tag{2.39}$$

In the limit of small mixing—which is certainly the case for charm—this may be written as: [51, 52]

$$A_{CP}(f;\,t) = a^{\rm dir}_{CP}(f) \;+\; \frac{t}{\tau}a^{\rm ind}_{CP}, \tag{2.40}$$

where $a^{\rm dir}_{CP}$ and $a^{\rm ind}_{CP}$ are the direct and indirect *CP* asymmetries, and where τ is the D^0 lifetime. Note that $a^{\rm dir}_{CP}$ depends on the final state f, whereas $a^{\rm ind}_{CP}$ is (to a good approximation) independent of f [36, 32] and is related to the observable A_Γ introduced earlier (eq. 2.24) by [29]

$$A_\Gamma = -a^{\rm ind}_{CP} - a^{\rm dir}_{CP}(f)\,y_{CP}. \tag{2.41}$$

The time-integrated asymmetry measured by an experiment, $A_{CP}(f)$, will depend on the decay-time acceptance of that experiment:

$$A_{CP}(f) = a^{\rm dir}_{CP}(f) \;+\; \frac{\langle t(f)\rangle}{\tau}a^{\rm ind}_{CP}, \tag{2.42}$$

where $\langle t(f)\rangle$ is the average decay time of the reconstructed and selected events used[38]. Thus, the *difference* in asymmetry between the decay modes $D^0 \to K^-K^+$ and $D^0 \to \pi^-\pi^+$ is given by:

$$\begin{aligned}
\Delta A_{CP} &\equiv A_{CP}(K^-K^+) - A_{CP}(\pi^-\pi^+) && (2.43)\\
&= a^{\rm dir}_{CP}(K^-K^+) - a^{\rm dir}_{CP}(\pi^-\pi^+) + \frac{\langle t(K^-K^+)\rangle - \langle t(\pi^-\pi^+)\rangle}{\tau}a^{\rm ind}_{CP} && (2.44)\\
&= \Delta a^{\rm dir}_{CP} + \frac{\Delta\langle t\rangle}{\tau}a^{\rm ind}_{CP}, && (2.45)
\end{aligned}$$

[38] For the special case of an unbiased time acceptance, as might be found at an e^+e^- B-factory, this simplifies to $a^{\rm dir}_{CP}(f) + a^{\rm ind}_{CP}$.

where the Δ denotes a difference between $D^0 \to K^-K^+$ and $D^0 \to \pi^-\pi^+$. Since the average time acceptance will be similar for the two final states, this has the effect of strongly suppressing the indirect CPV term[39]. The real reason for using ΔA_{CP} is experimental, as we'll see shortly, but we should first ask: is it a useful observable? As stated earlier, direct *CP* asymmetries depend upon the final state, so in general we do not expect cancellation between $a_{CP}^{\rm dir}(K^-K^+)$ and $a_{CP}^{\rm dir}(\pi^-\pi^+)$. More quantitatively, in the limit of U-spin symmetry we expect that the two final states have direct *CP* asymmetries that are equal in magnitude and opposite in sign [36], $a_{CP}^{\rm dir}(K^-K^+) = -a_{CP}^{\rm dir}(\pi^-\pi^+)$, maximising the size of ΔA_{CP}. In practice, U-spin can be broken through strong interaction effects [53]—but the key point is that we do not expect the two direct *CP* asymmetries to cancel in ΔA_{CP}.

So far we have discussed the underlying physical *CP* asymmetries. However, the basic quantities which we measure experimentally are event yields. We can construct raw asymmetries from them:

$$A_{\rm raw}(f) = \frac{N(D^0 \to f) - N(\overline{D}^0 \to f)}{N(D^0 \to f) + N(\overline{D}^0 \to f)}, \tag{2.46}$$

where N is a measured signal yield. The raw asymmetry includes the true *CP* asymmetry $A_{CP}(f)$ but also experimental effects, notably detection efficiency and production asymmetries, which we will discuss below. As a practical matter, it is necessary to separate $D^0 \to f$ from $\overline{D}^0 \to f$. Since the final states f are identical, the flavour of the D^0 must be tagged. Two methods are in common use at LHCb: tagging with D^{*+} decays and tagging with semileptonic B decays. In the analyses described here, we use D^{*+} tags, looking for a decay chain of the form ($D^{*+} \to D^0\pi^+$, $D^0 \to f$), or the conjugate process ($D^{*-} \to \overline{D}^0\pi^-$, $\overline{D}^0 \to f$). The charge of the soft pion indicates the flavour of the $D^0/\overline{D}^0$ at production[40]. The D^{*+} is easily separated from combinatoric background: the very small energy release means that it produces a sharp peak in the mass difference

$$\delta m \equiv m_{\rm cand}(D^{*+}) - m_{\rm cand}(D^0) - {\rm m}(\pi^+), \tag{2.47}$$

with small experimental resolution and natural width. Both D^{*+} produced at the primary vertex ("prompt") and D^{*+} produced in the decays of b-hadrons ("secondary") can be used, but in practice nearly all of our sample will consist of prompt charm. The other approach used at LHCb is to look for a secondary D^0 produced in association with a muon, from a decay of the form $\overline{B} \to D^0\mu^-X$; in that method, the charge of the muon indicates the flavour of the D^0 at decay. Results obtained with this second method will be discussed at the end of this section.

What we measure in practice, then, are the raw yields and their asymmetries:

$$A_{\rm raw}(f) = \frac{N[D^{*+} \to D^0(f)\pi^+] - N[D^{*-} \to \overline{D}^0(f)\pi^-]}{N[D^{*+} \to D^0(f)\pi^+] + N[D^{*-} \to \overline{D}^0(f)\pi^-]}. \tag{2.48}$$

The ratio of yields may be obtained from the asymmetries as:

$$\frac{N[D^{*+} \to D^0(f)\pi^+]}{N[D^{*-} \to \overline{D}^0(f)\pi^-]} = \frac{1 + A_{\rm raw}(f)}{1 - A_{\rm raw}(f)}. \tag{2.49}$$

The yields may be written as:

$$N[D^{*+} \to D^0(f)\,\pi^+] = P_+\,B_+(f)\,\varepsilon_+(f) \tag{2.50}$$
$$N[D^{*-} \to \overline{D}^0(f)\,\pi^-] = P_-\,B_-(f)\,\varepsilon_-(f), \tag{2.51}$$

[39] For the LHCb analyses presented here, $\Delta\langle t\rangle/\tau$ is approximately 10% (specifically, 0.10 ± 0.01 in the $1.0\,{\rm fb}^{-1}$ analysis).

[40] Because of D^0-$\overline{D}^0$ mixing, the flavour at production isn't necessarily the same as the flavour at decay. This implies a dilution factor, reducing the *CP* asymmetry. However, (a) the effect is small because charm mixing is small, and (b) it is a multiplicative correction, *i.e.* a couple of orders of magnitude smaller than something that's too small to measure. Therefore, we don't need to worry about it until that happy day when we are making precision measurements of *CP* asymmetries in charm.

where $P_\pm$ is the number of $D^{*\pm}$ produced in the LHCb acceptance, $B_\pm$ is the full branching fraction ($D^{*+} \to D^0\pi^+,\ D^0 \to f$), and $\varepsilon_\pm$ is the efficiency to reconstruct and select a $D^{*\pm}$ produced in the LHCb acceptance. Note that $P_\pm$ is manifestly independent of the subsequent decay mode. The ratio of the yields is then simply

$$\frac{N[D^{*+} \to D^0(f)\,\pi^+]}{N[D^{*-} \to \overline{D}^0(f)\,\pi^-]} = \frac{P_+\,B_+(f)\,\varepsilon_+(f)}{P_-\,B_-(f)\,\varepsilon_-(f)}. \tag{2.52}$$

Combining eq. 2.52 with repeated applications of the identity in eq. 2.49, we obtain

$$\frac{1+A_{\rm raw}(f)}{1-A_{\rm raw}(f)} = \left(\frac{1+A_P}{1-A_P}\right)\left(\frac{1+A_B(f)}{1-A_B(f)}\right)\left(\frac{1+A_\varepsilon(f)}{1-A_\varepsilon(f)}\right), \tag{2.53}$$

where A_P, $A_B(f)$, and A_ε are the production, branching fraction, and efficiency asymmetries. The branching fraction asymmetry here is the same as the *CP* asymmetry,

$$A_B(f) \equiv A_{CP}(f). \tag{2.54}$$

We can simplify things by noticing that the efficiency asymmetry is independent of the final state f *within a local area of phase space*[41]. To see this, we split the efficiency into parts:

$$\varepsilon_+(f) = \epsilon(D^{*+} \to D^0\pi^+)\,\epsilon(D^0 \to f) \tag{2.55}$$
$$\varepsilon_-(f) = \epsilon(D^{*-} \to \overline{D}^0\pi^-)\,\epsilon(\overline{D}^0 \to f) \tag{2.56}$$

But in a local region of phase space, the efficiencies to reconstruct $D^0 \to f$ and $\overline{D}^0 \to f$ are the same—it's the exact same final state f, with no difference in angular distribution *etc.* in the decay of the spin-0 D^0 meson. Therefore $\epsilon(D^0 \to f) = \epsilon(\overline{D}^0 \to f)$, and so they cancel in the ratio:

$$\frac{\varepsilon_+(f)}{\varepsilon_-(f)} = \frac{\epsilon(D^{*+} \to D^0\pi^+)}{\epsilon(D^{*-} \to \overline{D}^0\pi^-)} \tag{2.57}$$

Thus, in a local region of phase space, A_ε is independent of f. Taylor-expanding eq. 2.53 at second order and writing A_ε as independent of f, we obtain:

$$1 + 2A_{\rm raw}(f) + 2[A_{\rm raw}(f)]^2 \approx [1 + 2A_P + 2A_P^2]\,[1 + 2A_{CP}(f) + 2A_{CP}^2(f)]\,[1 + 2A_-\varepsilon + 2A_\varepsilon^2]. \tag{2.58}$$

At first order this reduces to

$$A_{\rm raw}(f) \approx A_P + A_{CP}(f) + A_\varepsilon, \tag{2.59}$$

the rather intuitive result that we can combine small asymmetries just by adding them. We also see immediately that A_P and A_ε will cancel in the difference between two decay modes:

$$A_{\rm raw}(K^-K^+) - A_{\rm raw}(\pi^-\pi^+) \approx A_{CP}(K^-K^+) - A_{CP}(\pi^-\pi^+) = \Delta A_{CP}. \tag{2.60}$$

The approximation here is the first-order Taylor expansion from eq. 2.59. We can, of course, go back and add higher-order terms if we wish—but in practice there is no need, for two reasons. First, we will work in a region of phase space where the nuisance asymmetries are small, $\mathcal{O}(10^{-2})$ or less, such that the second-order terms are below $\mathcal{O}(10^{-4})$ and are smaller than our level of sensitivity by at least an order of magnitude. Second, in the absence of a physics asymmetry ($A_{CP} = 0$) the nuisance asymmetries cancel at all orders and the expected value is exactly zero. This, in short, is why we focus on ΔA_{CP} as an observable: it elegantly removes a whole slew of experimental effects which we would otherwise have to measure, and which would come with unacceptably large systematic uncertainties.

[41] As the alert reader is no doubt already thinking, this means that we will have to take precautions when combining different parts of phase space to obtain an overall asymmetry.

2.6.2 Kinematic binning and reweighting

There are a few subtleties in the experimental procedure. The most important is that the method outlined above is only strictly correct if carried out within a local area of phase space. If we make naive measurements of the charge asymmetries integrated across the entire phase space for $D^0 \to K^-K^+$ and $D^0 \to \pi^-\pi^+$, we risk introducing second-order effects in ΔA_{CP}. This is perhaps easiest to understand with a toy example. Suppose that we have two regions of phase space, A and B. Suppose also that there is no true *CP* asymmetry, and that we have huge samples so that statistical errors are negligible. In region A, there is a charge asymmetry in the soft pion detection efficiency, $A_\varepsilon = 0.1$, but in region B the asymmetry is zero. Let's also say that the ratios of efficiencies to select $D^0 \to K^-K^+$ and $D^0 \to \pi^-\pi^+$ are different in the two regions[42], so that for K^-K^+ the yields are equal in A and B but for the $\pi^-\pi^+$ mode the yield is four times larger in A than in B. Neither of these effects is a problem in itself, and if we measure ΔA_{CP} in A and in B separately they will not cause a bias. (The soft pion charge asymmetry in A will affect both K^-K^+ and $\pi^-\pi^+$ decays and vanish in the difference, and the $K^-K^+/\pi^-\pi^+$ efficiency difference in B may reduce the statistical precision but will not affect the asymmetry measurements.) However, if we fail to separate the data from regions A and B, we'll have a problem: the K^-K^+ mode has equal yields from both regions but the $\pi^-\pi^+$ mode is more strongly weighted towards region A. So the average raw asymmetry in K^-K^+ will be around 0.05 (*i.e.* an equally weighted average of 0.10 and 0) but in $\pi^-\pi^+$ it will be around 0.08 (*i.e.* a 4 : 1 weighted average of 0.10 and 0). That is, there will be a non-cancelling portion of the asymmetry—0.03 in this toy example—in ΔA_{CP}. More generally, effects like this occur when the $K^-K^+/\pi^-\pi^+$ yield ratio and the asymmetry sum from detector effects ($A_P + A_\varepsilon$) both vary within the phase space of which we integrate.

There is a very simple solution to the problem outlined above: you can divide the phase space up into kinematic bins that are small enough so that there isn't significant coherent variation of the ratio and asymmetry within a given bin. (The data must also be split by magnet polarity and trigger status for similar reasons.) Then you simply measure ΔA_{CP} in each bin independently and combine the results. This approach was used in all three of the analyses. Some care is required when choosing the binning scheme: it must be fine enough (and in the right variables) to protect against the coherent variation effect, but increasing the number of fits poses its own practical problems—not just that adding to the total number of free parameters will reduce the overall statistical precision, but also that the proper behaviour and convergence of all of the fits must be ensured. In the first analysis on $35\,\text{pb}^{-1}$, the data were split into a total of 12 kinematic bins by the p_T and pseudorapidity (η) of the D^0 meson, then further split by magnet polarity and trigger configuration for a total of 48 subsamples. In the second analysis on $0.6\,\text{fb}^{-1}$, this was extended to include a binning in the soft pion momentum (for a total of 54 kinematic bins) and divided by left/right detector side as well as magnet polarity and data-processing version, for a total of 216 subsamples. A similar approach was used in the $1.0\,\text{fb}^{-1}$ analysis, though with a modified partition[43].

However, this method does not scale well: although the systematic uncertainty is small (see later), managing such a large number of fits is a complex and error-prone task. In addition, the sophistication of the fits is limited compared to what could be done with the whole data sample because the individual yields are reduced by a couple of orders of magnitude. A better method is to reweight the data so that the $D^0 \to K^-K^+$ and $D^0 \to \pi^-\pi^+$ samples have the same kinematic distribution (or, at least, the same for all variables that are relevant to D^* production or soft pion efficiency asymmetries); this removes potential biases due to the coherent variation effect entirely. This method was adopted for the $1.0\,\text{fb}^{-1}$ analysis, with the binning approach described above serving as a cross-check. The reweighting was done in two steps: a 2D weighting in the $|p|$ and p_T of the D^{*+}, followed by a 1D weighting in the azimuthal angle ϕ of the D^{*+}. Although this is not the full set of kinematic observables, the

[42] Differences of this kind (though generally less extreme than in the toy example) can arise because of the RICH particle identification system performance, or even simply from the difference in energy release of the two decays.

[43] The data were reprocessed for this analysis, so that split could be removed; instead a separation by hardware trigger decision was added.

other relevant quantities (*e.g.* the soft pion momentum) are sufficiently correlated with them that they are also equalized for $D^0 \to K^-K^+$ and $D^0 \to \pi^-\pi^+$ after reweighting. In detail, the procedure is to obtain the kinematic distributions for the two decay modes separately, using sWeights in δm to separate signal from background and splitting the data into subsamples by magnet polarity and hardware trigger decision. We then produce normalised histograms of these distributions—one 2D histogram for $(|p|, p_{\mathrm{T}})$ and one 1D histogram for ϕ—and take their ratio. For a given $D^0 \to K^-K^+$ candidate we look at each histogram, see which bin it falls into, and find the value of that ratio in that bin; its weight is the product of those ratios. The distribution of the weights is peaked at 1, with nearly all weights between 0.5 and 2.0. (The weights for $D^0 \to \pi^-\pi^+$ candidates are simply 1.)

2.6.3 Reconstruction and Selection

We now turn to the data. As outlined above, we reconstruct candiates in the decay chains $D^{*+} \to D^0\pi^+$, $D^0 \to K^-K^+$, $\pi^-\pi^+$. Events must first pass the L0 hardware trigger, either because one of the D^0 daughters deposits enough transverse energy in the calorimeter, or because a particle from outside the D^{*+} decay chain fires the trigger[44]. The former path is referred to as TOS (Triggered On Signal), and the latter as TIS (Triggered Independently of the Signal)[45]. D^0 candidates must also pass the software trigger. Offline selection criteria are applied, including requirements that the decay chain have the expected topology: the D^0 and the soft pion should originate at a primary vertex, the D^0 daughter tracks should meet at a common vertex, the D^0 decay vertex should be displaced from its origin, and the direction of the D^0 momentum should be consistent with the displacement vector between its origin and decay vertices. The D^0 daughter tracks are also required to pass particle identification requirements for pions or kaons, as appropriate, suppressing background from misidentified charm decays. For the $1.0\,\mathrm{fb}^{-1}$ analysis, a further refitting step was added in which the D^{*+} was constrained in the fit to originate at a PV. This improves the δm resolution significantly, reducing the signal width by a factor of 2–3. (This is so effective because the soft pion is both less precisely measured than the other tracks and nearly collinear with the D^0.)

In addition, starting with the $0.6\,\mathrm{fb}^{-1}$ analysis we require that the candidate lie within a fiducial kinematic region. This is needed to ensure that the efficiency asymmetry for the tagging soft pion is indeed small throughout the phase space used, as we assumed for the formalism. Because the soft pion has low momentum (typically a few GeV/c), the dipole field at LHCb is strong (bending power of about 4 Tm), and the LHCb acceptance is narrow (around 300 mrad), the pions may be swept out of the LHCb acceptance entirely. Moreover, for a given magnet polarity and kinematic configuration, this depends strongly on the pion charge. For example, suppose that the magnetic field is in the up direction and that the soft pion has a momentum vector of $(+200, 0, 2000)\,\mathrm{MeV}/c$. The magnetic field will bend π^+ to the left ($-x$ direction) and π^- to the right ($+x$ direction). So a π^+ would be swung back left towards the centre of the detector and is likely to be detected, whereas a π^- would be pushed further right and would not reach the downstream tracking stations. This is illustrated in the upper row of Fig. 2.8, along with the fiducial cuts imposed to eliminate those regions of large local asymmetry. There is an additional geometrical effect arising from the hole in the acceptance due to the beampipe, illustrated for tracks with small $|p_y|$ in the lower row of Fig. 2.8. These regions of large asymmetry are also removed.

For D^{*+} candidates passing the selection in the $1.0\,\mathrm{fb}^{-1}$ sample, the $m(K^-K^+)$ and $m(\pi^-\pi^+)$ distributions are shown in Fig. 2.9, and the δm distributions in Fig. 2.10. Note that these are 1D

[44] Between them, these two possibilities cover nearly all the ways that the hardware trigger can be activated. They exclude certain technical/diagnostic triggers, and more importantly they also exclude the rare events in which only the soft pion fires the trigger. We want to exclude the latter because their charge efficiency asymmetry could be more complicated to understand.

[45] In the usual LHCb convention, these are not mutually exclusive since events may be both TOS and TIS (*e.g.* in an event where the energy deposit from one of the D^0 daughters fires the calorimeter trigger, and in addition so does the calorimeter deposit or a muon station track of a particle from the decay of another charmed hadron). For the purposes of the ΔA_{CP} analysis we divide the data into two disjoint sets: candidates with a D^0 daughter that is TOS on the hadron calorimeter trigger, and candidates that do not fulfil the TOS requirement but are triggered as TIS.

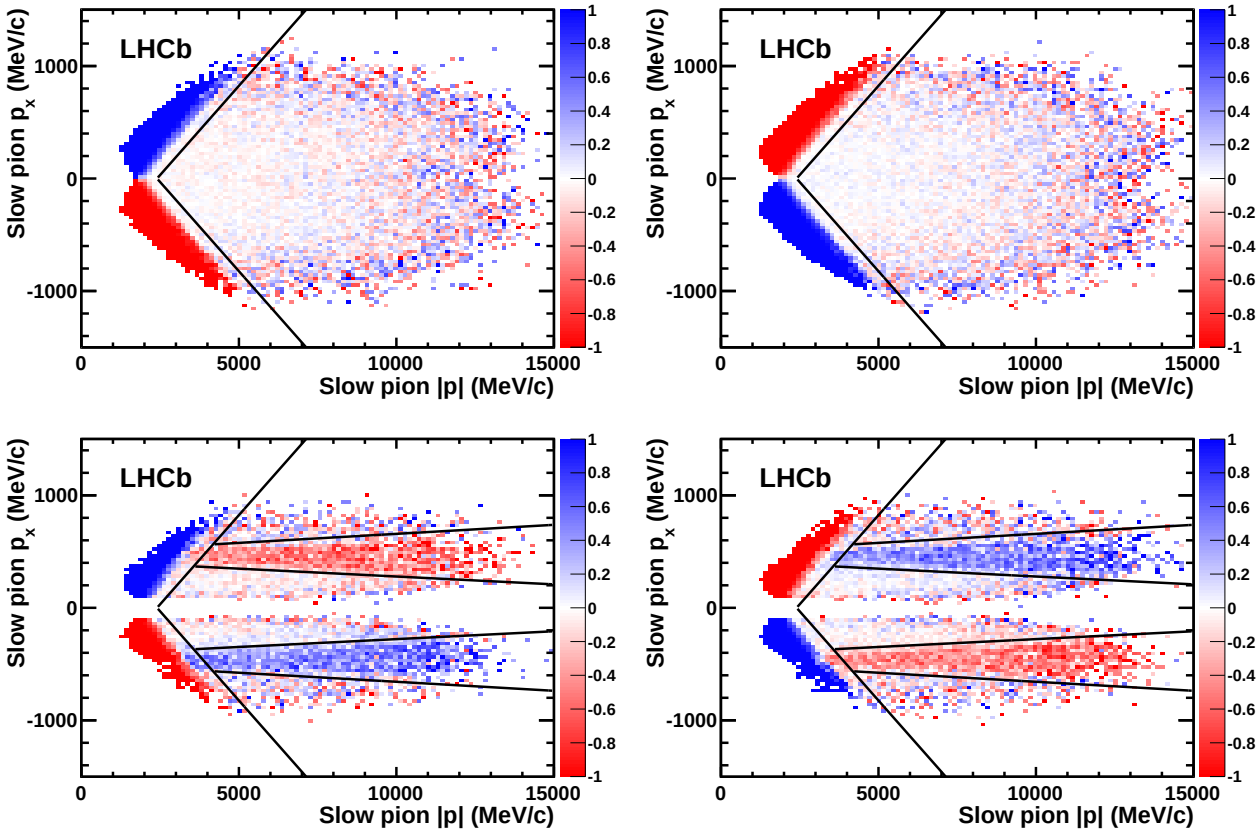

Figure 2.8: Raw asymmetry in bins of soft pion p_x vs $|p|$ for $D^{*+} \to D^0\pi^+$, $D^0 \to K^-K^+$ candidates. Upper row: candidates with $|p_y/p_z| > 0.02$. Lower row: candidates with $|p_y/p_z| < 0.02$ (beam pipe region). Left column: magnet polarity up. Right column: magnet polarity down. The fiducial cuts are marked with solid black lines, and exclude the regions of large asymmetry.

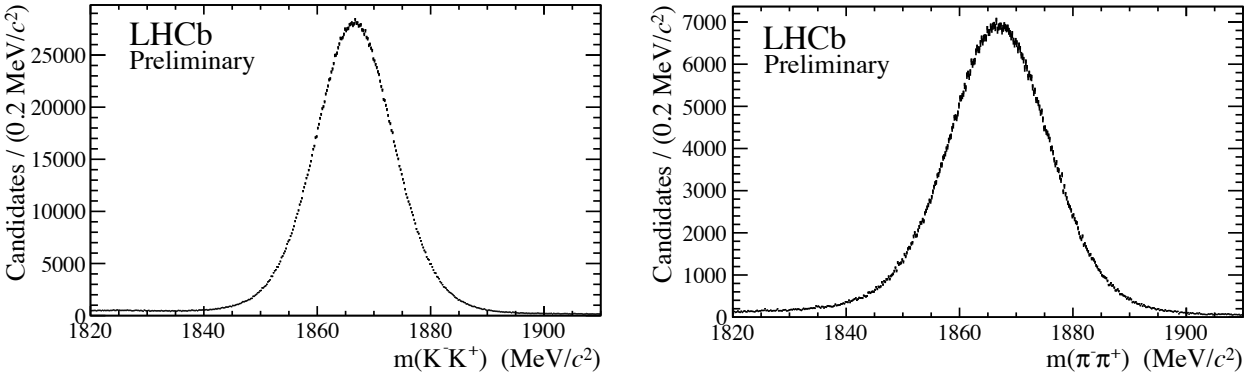

Figure 2.9: Fits to the $m(K^-K^+)$ and $m(\pi^-\pi^+)$ spectra of D^{*+} candidates passing the selection and satisfying $0 < \delta m < 12\,\mathrm{MeV}/c^2$.

Table 2.6: Yields for the various signal and control samples used to measure ΔA_{CP}. The D^0 decay mode is indicated, along with whether it was tagged by a $D^{*+} \to D^0\pi^+$ decay.

Analysis	Sample	Signal yield
$35\,\mathrm{pb}^{-1}$	Untagged $K^-\pi^+$	5.1×10^6
$35\,\mathrm{pb}^{-1}$	Tagged $K^-\pi^+$	1.0×10^6
$35\,\mathrm{pb}^{-1}$	Tagged K^-K^+	1.2×10^5
$35\,\mathrm{pb}^{-1}$	Tagged $\pi^-\pi^+$	3.6×10^4
$0.6\,\mathrm{fb}^{-1}$	Tagged K^-K^+	1.44×10^6
$0.6\,\mathrm{fb}^{-1}$	Tagged $\pi^-\pi^+$	0.38×10^6
$1.0\,\mathrm{fb}^{-1}$	Tagged K^-K^+	2.24×10^6
$1.0\,\mathrm{fb}^{-1}$	Tagged $\pi^-\pi^+$	0.69×10^6

projections of a 2D distribution, and in particular that the same $D^0 \to h^-h^+$ combination may appear more than once in Fig. 2.9 if there is more than one candidate in an event. This occurs in approximately 6–10% of cases, and is almost always due to a single D^0 being compatible with more than one soft pion. This is entirely normal and expected—many pions are produced at an event primary vertex—and does not need any special handling[46]. For the δm fits and asymmetry measurement, the D^0 candidate mass is required to lie in the narrow window 1844–1884 MeV/c^2. The yields obtained in the three analyses are shown in Table 2.6.

2.6.4 Fit procedure and results

The fit procedure was updated over the three analyses as more data were added, and as we passed from a strategy of performing many independent fits in kinematic bins to one of performing a small number of fits to weighted data. In each case, the baseline results use 1D fits to δm distributions, with signal and background components. The signal peak is described by the convolution of (the sum of n Gaussian functions with the same mean but different widths) and a function B that improves the

[46] There is often a temptation to remove candidates until only one remains, either at random or according to a figure of merit such as a vertex χ^2. There are cases when this is appropriate, notably for self-cross-feed when a single decay can produce multiple correlated candidates peaking at the same place, but it can be actively harmful if misapplied. For us it would reduce the signal efficiency in a way which is correlated in a hard-to-understand way with the background level, and probably with the decay kinematics. It would therefore mean exchanging a small amount of combinatoric background for a tricky systematic uncertainty—not a good trade-off.

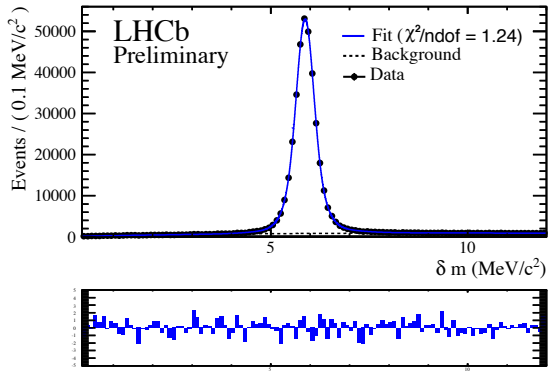

K^-K^+, magnet up, TOS

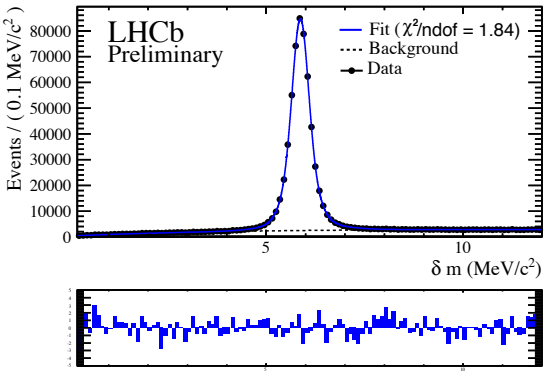

K^-K^+, magnet up, TIS

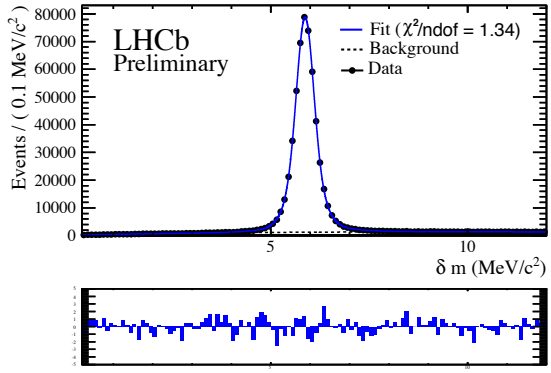

K^-K^+, magnet down, TOS

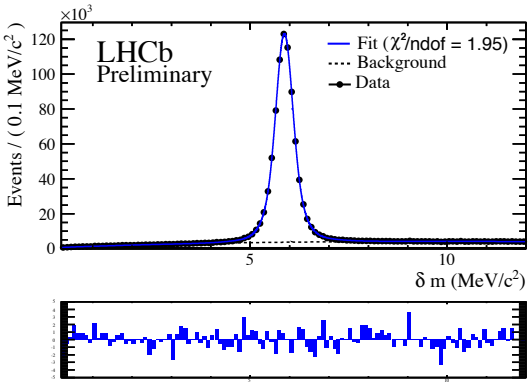

K^-K^+, magnet down, TIS

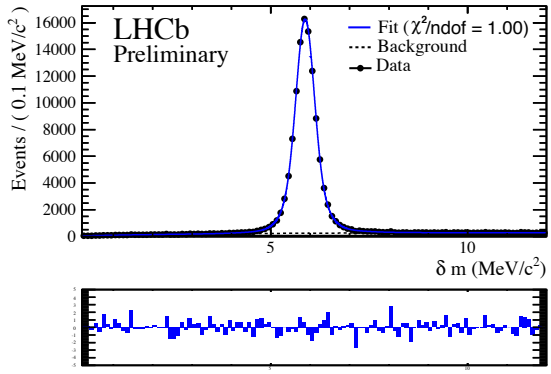

$\pi^-\pi^+$, magnet up, TOS

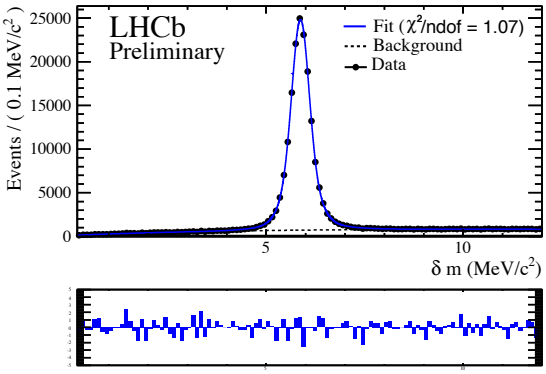

$\pi^-\pi^+$, magnet up, TIS

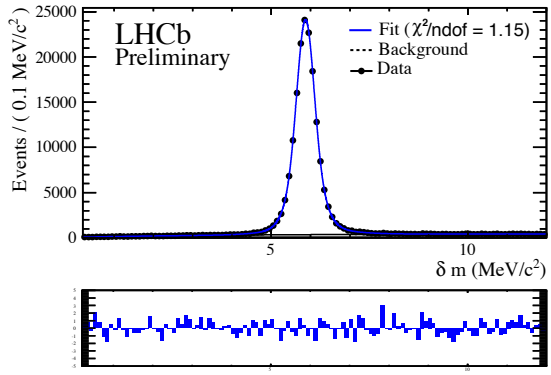

$\pi^-\pi^+$, magnet down, TOS

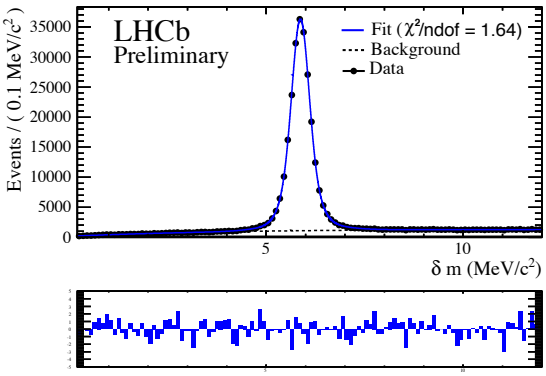

$\pi^-\pi^+$, magnet down, TIS

Figure 2.10: Fits to the δm spectra of D^{*+} candidates passing the selection and with $1844 < m(D^0) < 1884\,\mathrm{MeV}/c^2$.

description of the tails:

$$B(x;s) = \Theta(x)\, x^s, \tag{2.61}$$

where Θ is the Heaviside function and the parameter s typically takes a value a little greater than -1. For the $35\,\mathrm{pb}^{-1}$ and $0.6\,\mathrm{fb}^{-1}$ analyses we use $n = 2$ Gaussian functions, and for the $1.0\,\mathrm{fb}^{-1}$ analysis we use $n = 3$ Gaussian functions. The combinatorial background is described by an empirical threshold function. For the $35\,\mathrm{pb}^{-1}$ and $0.6\,\mathrm{fb}^{-1}$ analysis it is of the form

$$f(\delta m) = 1 - e^{-(\delta m - \delta m_0)/\alpha}, \tag{2.62}$$

where δm_0 and α are free parameters describing the threshold and shape, respectively; and for the $1.0\,\mathrm{fb}^{-1}$ analysis it is of the form

$$f(\delta m) = (\delta m - \delta m_0)^\beta\, e^{-(\delta m - \delta m_0)/\alpha}, \tag{2.63}$$

where β is an additional free parameter. For a particular subsample, the D^{*+} and D^{*-} events are fitted simultaneously so that the raw asymmetry and its uncertainty are obtained directly from the fit. The D^{*+} and D^{*-} events share nearly all shape parameters, except for a charge-dependent offset in the signal peak position and a charge-dependent scale factor in the signal peak width (and not even those for the $35\,\mathrm{pb}^{-1}$ analysis). By contrast, no free parameters are shared between the different D^0 decay modes (K^-K^+, $\pi^-\pi^+$), nor between different subsamples (magnet polarities, kinematic bins if appropriate, etc). This ensures that the fits are statistically independent and simplifies the propagation of statistical uncertainties. Asymmetries in the background yield are also allowed in the fit, but don't have any particular physical significance.

After the fits, we have measurements of the raw asymmetries $A_{\mathrm{raw}}(K^-K^+)$ and $A_{\mathrm{raw}}(\pi^-\pi^+)$ for each of the independent subsamples. As shown in eq. 2.59, these raw asymmetries include production and detector effects—and those effects can and do vary depending on the particles' kinematics, the magnet polarity, the detector conditions, *etc.*, so we do not attempt to assign them any physical significance. However, the differences are meaningful. For each subsample we obtain a statistically independent measurement of ΔA_{CP}. When using the kinematic binning approach this amounts to a very large number of measurements which are not given here in full but which are internally consistent ($\chi^2/\mathrm{NDF} = 211/215$, for a p-value of 56% with $0.6\,\mathrm{fb}^{-1}$). The results among the subsamples obtained with the weighting method in the $1.0\,\mathrm{fb}^{-1}$ are shown in Table 2.7. Again, the values of ΔA_{CP} measured among the subsamples are consistent ($\chi^2/\mathrm{ndof} = 0.9/3$). In each analysis, the individual ΔA_{CP} measurements were combined in a weighted average, obtaining:

$$\begin{aligned} 35\,\mathrm{pb}^{-1}: &\quad (-0.28 \pm 0.70)\%, \\ 0.6\,\mathrm{fb}^{-1}: &\quad (-0.82 \pm 0.21)\%, \\ 1.0\,\mathrm{fb}^{-1}: &\quad (-0.34 \pm 0.15)\%, \end{aligned}$$

where the uncertainties are statistical only.

Some time was spent understanding the change in the central value between the $0.6\,\mathrm{fb}^{-1}$ and $1.0\,\mathrm{fb}^{-1}$ analyses. Several effects contribute. We will step through the changes between the two, looking at the effect on ΔA_{CP} at each stage.

Reconstruction software check: First and foremost are several statistical effects: the $0.6\,\mathrm{fb}^{-1}$ sample is not a simple subset of the $1.0\,\mathrm{fb}^{-1}$ sample. The data were reprocessed with a new calibration and a new version of the reconstruction software. This increased the yields (see Table 2.6), especially for the $D^0 \to \pi^-\pi^+$ sample which dominates the statistical uncertainty. Further, some of the events previously used were no longer selected[47], corresponding to about 15% of the K^-K^+

[47] Note that the selection cuts themselves did not change. However, some events which previously passed the cuts now fail, and vice versa. This is true even for straightforward quantities like p_{T}: rerunning the construction with a new calibration will in general give different results, so some events will migrate in or out. This goes double for more complex quantities, like the vertex fit χ^2 and the output of the multivariate particle identification selector, which are especially sensitive to changes in conditions.

Table 2.7: Measured asymmetries from the fits of the $1.0\,\text{fb}^{-1}$ analysis using the weighting method, with statistical uncertainties only. The data are divided into disjoint samples according to the D^0 decay mode, the magnet polarity, and the hardware trigger category. (Here TIS indicates that the event was triggered TIS and was not triggered TOS on the D^0.)

Quantity	Magnet polarity	Hardware trigger decision	Observed value [%]
$A_{\text{raw}}(K^-K^+)$	Up	TOS	-1.35 ± 0.18
$A_{\text{raw}}(K^-K^+)$	Down	TOS	-0.45 ± 0.15
$A_{\text{raw}}(\pi^-\pi^+)$	Up	TOS	-0.73 ± 0.31
$A_{\text{raw}}(\pi^-\pi^+)$	Down	TOS	-0.08 ± 0.26
$A_{\text{raw}}(K^-K^+)$	Up	TIS	-1.72 ± 0.15
$A_{\text{raw}}(K^-K^+)$	Down	TIS	$+0.12 \pm 0.12$
$A_{\text{raw}}(\pi^-\pi^+)$	Up	TIS	-1.43 ± 0.26
$A_{\text{raw}}(\pi^-\pi^+)$	Down	TIS	$+0.34 \pm 0.22$
ΔA_{CP}	Up	TOS	-0.62 ± 0.36
ΔA_{CP}	Down	TOS	-0.36 ± 0.30
ΔA_{CP}	Up	TIS	-0.30 ± 0.30
ΔA_{CP}	Down	TIS	-0.22 ± 0.25

sample and 14% of the $\pi^-\pi^+$ sample. As a starting point and to check that there is no bias due to the reconstruction software and calibration, we measure ΔA_{CP} with the method of the $0.6\,\text{fb}^{-1}$ analysis on the set of events that were selected by both analyses, first when the events are reconstructed with the previous code and calibration, and second with the new version. The two values obtained are $(-0.80 \pm 0.23)\%$ and $(-0.78 \pm 0.23)\%$. Thus, the two versions of the reconstruction software give fully consistent results when applied to the same set of events. These are also consistent with the result obtained on the full $0.6\,\text{fb}^{-1}$ sample with the old analysis.

New events in the first $0.6\,\text{fb}^{-1}$: In addition to this overlap sample, there are two groups of new events added in the $1.0\,\text{fb}^{-1}$ analysis. The first comprises additional events in the first $0.6\,\text{fb}^{-1}$, with yields of approximately 0.21×10^6 for K^-K^+ and 0.11×10^6 for $\pi^-\pi^+$, corresponding to about 17% and 34% of the yields in the first $0.6\,\text{fb}^{-1}$. The $\pi^-\pi^+$ sample gains disproportionately from changes to the RICH calibration, effectively improving the efficiency of the PID cut. The value of ΔA_{CP} evaluated in the first $0.6\,\text{fb}^{-1}$ with these additional events included, but still using the methodology of the $0.6\,\text{fb}^{-1}$ analysis, is $(-0.55 \pm 0.21)\%$.

New events in the last $0.4\,\text{fb}^{-1}$: The second set of new events comes from the final $0.4\,\text{fb}^{-1}$ of data taken in 2011. When ΔA_{CP} is measured on this subsample alone (still using the methodology of the $0.6\,\text{fb}^{-1}$ analysis), a value of $(-0.28 \pm 0.26)\%$ is obtained; and when fitting the full $1.0\,\text{fb}^{-1}$ as a block, a value of $(-0.45 \pm 0.16)\%$ is obtained.

Change from kinematic binning to reweighting: One important difference between the old and the new analysis is a change from kinematic binning to weighting. While this involves quite large technical changes to how the fits are carried out, it makes essentially no difference to the results: the value of ΔA_{CP} becomes $(-0.45 \pm 0.17)\%$.

Primary vertex constraint: The other important change is the constraint that the D^0 and soft pion meet at a primary vertex, which improves the δm resolution substantially as noted in Section 2.6.3. This in turn gives better background rejection and reduces the statistical uncertainty. With this change, the measured value of ΔA_{CP} becomes $(-0.34 \pm 0.15)\%$, corresponding to a shift of $+0.11\%$. The expected variation from statistical effects alone has a standard deviation of 0.05% (evaluated with toy experiments). The change seen is marginally consistent with being

purely statistical, being just over 2σ. In addition, a systematic effect associated with excluding events in which the soft pion does not point to the PV is considered (see later), with a size of 0.08%. Taking this into account, the results are consistent with uncertainties.

The pattern that emerges is fairly clear and more than a little disheartening: while the central value of the first $0.6\,\text{fb}^{-1}$ was intriguingly far from zero, with each addition of new events or improvement in statistical precision, the central value moves steadily in the direction of zero. While there may still be a modest level of real CPV present, the behaviour closely tracks what would be seen following a large statistical fluctuation in a sample whose underlying value is zero.

2.6.5 Systematic uncertainties and checks

A similar set of systematic uncertainties were considered for each of the three analyses, with the treatment becoming gradually more precise and more sophisticated as data were added. In most cases there is a substantial statistical component. The uncertainties are summarised in Table 2.8. To avoid repetition, we focus here on the uncertainties for the most recent analysis. They consist of:

Fiducial cut: The fiducial cuts were loosened (see dashed line in Fig. 2.8). By pushing closer to the large-asymmetry zone, we test whether we may be affected by its tails. The systematic uncertainty is assigned based on the difference in the value of ΔA_{CP} measured.

Peaking background: Because we fit only the δm distribution, we are in principle vulnerable to background components which peak in δm. These can occur from misreconstructed D^{*+} decays. For example, suppose that the decay $D^{*+} \to D^0\pi^+, D^0 \to K^-\pi^+\pi^0$ occurs and we find all of the charged tracks successfully but misidentify the D^0 daughter π^+ as a K^+ (and ignore the π^0). Because we found most of the D^0 momentum and the soft pion, the value of δm will be roughly correct (though with a degraded resolution). The D^0 candidate mass will be a smooth function and will not peak in the right place—but some fraction of the events will end up in our signal window and be selected (since some energy is lost due to the missing π^0 and some is gained back due to the $\pi \to K$ misidentification). In practice the rate of such events is small, due to the mass and PID cuts, but it is not zero. The systematic uncertainty is assigned by changing the fit procedure to fit the $m(K^-K^+)$ and $m(\pi^-\pi^+)$ distributions in the δm signal window (and, separately, sidebands) instead of fitting δm in the $m(h^-h^+)$ signal window. The modified procedure eliminates this class of peaking background entirely. The systematic uncertainty is assigned based on the difference in the value of ΔA_{CP} measured.

Fit procedure: To check that the result does not depend on the details of the signal shapes and fit procedure, we remeasure ΔA_{CP} without any fitting whatsoever, instead counting candidates and using sideband subtraction to obtain signal yields. The systematic uncertainty is assigned based on the difference found.

Multiple candidates: As discussed in Sec. 2.6.3, for events in which more than one candidate passes the full selection, we retain all of them. Broadly speaking this is the right thing to do, but it could conceivably introduce a bias if there were an unknown source of correlated multiple candidates (*e.g.* duplicate tracks introduced by some software bug) that were not eliminated by existing clone-removing tools and which occurred at different rates for D^{*+} and D^{*-}. To check for this, we apply an algorithm to reject all candidates but one (chosen at random) for each event and remeasure ΔA_{CP}. The difference found is assigned as a systematic uncertainty.

Kinematic weighting: If the procedure does not equalize the kinematic distributions fully, there might be residual second-order effects. To bound the scale of this effect, we turn off the reweighting entirely and repeat the measurement: this should give a larger distortion. It's nonetheless small in absolute terms and we assign the difference seen as a systematic uncertainty.

Table 2.8: Systematic uncertainties on ΔA_{CP} for the three analyses. For the $35\,\text{pb}^{-1}$ analysis, the uncertainty denoted "peaking background" corresponds to the effect of varying the cut on the D^0 mass window.

Source	$35\,\text{pb}^{-1}$	$0.6\,\text{fb}^{-1}$	$1.0\,\text{fb}^{-1}$
Fiducial cut	—	0.01%	0.02%
Peaking background	0.20%	0.04%	0.04%
Fit procedure	0.06%	0.08%	0.03%
Multiple candidates	0.13%	0.06%	0.01%
Kinematic binning/weighting	0.01%	0.02%	0.01%
Soft pion χ^2_{IP}	—	—	0.08%
Total	0.25%	0.11%	0.10%

Soft pion χ^2_{IP}: Events are present in which the soft pion has a large impact parameter χ^2 with respect to the primary vertex[48]. This is primarily due to multiple scattering of the soft pion. (Secondary D^{*+} could also contribute in principle, but the tight pointing requirement on the D^0 means they are subdominant.) However, the vertex fit constrains the soft pion to originate at the PV. This could distort the δm spectrum. While the effect is not expected to be large, a systematic uncertainty is assigned because a dependence of ΔA_{CP} on the soft pion χ^2_{IP} cannot be excluded with the $1\,\text{fb}^{-1}$ data sample (see Fig. 2.11).

Numerous other crosschecks were carried out, including: monitoring the value of ΔA_{CP} as a function of the time at which the data were taken; tightening particle identification requrements; using a different D^{*+} selection; testing different fit functions/lineshapes; computing ΔA_{CP} with the previous kinematic binning procedure; applying muon and electron vetoes to the soft pion and the D^0 daughters; validation of the statistical uncertainties with toy experiments; testing for dependence of the result on the event occupancy (track and PV multiplicity); and measuring ΔA_{CP} in a large sample of simulated events to verify that the procedure is unbiased. The analysis is found to be robust against systematic effects.

Including systematic uncertainties, the measured values of ΔA_{CP} were found to be

$$\begin{aligned} 35\,\text{pb}^{-1}: &\quad (-0.28 \pm 0.70 \pm 0.25)\%, \\ 0.6\,\text{fb}^{-1}: &\quad (-0.82 \pm 0.21 \pm 0.11)\%, \\ 1.0\,\text{fb}^{-1}: &\quad (-0.34 \pm 0.15 \pm 0.10)\%. \end{aligned}$$

A separate measurement of ΔA_{CP} on an independent dataset, in which the D^0 is produced in a semileptonic b-hadron decay, gave a value of $(+0.14 \pm 0.16 \pm 0.08)\%$ with $3\,\text{fb}^{-1}$ of data [54].

2.6.6 Conclusions

The current HFAG world average of ΔA_{CP} is $(-0.257 \pm 0.104)\%$, consistent with no CP violation at the 1.8% confidence level [24]. This is illustrated in Fig. 2.12. The result on the $0.6\,\text{fb}^{-1}$ sample, which had a significance of 3.5σ and was in agreement with similar results from CDF [55] and Belle [56], caused some excitement and seemed to suggest that an unexpected observation of *CP* violation in charm might be around the corner. Sadly, it seems to be suffering the fate of many 3σ results: subsequent measurements suggest that it was a fluctuation. (Optimistically, it might have been a fluctuation not from zero but from a *CP* asymmetry of order 10^{-3}.)

One happy consequence was that a good deal of progress was made on the question of *CP* violation in charm decays, and in particular what amount and type of direct CPV could be accommodated within the SM. Previously, predictions had generally been of order 10^{-3} or less. We now understand that the

[48] Formally, this is defined as the difference in the primary vertex fit χ^2 when the soft pion is included or excluded.

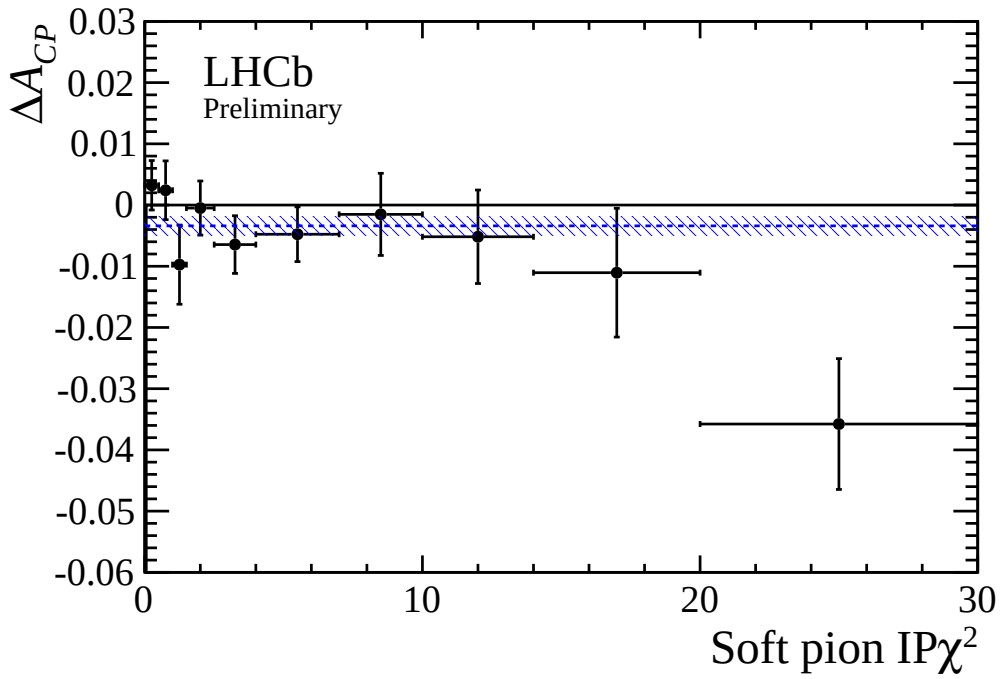

Figure 2.11: The value of ΔA_{CP} as a function of $\chi^2_{\rm IP}$ of the soft pion to the associated primary vertex. The data are divided into disjoint bins of $\chi^2_{\rm IP}$ and in each bin the analysis is performed, including further division into subsamples by trigger category and magnet polarity, except that for simplicity kinematic reweighting is not used. The measured value of ΔA_{CP} in each bin is indicated by the point and vertical error bar, and the extent of each bin by the horizontal error bar. The final point also includes all overflow events ($\chi^2_{\rm IP} > 30$). The horizontal line indicates the average ΔA_{CP} across all bins, and the hatched band indicates the 1σ error band around the average. The χ^2 consistency with a constant distribution is 7%.

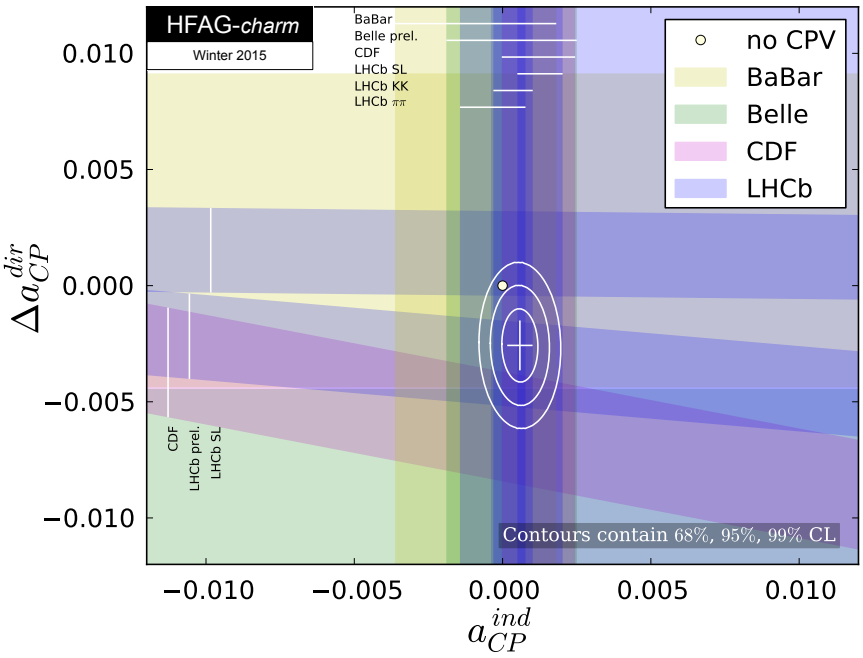

Figure 2.12: Combination plot for *CP* asymmetries in $D^0 \to K^-K^+$, $\pi^-\pi^+$ by HFAG [24]. The x-axis gives the indirect *CP* asymmetry (under the assumption that it is universal among *CP* eigenstates) and the y-axis gives the difference in direct *CP* asymmetry, equivalent to ΔA_{CP}. Diagonal bands, such as that for the measurement presented here, arise because the observable used is also sensitive to indirect CPV (see Sec. 2.6.1).

uncertainties on these estimates are larger than had been realised: QCD power corrections can enhance the penguin contribution (eq. 2.9) and thereby increase the *CP* asymmetry (eq. 2.17), and while the power corrections are not expected to be huge, there is no fundamental reason why they could not be. Indeed, the case of $D^0 \to K^-K^+$ and $D^0 \to \pi^-\pi^+$ is a special one: if both decays were tree-dominated, one would naively expect the branching fraction for $\pi^-\pi^+$ to be larger than that for K^-K^+, due to the difference in phase space. In fact the opposite is true, with $\mathcal{B}(D^0 \to K^-K^+)/\mathcal{B}(D^0 \to \pi^-\pi^+) \simeq 2.8$. An enhanced penguin contribution would naturally produce such an effect, and if it is interpreted as being solely due to penguin enhancements then one would expect a value of ΔA_{CP} of several permille [57, 58, 53, 38]. Thus, the current central value could easily be accommodated within the SM. Improved measurements of ΔA_{CP} are still worth pursuing experimentally, but absent a breakthrough in theoretical engineering it will not be possible to uncover new physics in this mode. By contrast, modes with $\Delta I = 3/2$ are much less susceptible to SM contamination and may yet reveal NP.

2.6.7 Afterword

After this thesis had been written, a new LHCb measurement of ΔA_{CP} was completed on the full $3\,\text{fb}^{-1}$ sample [59]. I worked on this analysis too, but more as a consultant than as one of the principal analysts. The result is: $\Delta A_{CP} = (-0.10 \pm 0.08 \pm 0.03)\%$, fully consistent with zero.

2.7 Other analyses of interest

I omit results from other charm CPV and mixing analyses I have worked on in the interest of brevity, but discerning readers may be interested in the following:

- A measurement of the prompt charm production cross-section at LHCb at $\sqrt{s} = 7$ TeV (Ref. [39],

in collaboration with several institutions)

- A measurement of the $D^{\pm}$ production asymmetry at LHCb (Ref. [60], in collaboration with a student at Oxford)
- A search for *CP* violation in $D^+ \to \phi\pi^+$ and $D_s^+ \to K_S^0\pi^+$ (Ref. [45], in collaboration with a student at Oxford)
- A measurement of the charm mixing parameters in $D^0 \to K_S^0\pi^+\pi^-$ using a novel, model-independent method (Ref. [61], in collaboration with Cambridge, Warwick, and a student at Oxford)

2.8 Summary and outlook

At the time of writing, LHCb had taken $3\,\text{fb}^{-1}$ of data at 7–8 TeV and had begin taking data at 13 TeV. The charm cross-section, already large in the 2011–2012 data, has increased by a factor of roughly 2 after moving to 13 TeV [62]. On top of this, improvements in the software trigger architecture will permit a higher efficiency for charm data (or, at least, for a target list of high-sensitivity modes).

With the Run 1 data, LHCb has made precise measurements of many key charm observables, notably mixing [26, 63, 61], indirect *CP* violation [26, 31, 63, 64], and studies of direct CPV in two-body decays [54, 65, 66, 60] and multi-body decays [67, 68, 69, 70]. For direct *CP* violation, the uncertainties are already reaching the per-mille level in some modes, and others will surely follow. This is both very exciting—these are world-leading measurements, driving into regions of parameter space never before probed where new physics may be lurking—and, at the same time, a little disappointing: we have already swept out much of the parameter space where a direct CPV discovery would indicate new physics. Attention in searches for direct CPV will need to turn to modes where the SM contribution is small, such as doubly-Cabbibo-suppressed decays or $\Delta I = 3/2$ transitions—though these will be more tricky experimentally. The situation is rosier for indirect CPV searches, where, despite again having made major gains in sensitivity, we are still some distance from the SM.

Chapter 3

Heavy baryon spectroscopy

In this chapter I will present results from recent analyses of heavy baryon spectroscopy that I carried out at LHCb. First, I will give a brief overview of what is expected for low-lying heavy baryon states. I will then describe a search for Ξ_b^- resonances decaying strongly to the final state $\Xi_b^0\pi^-$ in Sec. 3.2 and a search for the doubly heavy baryon Ξ_{cc}^+ decaying weakly to the final state $\Lambda_c^+K^-\pi^+$ in Sec. 3.3.

3.1 Introduction

This section is heavily based on the text I wrote for the "Charmed baryon spectroscopy and decays" section of the The Physics of the B Factories book [13].

3.1.1 Overview

The spectroscopy of heavy baryons is beautiful and intricate. With three quarks there are numerous degrees of freedom, giving rise to many more states than in the meson sector. At the same time, the large difference in mass between the heavy quark and the light quarks provides a natural way to classify and understand these states: Heavy Quark Effective Theory (HQET) [71, 72, 73]. For pedagocial purposes we will focus in this section on charmed baryons, which are more thoroughly explored experimentally than beauty baryons. The spectrum of known singly charmed states can be thought of in three broad regimes: the ground states, which are a vindication of the constituent quark model; the low-lying excited states, which are described well by HQET; and higher excited states, where the situation is murkier.

The naming convention for charmed and beauty baryons is to take a light baryon, replace one or more s quarks with c (or b) quarks, and add a c (or b) subscript for every quark replaced. Isospin is unchanged. For example, Λ denotes an sud baryon with isospin zero and so Λ_c^+ denotes a cud baryon with isospin zero. Likewise, Ξ_c^0 denotes a csd baryon and Ξ_{cc}^+ denotes a ccd baryon. A summary of charmed baryon states is given in Table 3.1. Following this convention, the experimentally known $C = 1$ baryon states[1] are summarized in Fig. 3.1. Spin-parity assignments follow the PDG [14]; note that in many cases these are assigned based on quark model expectations rather than measurements.

3.1.2 Quark model for ground states

In the constituent quark model [74, 75, 76], baryons composed of u, d, s, c quarks can be classified into $SU(4)$ multiplets according to the symmetry of their flavour, spin, and spatial wavefunctions. All states in a given $SU(4)$ multiplet have the same angular momentum J, and parity P, but can have different quark flavours. For excited states with multiple units of orbital angular momentum the number of possible multiplets becomes large, but for the ground states the picture is much simpler.

[1] Strongly-decaying states are distinguished by their mass following the PDG convention, e.g. $\Xi_c(2645)$. The Ξ_c' and Ω_c^* do not decay strongly and are therefore not labelled by their mass, although the latter is sometimes referred to as the $\Omega_c(2770)$ in the literature.

Table 3.1: Baryon flavour states, isospin, and quark content. The symbol q denotes a u or d quark. Baryons with beauty are not included for brevity, but follow a similar pattern.

Symbol	I	Content
N (p,n)	1/2	udq
Δ	3/2	qqq
Λ	0	sud
Σ	1	sqq
Ξ	1/2	ssq
Ω	0	sss
Λ_c	0	cud
Σ_c	1	cqq
Ξ_c	1/2	csq
Ω_c	0	css
Ξ_{cc}	1/2	ccq
Ω_{cc}	0	ccs
Ω_{ccc}	0	ccc

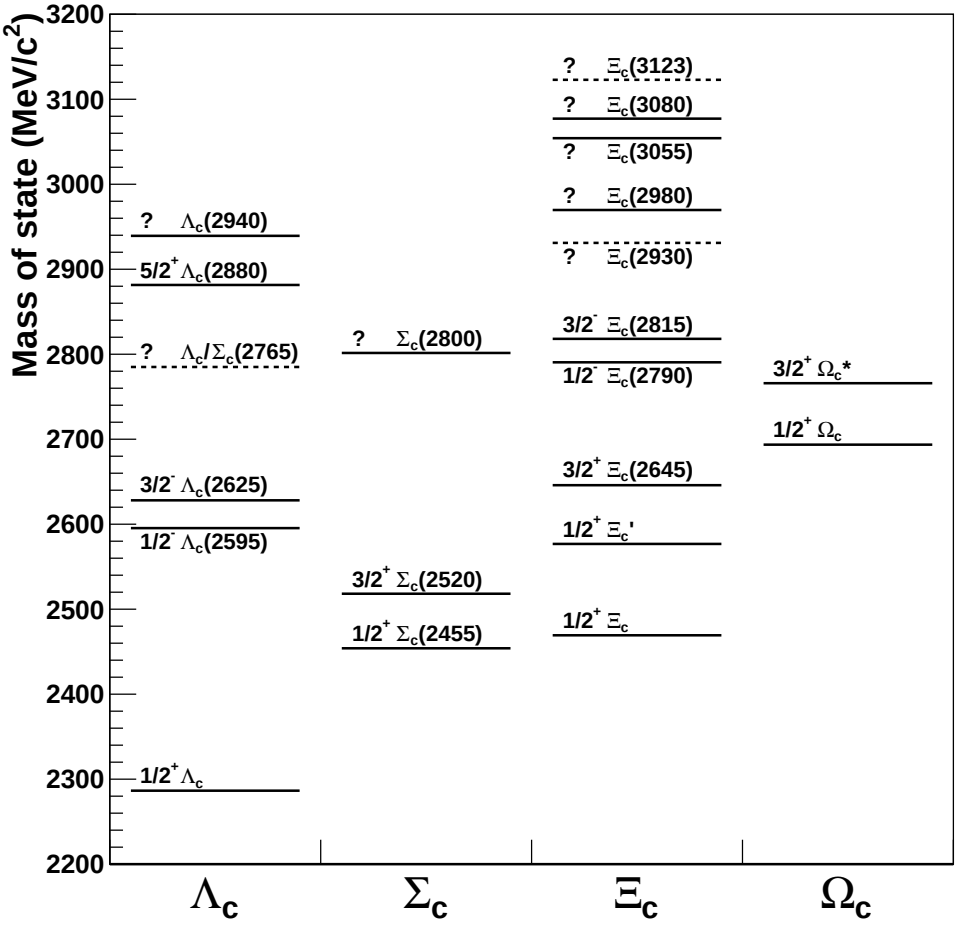

Figure 3.1: Summary of the known charmed baryon states. The spin-parity J^P is given, or marked "?" if not known. States whose existence is unclear (one-star rating in PDG) are marked with a dashed line.

Table 3.2: Summary of the ground state singly charmed baryons. S denotes a wavefunction that is fully symmetric under interchange of any two quarks; M_S and M_A denote mixed overall symmetry with interchange of the two light quarks being symmetric or antisymmetric, respectively; and A would denote a fully antisymmetric wavefunction.

Baryon	Diquark	Diquark I	Diquark j^p	Baryon flavour sym.	Baryon spin sym.	Baryon J^P
Λ_c	qq	0	0^+	M_A	M_A	$1/2^+$
Σ_c	qq	1	1^+	M_S	M_S	$1/2^+$
Σ_c^*	qq	1	1^+	S	S	$3/2^+$
Ξ_c	sq	1/2	0^+	M_A	M_A	$1/2^+$
Ξ_c'	sq	1/2	1^+	M_S	M_S	$1/2^+$
Ξ_c^*	sq	1/2	1^+	S	S	$3/2^+$
Ω_c	ss	0	1^+	M_S	M_S	$1/2^+$
Ω_c^*	ss	0	1^+	S	S	$3/2^+$

This framework is not exact—different states with the same conserved quantum numbers will mix, and baryons are not pure three-quark objects—but it works remarkably well for the ground states.

Quarks are fermions, so the baryon wavefunction must be overall antisymmetric under quark interchange[2]. Baryons are color singlets, and so have an antisymmetric color wavefunction. In the ground state, the orbital angular momentum L is zero (S-wave) and the spatial wavefunction is symmetric. Therefore, the product of the spin and flavour wavefunctions must also be symmetric for ground-state baryons. There are two ways this can be accomplished: both wavefunctions can be fully symmetric, or both can have mixed symmetry with the product being symmetric.

In concrete terms, we can consider a singly charmed baryon to consist of a heavy c quark and a light diquark with spin-parity j^p. Assuming isospin symmetry and letting q denote a u or d quark, there are four possibilities for the flavour content of the diquark:

- qq with isospin 0 (flavour antisymmetric);
- qq with isospin 1 (flavour symmetric);
- sq with isospin 1/2 (either);
- ss with isospin 0 (flavour symmetric).

These correspond to the Λ_c, Σ_c, Ξ_c, and Ω_c states, respectively. The diquark wavefunction must be antisymmetric under quark interchange. Its color wavefunction is antisymmetric and in the ground state its spatial wavefunction is symmetric, so it may be either flavour-symmetric and spin-symmetric ($j^p = 1^+$) or flavour-antisymmetric and spin-antisymmetric ($j^p = 0^+$). Combining the diquark with the charm quark gives rise to the possible states set out in Table 3.2 and illustrated in Fig. 3.2. Those with $J^P = 1/2^+$ are all members of the same multiplet as the proton, and those with $J^P = 3/2^+$ are all members of the same multiplet as the Δ and Ω (Fig. 3.3). Note that there is a second isospin doublet of Ξ_c states with $J^P = 1/2^+$, denoted Ξ_c'.

The constituent quark model predicts relations between the masses of these states as well as their existence and quantum numbers. These were expressed for the light baryons as sum rules (see Ref. [77,

[2] Strictly, it only needs to be antisymmetric under interchange of equal-mass quarks, but in order to build the model we assume $SU(4)$ is a good symmetry.

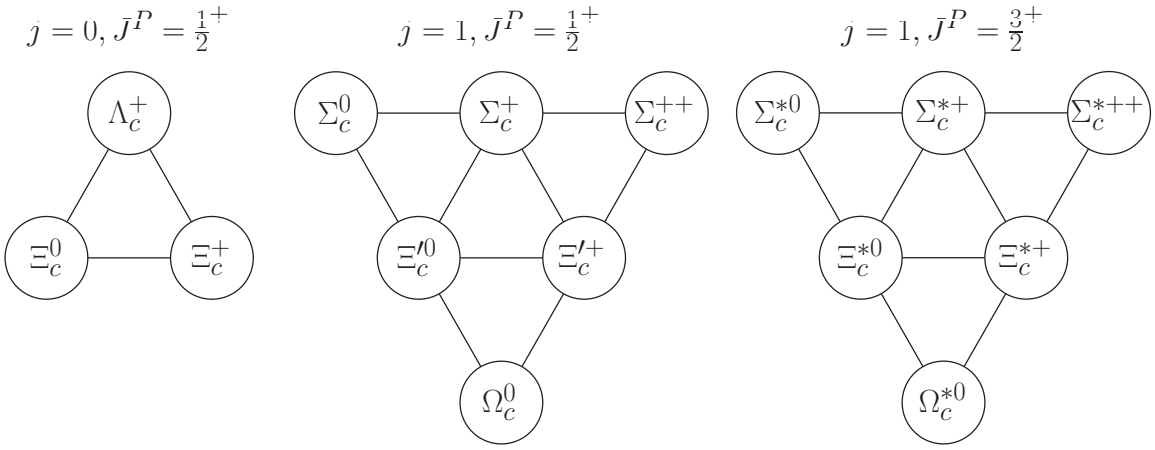

Figure 3.2: The $SU(3)$ multiplets containing the ground state baryons, grouped according to the spin j of the light diquark and the spin-parity J^P of the baryon.

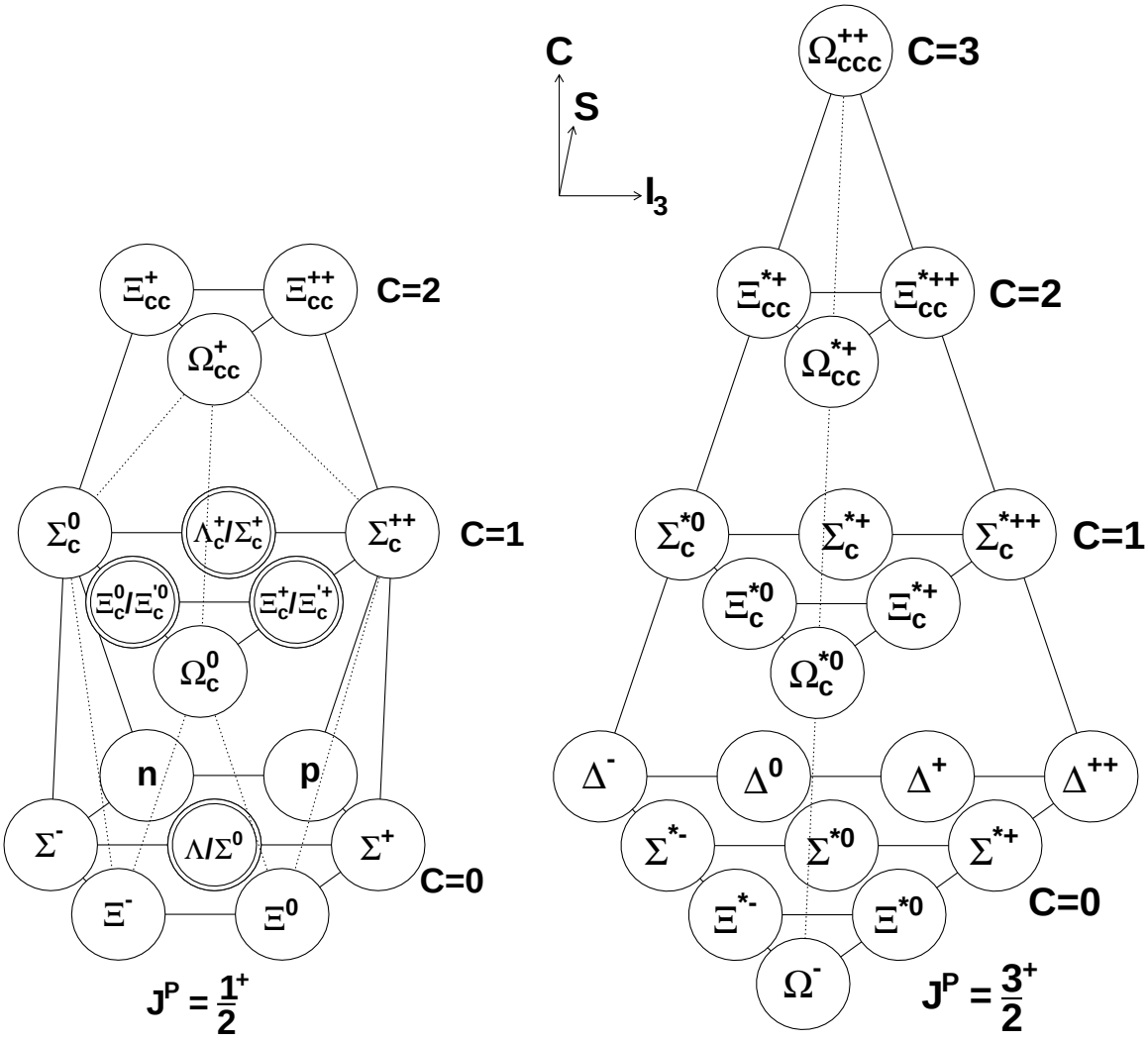

Figure 3.3: The $SU(4)$ multiplets containing the ground state baryons, arranged by spin-parity (J^P), isospin projection (I_3), strangeness (S), and charm (C). A double ring indicates that two states have the same J^P, I_3, S, and C quantum numbers.

78]):

$$(m_N + m_\Xi)/2 = (3m_\Lambda + m_\Sigma)/4, \tag{3.1}$$

$$m_{\Sigma^*} - m_\Delta = m_{\Xi^*} - m_{\Sigma^*} = m_\Omega - m_{\Xi^*}, \tag{3.2}$$

$$m_{\Sigma^*} - m_\Sigma = m_{\Xi^*} - m_\Xi, \tag{3.3}$$

of which the first is the famous Gell-Mann-Okubo rule. These can be thought of as expressing the mass as the sum of the valence quark masses plus a hyperfine (spin-spin) coupling. This can be parameterized in various ways[3], such as [80]:

$$M = A + B' \sum_i \Delta m_i + C' \sum_{i>j} \mathbf{s}_i \cdot \mathbf{s}_j \left(m_q - \Delta m_i - \Delta m_j\right), \tag{3.4}$$

where A, B', and C' are constants, m_q is the mass of a light quark, $\Delta m_i = m_i - m_q$ is the mass difference of the i^{th} quark compared to m_q, and $\mathbf{s}_i$ is the spin of the i^{th} quark. When evaluated for the ground state baryons, the sum rules given in Eq. 3.1–3.3 are recovered. This simple model can also be extended to baryons with heavy quarks. To illustrate its effectiveness, we note that the spectrum and decay pattern of singly charmed baryon ground states was mapped out in an essentially correct way within about three months of the discovery of charm but it took three decades before all of the states were seen experimentally. The last to be discovered was the Ω_c^*. The equal-spacing mass rule still holds for the singly charmed $J = 3/2^+$ multiplet:

$$m_{\Omega_c^*} - m_{\Xi_c^*} = m_{\Xi_c^*} - m_{\Sigma_c^*}, \tag{3.5}$$

but with additional flavours the hyperfine terms become more complicated so the analog of Eq. 3.3 is:

$$m_{\Omega_c^*} - m_{\Omega_c} = 2\left(m_{\Xi_c^*} - m_{\Xi_c'}\right) - \left(m_{\Sigma_c^*} - m_{\Sigma_c}\right). \tag{3.6}$$

Substituting in the current world-average experimental masses for states other than the Ω_c^*, one would calculate $m_{\Omega_c^*}$ to be approximately 2774 MeV/c^2 from Eq. 3.5 or 2770 MeV/c^2 from Eq. 3.6. These simple estimates are in remarkably good agreement with the observed mass, $2765.9 \pm 2.0\,\text{MeV}/c^2$ [14].

3.1.3 Higher states

Baryons can be given orbital (l) or radial (k) excitations. Since they are three-body systems there are two degrees of freedom in each case (denoted ρ, λ). For baryons with one heavy quark (mass M) and two light quarks (mass m), a natural way to specify these is to divide the system into a light diquark and the heavy quark. Taking a simple potential model based on the harmonic oscillator, the energy levels are given by [81]:

$$E = \sqrt{\frac{K}{m}}\left(3 + 2l_\rho + 4k_\rho\right) + \sqrt{\frac{K}{\mu}}\left(3 + 2l_\lambda + 4k_\lambda\right), \tag{3.7}$$

where K is a constant describing the potential and $\mu = (2/3M + 1/3m)^{-1} \approx 3m$ in the heavy quark limit. Thus, the ρ excitations (within the diquark) require roughly $\sqrt{3}$ times as much energy as the corresponding λ excitations (between quark and diquark). Therefore the lowest-lying excitations are those with $l_\lambda = 1$ and the other quantum numbers zero, i.e. $L = 1$. (Within this band there will be further splitting, e.g. due to spin-spin and spin-orbit couplings.) The second band will consist of two groups of states that have comparable energy: those with $l_\lambda = 2$ ($L = 2$) and those with $k_\lambda = 1$ ($L = 0$), with the other quantum numbers being zero. Beyond the second band the degeneracy grows further, but we lack useful experimental data in this region in any case.

[3] See also [79] for a nice review with a different hyperfine interaction term.

We can take this quark-diquark separation one step further for singly heavy baryons by considering the heavy quark to be essentially a spectator and treating the diquark as a distinct object with its own conserved quantum numbers j^p that is the main actor in decays (HQET: see Ref. [73]). As a consequence, some transitions that would otherwise be allowed are now forbidden. To take a concrete example[4], when the decay $\Lambda_c^+(2880) \to \Sigma_c(2455)\pi$ was first observed [82], the analysts wished to see if it was consistent with the state $(J^P, j^p) = (1/2^-, 0^-)$. If we consider only the overall J^P, an S-wave ($L = 0$) strong decay of the heavier state to the lighter state plus a pion, $(1/2^- \to 1/2^+\, 0^-)$, would be allowed. However, conservation of angular momentum forbids the corresponding S-wave diquark transition $(0^- \to 1^+\, 0^-)$. The interpretation that the state is purely $(1/2^-, 0^-)$ is therefore disfavoured (though it could have been an admixture of that state and some other). The HQET constraints thus have a concrete effect on the decay pattern of excited states, and imply that some will be narrow.

All this said, it is important to bear in mind that states which share all conserved, external quantum numbers (J, P, I, C, S) can mix. Therefore we should be careful when interpreting observed resonances as specific expected states, particularly for higher excitations.

3.2 Search for Ξ_b^- resonances

This section summarises the analysis published in [84].

3.2.1 Introduction

As explained in Sec. 3.1.2, baryons form multiplets according to the symmetry of their flavour, spin, and spatial wavefunctions. The pattern of the ground states—that is, those that are neither orbitally nor radially excited—is straightforward to understand and was set out for charm in Sec. 3.1.2. The equivalent b-baryon states should follow a pattern that is broadly similar, but differs in detail (since the splittings depend upon the heavy quark mass). As of 2014, several of the ground states had been discovered including all of the weakly decaying states (Λ_b^0, Ξ_b^-, Ξ_b^0, Ω_b^-) and the charged Σ_b states. In addition, CMS had observed a peak in the $\Xi_b^-\pi^+$ mass spectrum, interpreted as the $J^P = 3/2^+$ Ξ_b^0 state [85]. No studies with comparable sensitivity had been done for the $\Xi_b^0\pi^-$ spectrum. In short, this was one of the relatively rare textbook examples where the existence and properties of previously undiscovered states could be foreseen and tested[5].

In the charm system, the $J^P = 3/2^+$ Ξ_c^* states decay strongly to $\Xi_c\pi$, but the $J^P = 1/2^+$ Ξ_c' are below threshold for strong decay, with $m(\Xi_c'^+) - m(\Xi_c^+) = 108 \pm 3\,\mathrm{MeV}/c^2$ and $m(\Xi_c'^0) - m(\Xi_c^0) = 107 \pm 3\,\mathrm{MeV}/c^2$ [14]. Instead, they decay electromagnetically via $\Xi_c' \to \Xi_c\gamma$. If the analogous Ξ_b' states also decay electromagnetically, they will be hard to observe at LHCb: we would need to find and measure a soft photon from the primary vertex, for which the background would be vast. By contrast, strong decays to final states above but close to the $\Xi_b\pi^\pm$ threshold would be easy to observe (similar to the $D^{*+} \to D^0\pi^+$ decay used in Sec. 2.6). It was not clear *a priori* whether the $\Xi_b'^-$ state would be above or below threshold: there were a variety of theory predictions, some above threshold, some below threshold, and others essentially at threshold [81, 86, 87, 88, 89, 90, 91, 92, 93, 94, 95, 96]. Further, nearly all of the predictions were for the average mass of the isospin doublet which, as we will see shortly, is not the whole story.

We do have two key pieces of experimental input. The first is the mass of the state seen by CMS, which we will assume to be the Ξ_b^{*0}. They reported that

$$m(\Xi_b^{*0}) - m(\Xi_b^-) - m(\pi^+) = 14.84 \pm 0.74 \pm 0.28\,\mathrm{MeV}/c^2. \tag{3.8}$$

[4] This example is based on the discussion of the decay $\Lambda_c^+(2880) \to \Sigma_c(2455)\pi$ in Ref. [82]. The J^P of the state were subsequently measured by Belle to be $5/2^+$ [83].

[5] Full disclosure: Before looking at the data, I guessed incorrectly that the $\Xi_b'^-$ would be below threshold and that only one resonance, the Ξ_b^{*-}, would be seen in the $\Xi_b^0\pi^-$ spectrum. But hindsight makes for better textbooks.

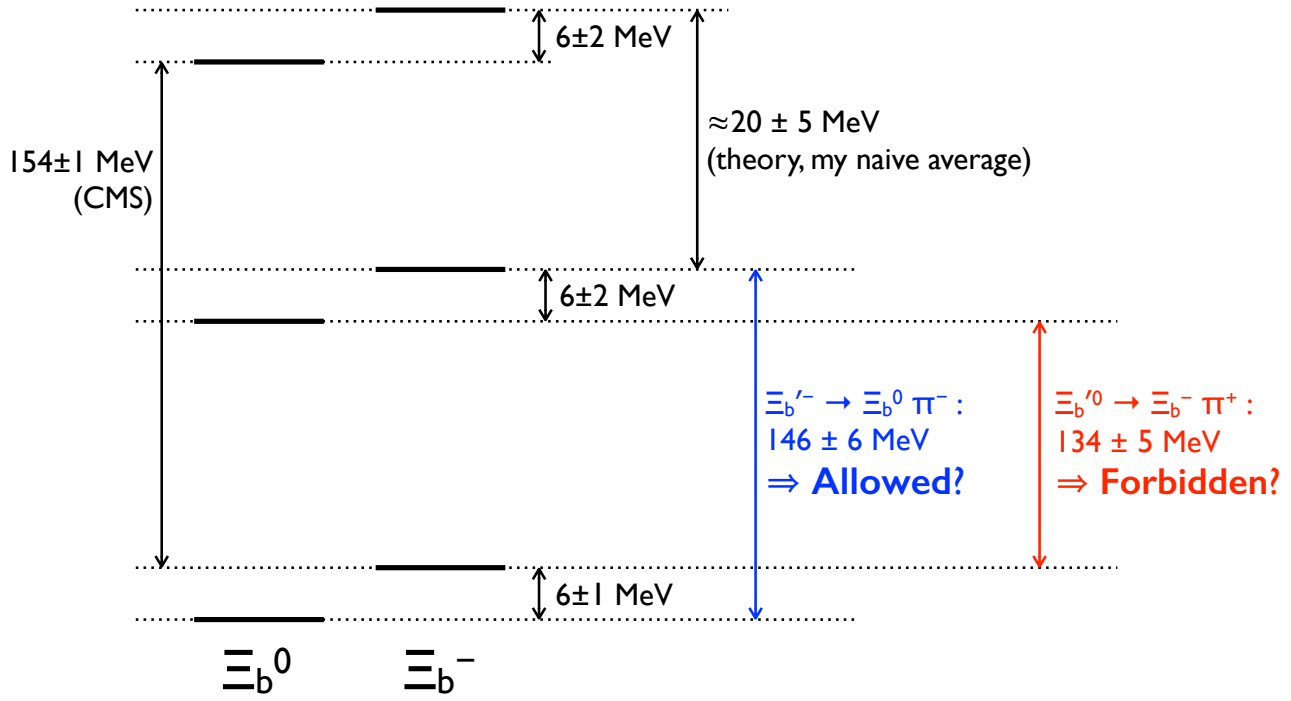

Figure 3.4: Expected spectrum of the low-lying Ξ_b states, under the assumptions outlined in the text. The mass differences are not to scale.

The second is the isospin splitting between the Ξ_b^- and Ξ_b^0 weakly decaying ground states, measured recently by LHCb to be [97]

$$m(\Xi_b^-) - m(\Xi_b^0) = 5.92 \pm 0.64\,\text{MeV}/c^2, \tag{3.9}$$

is in good agreement with the predicted value of $6.24 \pm 0.21\,\text{MeV}/c^2$ [86]. We would also like to know the isospin splittings for the Ξ_b' and Ξ_b^* doublets. These should be roughly similar, but because the hyperfine interaction term differs between the three doublets (eq. 3.4), the isospin splittings will also differ and are likely to be a little smaller for the spin-excited states. As an approximation, we will guess that the splitting is $6 \pm 2\,\text{MeV}/c^2$ for Ξ_b' and for Ξ_b^*.

We need one more piece of information: the expected splitting between the Ξ_b^* and Ξ_b' doublets. Theory estimates of this difference are more robust (and more consistent) than the those for the full difference between the spin-excited states and the weakly decaying ground states, typically falling between 10 and $30\,\text{MeV}/c^2$. We will make a naive average, take it to be $20 \pm 5\,\text{MeV}/c^2$. Putting together these numbers we arrive at the pattern of masses shown in Fig. 3.4, in which the $\Xi_b'^- \to \Xi_b^0\pi^-$ decay is a few MeV/c^2 above threshold while the $\Xi_b'^0 \to \Xi_b^-\pi^+$ decay is a few MeV/c^2 below threshold—though in both cases the difference is only about 1σ. In short, it would be quite plausible for the decay $\Xi_b'^- \to \Xi_b^0\pi^-$ to be kinematically allowed and for the decay $\Xi_b'^0 \to \Xi_b^-\pi^+$ to be forbidden (consistent with the lack of such a peak in CMS's paper).

3.2.2 Reconstruction and selection

We reconstruct $(\Xi_b^0\pi^-)$ candidates via the following decay chain: $\Xi_b^0 \to \Xi_c^+\pi^-$, $\Xi_c^+ \to pK^-\pi^+$. As for the D^{*+} decays discussed in Sec. 2.6, the first π^- is produced at the PV together with the Ξ_b^0 and is referred to as the soft pion. These Ξ_b^0 and Ξ_c^+ decay modes had been studied previously at LHCb [98], and the selection used for this search was heavily based on that[6] and other previous analyses, notably

[6] ... with one important difference: as well as a traditional cut-based selection, Ref. [98] used a Boosted Decision Tree multivariate selector to further improve the signal purity. A multivariate selector is not used in this analysis.

those described in Sec. 3.3 (for the baryon selection) and Sec. 2.6 (for the soft pion and related cuts). Candidates were required to pass the trigger, and specifically to pass an inclusive b-hadron selection in the higher-level software trigger. Additional cuts were applied in a centrally run preselection and in a subsequent offline selection. At each stage of the decay chain, the daughter particles were required to form a common vertex with good fit quality, with the top-level $\Xi_b^0\pi^-$ vertex being constrained in the fit to be consistent with an event PV. Cuts on momentum, track quality, and topology/pointing are applied to reduce combinatorial background, and the decay vertices of the Ξ_c^+ and Ξ_b^0 are required to be displaced from all PVs. The soft pion and the Ξ_b^0 are required to come from the same PV. Particle identification requirements are applied to the final state tracks to remove background from misidentified particles. In addition, Ξ_c^+ candidates are vetoed if they are kinematically consistent with being misidentified $D^+ \to K^-K^+\pi^+$, $D_s^+ \to K^-K^+\pi^+$, $D^+ \to K^-\pi^+\pi^+$, or $D^{*+} \to D^0(K^-K^+)\pi^+$ decays[7]. Lastly, we apply invariant mass cuts to the Ξ_c^+ and Ξ_b^0 candidates. The Ξ_c^+ mass is required to lie within $20\,\mathrm{MeV}/c^2$ of its nominal value (about $\pm 3\sigma$), and the Ξ_b^0 is required to fulfil[8]

$$5765 < m_{\mathrm{cand}}(\Xi_b^0) - m_{\mathrm{cand}}(\Xi_c^+) + m_{\Xi_c^+} < 5825\,\mathrm{MeV}/c^2,$$

where m_{cand} and $m_{\Xi_c^+}$ refer to the candidate and world-average masses. This window corresponds to approximately $\pm 2\sigma$. Lastly, we impose a broad requirement on the mass difference, which we define as

$$\delta m \equiv m_{\mathrm{cand}}(\Xi_b^0\pi_{\mathrm{s}}^-) - m_{\mathrm{cand}}(\Xi_b^0) - m_{\pi^-},$$

in analogy to what was done for the D^{*+}. The fit region is $0 < \delta m < 45\,\mathrm{MeV}/c^2$. After the full selection, we find that there are on average 1.15 candidates in this region per event. Similarly to the D^{*+}, such multiple candidates are predominantly due to a single Ξ_b^0 being paired with more than one soft pion.

For those $(\Xi_b^0\pi^-)$ candidates passing the selection (except the Ξ_b^0 mass cut), the Ξ_b^0 mass spectrum is shown in the left-hand plot of Fig. 3.5. The Ξ_b^0 mass peak can be seen clearly. The δm distribution is shown in the right-hand plot of the same figure For the right-sign $\Xi_b^0\pi^-$ data in the Ξ_b^0 mass signal window, two peaks are clearly visible, one just below $4\,\mathrm{MeV}/c^2$ and one around $24\,\mathrm{MeV}/c^2$. Two control samples in which only background is expected are also shown: right-sign data in the Ξ_b^0 mass sidebands, and wrong-sign $\Xi_b^0\pi^+$ data in the Ξ_b^0 mass signal window. Neither of the background samples exhibits any peaking structure.

3.2.3 Fit to the δm spectrum

At this point it is clear that we have two highly significant peaks. We now need to measure their properties and check that they are consistent with what we would expect for resonances. To do this, we need to fit the δm spectrum. Our model will consist of the two peaks plus an empirical background function. In general, the observed shape of a resonance may be described as its natural lineshape convolved with a resolution function.

To model the resolution, we generate and fit large samples of signal MC in which Ξ_b^- resonances are included with δm values of $3.69\,\mathrm{MeV}/c^2$ and $23.69\,\mathrm{MeV}/c^2$, chosen to correspond to the two peaks seen in data. The natural widths Γ are set to negligible values in the simulation so that the reconstructed width is purely due to resolution effects. We parameterise it as the sum of three Gaussian functions with independent means and fit the simulated data. The general scale of the resolution can be seen from the weighted average of the σ of the three Gaussians, and is $0.21\,\mathrm{MeV}/c^2$ for the lower-mass peak and $0.54\,\mathrm{MeV}/c^2$ for the higher-mass peak. In the fits to data described below, the resolution function will be fixed to that obtained from the fits to simulation, and small corrections will be applied

[7] These vetoes would probably be overkill if considering things purely from the point of view of signal significance, but when aiming to establish new states we want to be really sure that we do not have some pathological peaking background.

[8] This construction effectively takes the Ξ_c^+ resolution out of the Ξ_b^0 mass, improving the resolution.

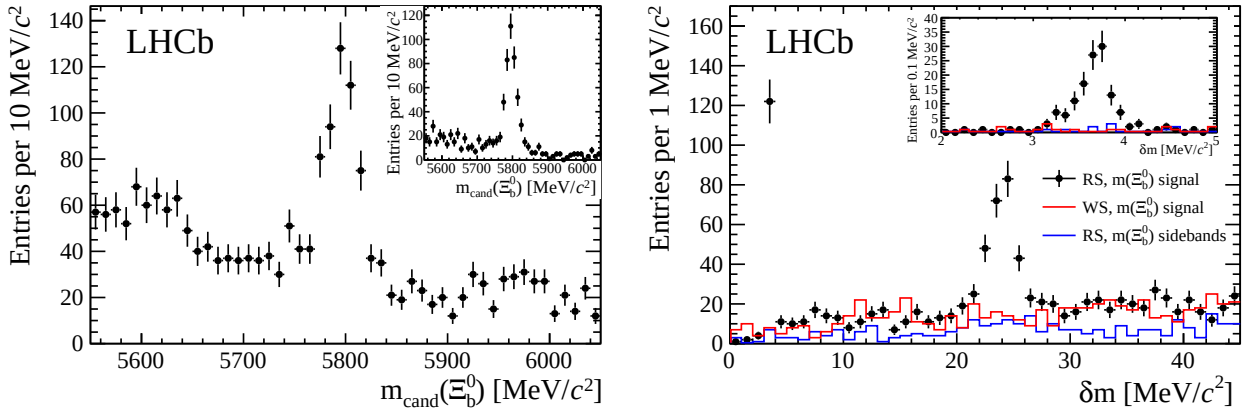

Figure 3.5: Spectra of selected $\Xi_b^0\pi_s^-$ candidates. Left: The distribution of Ξ_b^0 masses for $\Xi_b^0\pi_s^-$ candidates passing the full selection apart from the Ξ_b^0 mass requirement. Left inset: The subset of candidates that lie in the δm signal regions of $3.0 < \delta m < 4.2\,\text{MeV}/c^2$ and $21 < \delta m < 27\,\text{MeV}/c^2$. Right: The δm spectra after the full selection, showing right-sign candidates in the Ξ_b^0 mass signal window (points with error bars), wrong-sign candidates with the same selection (red histogram), and right-sign candidates in the Ξ_b^0 mass sidebands (blue histogram). Right inset: Detail of the region 2.0–5.5 MeV/c^2.

to the masses corresponding to the offsets in the resolution functions seen in the simulation. The combinatorial background will be described by an empirical threshold function of the form

$$f(\delta m) = \left(1 - e^{-\delta m/C}\right)(\delta m)^A,$$

where A and C are freely varying parameters determined in the fit to the data.

We now turn to the natural lineshapes of the peaks. Interpreting the peaks as the $\Xi_b'^-$ and Ξ_b^{*-} states, the transitions would both be P-wave[9]. So in an initial unbinned maximum likelihood fit, each peak is described using a P-wave relativistic Breit-Wigner (RBW) line shape [99] with a Blatt-Weisskopf barrier factor [100], convolved with the resolution function obtained from simulation. The natural width of the lower peak is found to be consistent with zero, *i.e.* the peak is dominated by the resolution, so its natural width is fixed to zero in the nominal fit[10]. We set an upper limit on the width peak using ensembles of toy experiments with the same parameters as in data, but with natural widths ranging from 0.01 to 0.12 MeV. The upper limit is taken to be the value of Γ for which a width equal to or greater than that obtained in data is observed in 95% of the toy experiments. The resulting upper limit is $\Gamma(\Xi_b'^-) < 0.08\,\text{MeV}$ at 95% confidence level (CL).

The nominal fit with the lower width fixed to zero is shown in Fig. 3.6. The fitted yields in the lower- and higher-mass peaks are 121 ± 12 and 237 ± 24 events, with statistical significances in excess of 10σ. With statistical uncertainties only, we measure $\delta m(\Xi_b'^-) = 3.653 \pm 0.018\,\text{MeV}/c^2$, $\delta m(\Xi_b^{*-}) = 23.96 \pm 0.12\,\text{MeV}/c^2$, and $\Gamma(\Xi_b^{*-}) = 1.65 \pm 0.31\,\text{MeV}$. The natural width of the higher-mass peak is inconsistent with zero: the change in likelihood when it is fixed to zero corresponds to a p-value of 4×10^{-14} using Wilks's theorem [101].

[9] The J^P transitions of $\Xi_b'^- \to \Xi_b^0\pi^-$ and $\Xi_b^{*-} \to \Xi_b^0\pi^-$ are $\frac{1}{2}^+ \to \frac{1}{2}^+0^-$ and $\frac{3}{2}^+ \to \frac{1}{2}^+0^-$. The parity changes so we require an odd-numbered orbital angular momentum L. In both cases, the only legal solution is $L = 1$.

[10] We use a numerical method to convolve the natural lineshape and the resolution function. This becomes unstable for very small values of Γ—crudely speaking, when the step size of the convolution is not small compared to Γ—so it is better simply to declare the width to be zero and use only the resolution function to describe the data.

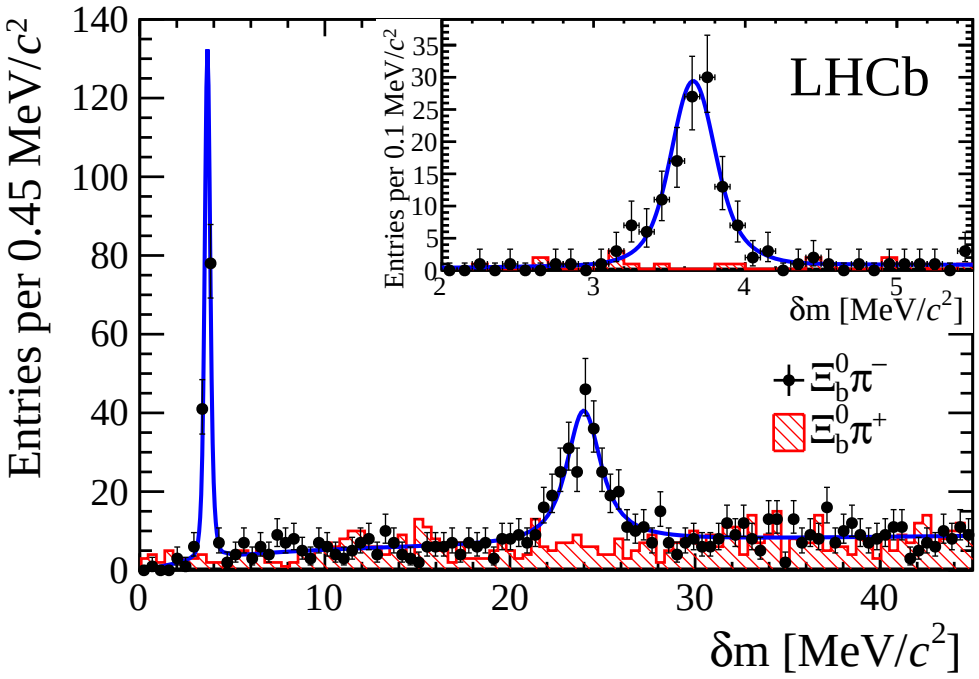

Figure 3.6: Fitted spectra of selected $\Xi_b^0\pi_s^-$ candidates. The points with error bars show right-sign candidates in the Ξ_b^0 mass signal region, and the hatched histogram shows wrong-sign candidates with the same selection. The curve shows the nominal fit to the right-sign candidates. Inset: detail of the region 2.0–5.5 MeV/c^2.

3.2.4 Systematic uncertainties and cross-checks for the δm fit

The measurements of the mass differences and the Ξ_b^{*-} width are the main quantitative results of the analysis, and their statistical uncertainties are small: all sub-MeV. We therefore need to evaluate the systematic uncertainties carefully. Happily, the low background in our channel and the excellent calibration and precision of the LHCb detector make this analysis robust against systematic effects. The uncertainties assigned are summarised in Table 3.3 and described below.

Simulated sample size: The resolution shapes and mass offset corrections are obtained with signal MC. The statistical errors from the fits to the MC samples are assigned as systematic uncertainties.

Multiple candidates: We go back and filter the dataset such that in events where there is more than one candidate in the fit range 0–45 MeV/c^2 after the selection, we choose one at random to retain and reject the rest. Both signals remain highly significant. The changes in the fitted parameters are assigned as systematic uncertainties.

Resolution model: We use signal MC to model the resolution function. However, it might not describe the resolution in data fully. To test this, we inflate the resolution width by a scale factor. When this factor is floated as a free parameter in the fit[11], it is found to be 1.03 ± 0.11, consistent with 1. We repeat the fit with the scale factor fixed to 1.1, based on estimates in previous LHCb analyses and from the D^{*+} control sample (see below), and assign the changes in the fitted parameters as systematic uncertainties.

[11] Remember that we fixed the natural width of the lower peak to be zero, *i.e.* it's a pure resolution function. This is where the main constraint on the scale factor comes from. Since the natural width of the upper peak is floated, we have much less of a constraint from it.

Background description: We try a different background function, specifically a first-order polynomial multiplied by the two-body phase space function. The changes in the fitted parameters are assigned as systematic uncertainties.

Momentum scale: The LHCb reconstruction software includes momentum scale corrections chosen to align the masses of several hadrons with their PDG values. Based on the agreement obtained, the tracking group estimates the systematic uncertainty on the momentum scale to be 3×10^{-4}; we propagate this effect to our mass and width measurements and assign systematic uncertainties accordingly. To check that this is realistic for an analysis like ours working with small mass differences, we validate it on a large sample of $D^{*+} \to D^0(K^-K^+)\pi^+$ decays used previously for the ΔA_{CP} analysis described in Sec. 2.6. We follow the same procedure, including fitting large MC samples to determine the resolution function and mass corrections, to measure the D^{*+} mass difference. We then compare it to a recent BABAR measurement [102, 103] and find a difference of $5.9 \pm 0.34 \pm 0.37 \pm 1.75 \pm 4\,\text{keV}/c^2$, where the errors are our data statistical uncertainty, our MC statistical uncertainty, the BABAR uncertainty, and our estimated mass scale uncertainty, respectively; this means that we are 1.3σ from the BABAR result, implying that our momentum scale uncertainty is sensible.

RBW spin and radial parameter: The signal lineshape model used for the Ξ_b^{*-} required us to assume an angular momentum L, and in addition the barrier factor needs a value for a radius parameter R. In the baseline fit, we took $L = 1$ and $R = 3\,\text{GeV}^{-1}$. We vary these, trying $R = 1\,\text{GeV}^{-1}$, $R = 5\,\text{GeV}^{-1}$, $L = 0$, and $L = 2$. The largest changes in the fitted parameters are assigned as systematic uncertainties. As expected, these have negligible effect on the $\Xi_b^{\prime-}$ since the lineshape model includes only the resolution.

Taking these into account, we obtain

$$\begin{aligned}
\delta m(\Xi_b^{\prime-}) &= 3.653 \pm 0.018 \pm 0.006\,\text{MeV}/c^2, \\
\delta m(\Xi_b^{*-}) &= 23.96 \pm 0.12 \pm 0.06\,\text{MeV}/c^2, \\
\Gamma(\Xi_b^{*-}) &= 1.65 \pm 0.31 \pm 0.10\,\text{MeV}, \\
\Gamma(\Xi_b^{\prime-}) &< 0.08\text{ MeV at 95\% CL.}
\end{aligned}$$

Combining these with the measurement of $m(\Xi_b^0) = 5791.80 \pm 0.50\,\text{MeV}/c^2$ obtained previously at LHCb [98], the masses of these states are found to be

$$\begin{aligned}
m(\Xi_b^{\prime-}) &= 5935.02 \pm 0.02 \pm 0.01 \pm 0.50\,\text{MeV}/c^2, \\
m(\Xi_b^{*-}) &= 5955.33 \pm 0.12 \pm 0.06 \pm 0.50\,\text{MeV}/c^2,
\end{aligned}$$

where the uncertainties are statistical, systematic, and due to the $m(\Xi_b^0)$ measurement, respectively.

Further cross-checks were carried out, including splitting the data by magnet polarity, splitting the data into $\Xi_b^0\pi^-$ and $\overline{\Xi}_b^+\pi^+$ samples, using a symmetric resolution function, imposing a stricter trigger requirement, fitting the wrong-sign control sample, and fixing the natural width of the lower peak to a non-zero value. Consistent behaviour was seen throughout. In addition, other decay modes of the Ξ_b^0 were tested. These do not give such clean, Ξ_b^0 efficient signals (else we would have used them instead!) but we do nonetheless find complementary evidence for the resonances as shown in Table 3.4. The data from $\Xi_b^0 \to \Lambda_c^+ K^-\pi^+\pi^-$, $\Lambda_c^+ \to pK^-\pi^+$, the cleanest of the crosscheck modes, are shown in Fig. 3.7.

3.2.5 Angular analysis

At this point we can be reasonably confident in saying that we have found two new states. Their masses and widths are consistent with what we would expect for the $\Xi_b^{\prime-}$ and Ξ_b^{*-} states, which in the quark model have J^P of $1/2^+$ and $3/2^+$. For both, we reconstruct them through the decay chain:

Table 3.3: Systematic uncertainties, in units of MeV/c^2 (masses) and MeV (width). The statistical uncertainties are also shown for comparison.

Source	$\delta m(\Xi_b')$	$\delta m(\Xi_b^*)$	$\Gamma(\Xi_b^*)$
Simulated sample size	0.002	0.005	
Multiple candidates	0.004	0.048	0.055
Resolution model	0.002	0.003	0.070
Background description	0.001	0.003	0.019
Momentum scale	0.003	0.014	0.003
RBW spin and radial parameter	0.000	0.023	0.028
Sum in quadrature	0.006	0.055	0.095
Statistical uncertainty	0.018	0.119	0.311

Table 3.4: Statistical significances of the signals. For the nominal mode, the masses of the resonances are free parameters in the fit, as is the natural width of the Ξ_b^{*-}. For the other modes, the masses and widths are fixed in the fit.

Ξ_b^0 decay mode	Significance for $\Xi_b^{\prime -}$	Significance for Ξ_b^{*-}
$\Xi_b^0 \to \Xi_c^+\pi^-$, $\Xi_c^+ \to pK^-\pi^+$ (nominal)	$> 10\sigma$	$> 10\sigma$
$\Xi_b^0 \to \Lambda_c^+ K^-\pi^+\pi^-$, $\Lambda_c^+ \to pK^-\pi^+$	6.4σ	4.7σ
$\Xi_b^0 \to D^0 pK^-$, $D^0 \to K^-\pi^+$	4σ	2σ
$\Xi_b^0 \to D^+ pK^-\pi^-$, $D^+ \to K^-\pi^+\pi^+$	3σ	3σ

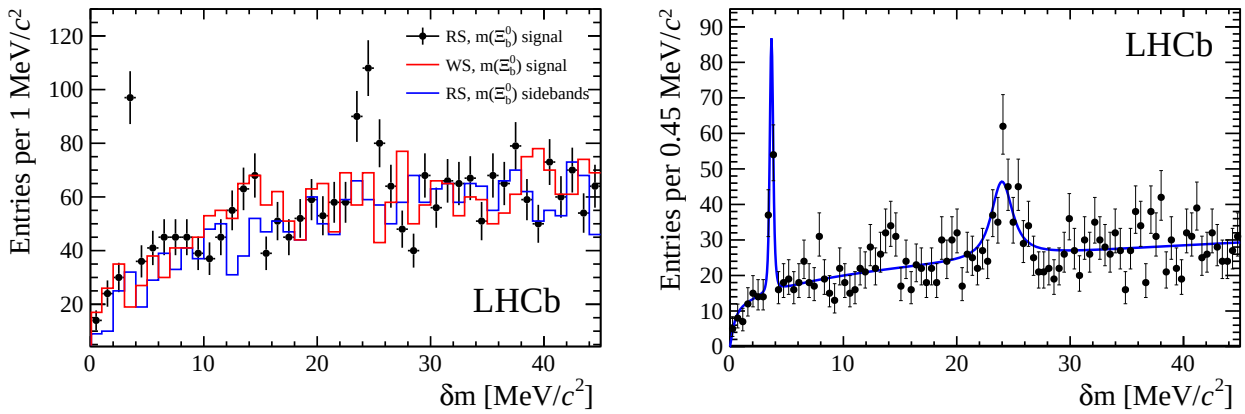

Figure 3.7: The crosscheck mode $\Xi_b^0 \to \Lambda_c^+ K^-\pi^+\pi^-$. The left plot shows the unfitted mass spectrum for right-sign $\Xi_b^0\pi^-$ in the $m(\Xi_b^0)$ signal window (points), wrong-sign $\Xi_b^0\pi^-$ (red histogram), and the right-sign mass sidebands (blue histogram). The right plot shows a fit to the same right-sign data. In the fit, the masses and widths are fixed to the values obtained in the fit to the main $\Xi_b^0 \to \Xi_c^+\pi^-$ sample. The statistical significances are 6.4σ for the lower peak and 4.7σ for the upper peak (from Wilks' theorem).

Table 3.5: Results of the fits to the background-subtracted, efficiency-corrected $\cos\theta_h$ distribution.

Peak	Fitted a	χ^2/NDF for best-fit a	χ^2/NDF for $a = 1$
Lower	0.89 ± 0.11	9.4/7	10.3/8
Upper	0.88 ± 0.11	3.1/7	4.4/8

$\Xi_b^{(\prime,*)-} \to \Xi_b^0\pi^-$, $\Xi_b^0 \to \Xi_c^+\pi^-$. In the quark model, the J^P of both the Ξ_b^0 and the Ξ_c^+ is $1/2^+$. Assuming that this is correct, we can put some constraints on the expected angular distributions[12].

We define the decay helicity angle θ_h as the angle between the 3-momentum of the Ξ_b^0 in the $\Xi_b^{(\prime,*)-}$ rest frame and the 3-momentum of the Ξ_c^+ in the Ξ_b^0 rest frame. This quantity is Lorentz-invariant and can be calculated via

$$\cos\theta_h = \frac{(p\cdot d)\,(q\cdot q) - (p\cdot q)\,(q\cdot d)}{\sqrt{[(p\cdot q)\,(p\cdot q) - (q\cdot q)\,(p\cdot p)]\,[(q\cdot d)\,(q\cdot d) - (q\cdot q)\,(d\cdot d)]}}, \tag{3.10}$$

where p, q, and d are the 4-momenta of the $\Xi_b^{(\prime,*)-}$, the Ξ_b^0, and the Ξ_c^+, respectively. (Since $\cos\theta_h$ is Lorentz-invariant we can evaluate these in any frame, as long as we use the same frame for all three—so we will simply use the lab frame.)

We consider a decay chain $J^P \to \frac{1}{2}^+0^-$, $\frac{1}{2}^+ \to \frac{1}{2}^+0^-$. For $J = \frac{1}{2}$ the distribution the angular distribution is uniform (flat in $\cos\theta_h$). For higher spins the distribution in $\cos\theta_h$ is in general a polynomial of order $(2J-1)$. The coefficients of the polynomial are determined by the elements of the density matrix ρ_{ij}. For the case that the matrix is diagonal, the function will be even (symmetric about $\cos\theta_h = 0$, i.e. only even powers of $\cos\theta_h$ survive). So if we see a polynomial of order $2n$ then we know that $J \geq (n+1)/2$. However, if the $\Xi_b^{(\prime,*)-}$ is unpolarized then the diagonal matrix elements will be equally populated and all of the higher-order terms will cancel, leaving a flat distribution independent of J. So in the quite likely scenario that the state is produced unpolarized or mostly-unpolarized we will not be able to say anything about its quantum numbers—but if we **do** see a non-flat distribution we will be able to exclude lower spins.

For each of the two peaks, we define a narrow window and sideband regions in δm, and from them obtain the background-subtracted, efficiency-corrected $\cos\theta_h$ distribution. This gives us a background-subtracted, efficiency-corrected distribution. We normalize this, setting the sum of all bin contents to one, and fit it with a function of the form

$$f(\cos\theta_h) \propto a + 3(1-a)\cos^2\theta_h \tag{3.11}$$

where the factor of 3 is for normalisation. A value of a differing from 1 would indicate $J > 1/2$. The results of the fits are given in Table 3.5 and plotted in Fig. 3.8. For both states the distribution is consistent with flat. This gives us only weak constraints: it is consistent with the lower peak being a $J = 1/2$ state and the upper peak being an unpolarized or weakly polarized $J = 3/2$ state, but other J are not excluded.

3.2.6 Relative production rates

Finally, we measure the production rates of the two resonances relative to that of the weakly decaying ground state, selected inclusively and passing the same Ξ_b^0 selection criteria as the signal sample. Because of bandwidth restrictions in the centrally run preselection, not all events could be retained for the Ξ_b^0 normalisation mode. Instead, 10% of the candidates were randomly selected and retained

[12] For more background, see Ref. [83] in which Belle applied a similar analysis technique to the decay $\Lambda_c(2880) \to \Sigma_c(2455)\pi$, $\Sigma_c(2455) \to \Lambda_c\pi$; Ref. [104] in which BABAR examined the decay $\Xi_c^0 \to \Omega^-K^+$, $\Omega^- \to \Lambda K^-$; Ref. [105] in which BABAR examined the decay $\Lambda_c^+ \to \Xi(1530)^0K^+$, $\Xi(1530)^0 \to \Xi^-\pi^+$; and Ref. [106] for a guide to the helicity formalism.

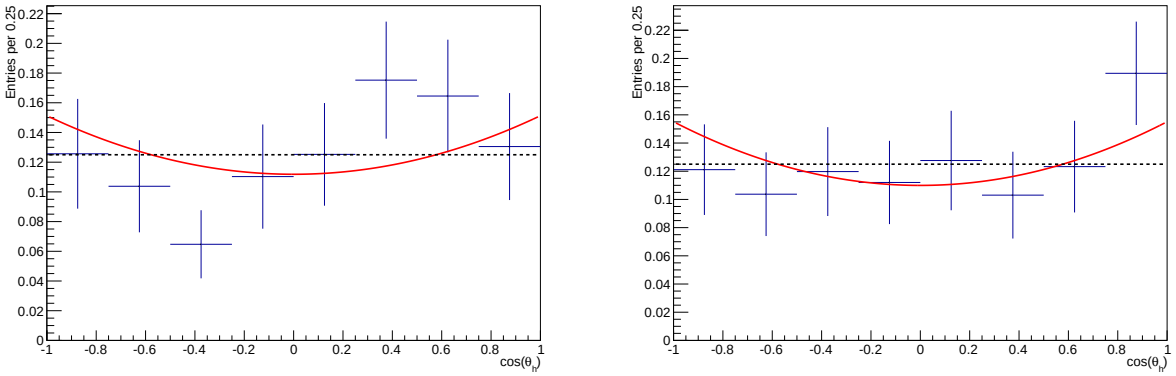

Figure 3.8: Fits to the $\cos\theta_h$ distributions, for (left) $\Xi_b^{\prime -}$ and (right) Ξ_b^{*-}. The dashed black line indicates a flat distribution ($a = 1$ in eq. 3.11). The red curve is a fit in which a quadratic component is allowed.

for use in this analysis. To ensure that the efficiencies are well understood, we use only the subset of events in which one or more of the Ξ_b^0 decay products is consistent with activating the hardware trigger in the calorimeter.

For this subsample of events, the fitted yields are 93 ± 10 for the lower-mass $\Xi_b^0\pi_s^-$ state, 166 ± 20 for the higher-mass $\Xi_b^0\pi_s^-$ state, and 162 ± 15 for the Ξ_b^0 normalization sample. The efficiency ratios are determined with simulated decays, applying the same trigger, reconstruction, and selection procedures that are used for the data. Systematic uncertainties (and, where appropriate, corrections) are assigned for those sources that do not cancel in the efficiency ratios. These uncertainties include the modeling of the Ξ_b momentum spectra, the π_s^- reconstruction efficiency [5], the fit method, and the efficiency of those selection criteria that are applied to the $\Xi_b^0\pi_s^-$ candidates but not to the Ξ_b^0 normalization mode. Combining the 7 TeV and 8 TeV data samples, the results obtained are

$$\begin{aligned}
\frac{\sigma(pp \to \Xi_b^{\prime -} X)\mathcal{B}(\Xi_b^{\prime -} \to \Xi_b^0\pi^-)}{\sigma(pp \to \Xi_b^0 X)} &= 0.118 \pm 0.017 \pm 0.007, \\
\frac{\sigma(pp \to \Xi_b^{*-} X)\mathcal{B}(\Xi_b^{*-} \to \Xi_b^0\pi^-)}{\sigma(pp \to \Xi_b^0 X)} &= 0.207 \pm 0.032 \pm 0.015, \\
\frac{\sigma(pp \to \Xi_b^{*-} X)\mathcal{B}(\Xi_b^{*-} \to \Xi_b^0\pi^-)}{\sigma(pp \to \Xi_b^{\prime -} X)\mathcal{B}(\Xi_b^{\prime -} \to \Xi_b^0\pi^-)} &= 1.74 \pm 0.30 \pm 0.12,
\end{aligned}$$

where the first and second uncertainties are statistical and systematic, respectively, σ denotes a cross-section measured within the LHCb acceptance and extrapolated to the full kinematic range with Pythia, $\mathcal{B}$ represents a branching fraction, and X refers to the rest of the event. Given that isospin partner modes $\Xi_b^{\prime 0} \to \Xi_b^0\pi^0$ and $\Xi_b^{*0} \to \Xi_b^0\pi^0$ are also expected, these results imply that a large fraction of Ξ_b^0 baryons in the forward region are produced in the decays of Ξ_b resonances.

3.2.7 Feed-down mechanism

With a very specific configuration of other excited Ξ_b states, it is possible to produce a narrow peak in the $\Xi_b^0\pi^-$ mass spectrum without invoking a $\Xi_b^{\prime -}$ state. This can occur for the decay chain:

$$\Xi_b^{**-} \to \Xi_b^{\prime 0}\pi^-, \ \Xi_b^{\prime 0} \to \Xi_b^0\pi^0$$

where Ξ_b^{**-} is a higher excitation. If both decays are close to threshold, the particles produced will be kinematically correlated such that combining the Ξ_b^0 daughter with the π^- from the Ξ_b^{**-} would produce a structure in the $m(\Xi_b^0\pi^-)$ spectrum. In general such a structure would be broader than

that seen in the data and would be accompanied by a similar peak in the wrong-sign $\Xi_b^0\pi^+$ spectrum from the isospin-partner decay, $\Xi_b^{**0} \to \Xi_b'^-\pi^+$, $\Xi_b'^- \to \Xi_b^0\pi^-$. However, if a number of conditions are fulfilled[13], it is possible to circumvent these constraints. This would also require that the production rate of the $L = 1$ state be comparable to that of the $L = 0$, $J^P = \frac{3}{2}^+$ state. Although this scenario is contrived, it cannot be excluded at present.

3.2.8 Conclusions

To summarise: two structures are observed with high significance in the $\Xi_b^0\pi^-$ mass spectrum with mass differences above threshold of $\delta m = 3.653 \pm 0.018 \pm 0.006\,\text{MeV}/c^2$ and $23.96 \pm 0.12 \pm 0.06\,\text{MeV}/c^2$. These values are in general agreement with quark model expectations for the $J^P = \frac{1}{2}^+$ $\Xi_b'^-$ and $J^P = \frac{3}{2}^+$ Ξ_b^{*-} states; these very precise measurements, especially that of $m(\Xi_b'^-) - m(\Xi_b^0)$, impose strong constraints on models of heavy baryon spectroscopy. Their natural widths are measured to be $\Gamma(\Xi_b'^-) < 0.08\,\text{MeV}$ at 95% CL and $\Gamma(\Xi_b^{*-}) = 1.65 \pm 0.31 \pm 0.10\,\text{MeV}$. The observed angular distributions in the decays of these states are consistent with the spins expected in the quark model, but other J values are not excluded. The relative production rates are also measured.

3.2.9 Afterword: Ξ_b^{*0}

After this thesis had been written, a follow-on analysis to the above was carried out to investigate the $\Xi_b^-\pi^+$ final state in which CMS had initially observed the Ξ_b^{*0}. The analysis methodology is similar to that described above, except that we use the decay chain $\Xi_b^- \to \Xi_c^0\pi^-$, $\Xi_c^0 \to pK^-K^-\pi^+$. A fit to the data is shown in Fig. 3.9. We confirm the CMS observation, improving the measurement of the mass and making a first measurement of the width:

$$\begin{aligned} m(\Xi_b^{*0}) - m(\Xi_b^-) - m(\pi^+) &= 15.727 \pm 0.068 \pm 0.023\,\text{MeV}/c^2, \\ \Gamma(\Xi_b^{*0}) &= 0.90 \pm 0.16 \pm 0.08\,\text{MeV}. \end{aligned}$$

These results are consistent with, and an order of magnitude more precise than, the CMS values of $\delta m = 14.84 \pm 0.74 \pm 0.28\,\text{MeV}/c^2$ and $\Gamma = 2.1 \pm 1.7\,(\text{stat})\,\text{MeV}$ [85]. Preliminary results from this analysis were presented at Moriond QCD 2016, and a paper will be submitted to JHEP [107].

3.3 Search for Ξ_{cc}^+

This section summarises the analysis published in [108].

3.3.1 Introduction and background

The spectroscopy of ground state baryons was discussed in Sec. 3.1, with a focus on singly heavy states. However, the quark model also predicts doubly (and triply) heavy baryons. In the meson system, charmonium ($c\bar{c}$) and bottomonium ($b\bar{b}$) states have been known for many years, and the B_c^+ meson ($\bar{b}c$) is now well-established. Very recently, the first pentaquark state was observed[14] [109] and has quark content $uudc\bar{c}$, making it the first doubly heavy baryon state seen. However, it still has net charm quantum number zero and will not be discussed further in this document.

The lightest doubly heavy baryons are $\Xi_{cc}^+ = ccd$ and $\Xi_{cc}^{++} = ccu$, which are predicted to form an isospin doublet with $J_P = \frac{1}{2}^+$. Many theoretical model predict the masses and lifetimes of Ξ_{cc}

[13] The details are discussed in Appendix B.1, but in short it would only reproduce the observed spectra if

$$\begin{aligned} m(\Xi_b^{**-}) - m(\Xi_b^0) &= 279.0 \pm 0.5\ \text{MeV}/c^2 \\ m(\Xi_b^{\prime 0}) - m(\Xi_b^0) &= 135.8 \pm 0.5\ \text{MeV}/c^2 \\ m(\Xi_b'^-) - m(\Xi_b^0) &= 138.3 \pm 1.0\ \text{MeV}/c^2. \end{aligned}$$

[14] This was not the first report of a pentaquark observation, but in my opinion it's the first credible one.

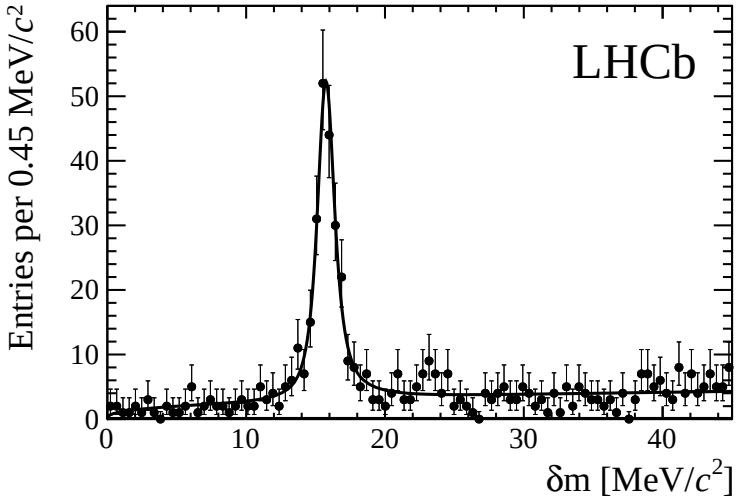

Figure 3.9: Fitted distribution of δm for the final state $\Xi_b^-\pi^+$ from the follow-on analysis 3.9, as described in Sec. 3.2.9.

baryons. Most[15] predict the Ξ_{cc} mass to be in the range of 3.5–3.7 GeV/c^2 [111, 112, 113, 114, 115, 116, 117, 118, 95], and the lifetime to be in the range of 110–250 fs [119, 120, 121].

To date, only one experiment, SELEX, has reported observations of Ξ_{cc} baryons. The data they used were collected by colliding a hyperon beam (containing a mixture of p, Σ^-, and π^-) with a fixed target. They first announced the discovery of the decay $\Xi_{cc}^+ \to \Lambda_c^+ K^-\pi^+$ at a mass of $3518.7 \pm 1.7\,\mathrm{MeV}/c^2$ [122] and subsequently reported a confirmation in the pD^+K^- final state [123][16]. The lifetime was found to be compatible with zero within experimental resolution and less than 33 fs at the 90% confidence level (CL), which is incompatible with the theoretical predictions listed above. SELEX also estimated that 20% of their Λ_c^+ yield originates from Ξ_{cc}^+ decays, in contrast to theory expectations that the production of doubly charmed baryons would be suppressed by several orders of magnitude with respect to singly charmed baryons [114].

Other experiments tried to repeat SELEX's result, but without success. The FOCUS collaboration, a heavy-flavor photoproduction experiment at Fermilab, failed to observe Ξ_{cc}^+ in a sample of 19,400 reconstructed Λ_c^+, compared to the 1650 Λ_c^+ used at SELEX [124]. The e^+e^- b-factories, Belle and BaBar, also reported null results in searches for doubly charmed baryons with large data samples [125, 126]. Still, the production environments at these experiments differed from SELEX's, and it cannot be excluded that the cross-section was greatly enhanced at SELEX compared to the others. While not identical due to the absence of net strangeness in the inital state, LHCb's production environment—hadron-hadron collisions in the forward region—is comparatively close to that of SELEX. If there is such an enhancement, we might see it.

More broadly, double charm production has been observed previously at LHCb both in the $J/\psi\,J/\psi$ final state [127] and in final states including one or two open charm hadrons [128]. The Ξ_{cc} production cross-section is of course unknown, but phenomenological estimates exist for pp collisions at $\sqrt{s} = 14\,\mathrm{TeV}$ and are in the range 60–1800 nb [114, 129, 130]; the cross-section at $\sqrt{s} = 7\,\mathrm{TeV}$ is expected to be roughly a factor of two smaller. As is typical for charmed hadrons, the production is expected to be concentrated in the low transverse momentum and forward rapidity kinematic region that LHCb instruments [130]. For comparison, the prompt Λ_c^+ cross-section in the range $0 < p_\mathrm{T} < 8000\,\mathrm{MeV}/c$ and $2.0 < y < 4.5$ at $\sqrt{s} = 7\,\mathrm{TeV}$ has been measured to be $(233 \pm 26 \pm 71 \pm 14)\,\mu\mathrm{b}$ at LHCb [39], where the uncertainties are statistical, systematic, and due to the description of the fragmentation model,

[15] There are also some references which predict the mass to be beyond 4 GeV/c^2 [110].

[16] SELEX also presented evidence for other new Ξ_{cc} states and decay modes at a Fermilab seminar in 2003, but these claims were never published. The slides are available at: `http://www-selex.fnal.gov/documentation/fnal.pdf`

respectively. Taking into account the LHCb acceptance, the cross-section for Ξ_{cc}^+ production at LHCb is predicted to be smaller than that for Λ_c^+ by a factor of order 10^{-4} to 10^{-3}.

3.3.2 Analysis overview

We'll carry out a search for Ξ_{cc}^+ in $0.65\,\text{pb}^{-1}$ of LHCb data using the decay chain $\Xi_{cc}^+ \to \Lambda_c^+ K^-\pi^+$, $\Lambda_c^+ \to pK^-\pi^+$, and will set upper limits[17] on the production cross-section. We'll quote the Ξ_{cc}^+ cross-section relative to that of the Λ_c^+. This reduces systematic uncertainties, and also makes it simpler to compare our limits to previous experimental results[18]. The production ratio R that is measured is defined as

$$R \equiv \frac{\sigma(\Xi_{cc}^+)\,\mathcal{B}(\Xi_{cc}^+ \to \Lambda_c^+ K^-\pi^+)}{\sigma(\Lambda_c^+)} = \frac{N_{\text{sig}}}{N_{\text{norm}}}\frac{\varepsilon_{\text{norm}}}{\varepsilon_{\text{sig}}}, \tag{3.12}$$

where N_{sig} and N_{norm} refer to the measured yields of the signal (Ξ_{cc}^+) and normalisation (Λ_c^+) modes, ε_{sig} and $\varepsilon_{\text{norm}}$ are the corresponding efficiencies, $\mathcal{B}$ indicates a branching fraction, and σ indicates a cross-section. Assuming that $\mathcal{B}(\Xi_{cc}^+ \to \Lambda_c^+ K^-\pi^+) \approx \mathcal{B}(\Lambda_c^+ \to pK^-\pi^+) \approx 5\%$ [14], the expected value of R at LHCb is of order 10^{-5} to 10^{-4}. By contrast, the SELEX observation [122] reported 15.9 Ξ_{cc}^+ signal events in a sample of 1630 Λ_c^+ events with an efficiency ratio of 11%, corresponding to $R = 9\%$. For convenience, the single-event sensitivity α is defined as

$$\alpha \equiv \frac{\varepsilon_{\text{norm}}}{N_{\text{norm}}\,\varepsilon_{\text{sig}}} \tag{3.13}$$

such that $R = \alpha N_{\text{sig}}$. For each candidate the mass difference is computed as

$$\delta m = m_{\text{cand}}(\Lambda_c^+ K^-\pi^+) - m_{\text{cand}}(\Lambda_c^+) - m(K^-) - m(\pi^+), \tag{3.14}$$

in analogy to what was done in previous sections for the D^{*+} and Ξ_b^{*-}.

Since we don't know the Ξ_{cc}^+ mass, a wide signal window of $380 < \delta m < 880\,\text{MeV}/c^2$ is used for the search, corresponding to approximately $3300 < m(\Xi_{cc}^+) < 3800\,\text{MeV}/c^2$. The search was done entirely blinded: all aspects of the analysis procedure were fixed before the data in this signal region were examined. Likewise, we don't know the Ξ_{cc}^+ lifetime, and the efficiency ε_{sig} depends on its lifetime (and mass). We'll therefore quote limits on R as a function of the Ξ_{cc}^+ mass and lifetime.

3.3.3 Reconstruction and selection

The topology of $\Xi_{cc}^+ \to \Lambda_c^+ K^-\pi^+$, $\Lambda_c^+ \to pK^-\pi^+$ is similar to that of the Ξ_b^0 decay used in Sec. 3.2.2, and the reconstruction and selection share several features. In this section, we focus on the features that are specific to the Ξ_{cc}^+ search.

First, we aim to measure or set a limit on the production relative to that of Λ_c^+, and will therefore align the trigger and selection between the signal (Ξ_{cc}^+) and normalisation (Λ_c^+) modes as far as practical. Second, while the Ξ_{cc}^+ is weakly decaying and so has a non-zero lifetime, that lifetime is expected to be much shorter than that of the Ξ_b^0 from Sec. 3.2, and could be very short ($< 100\,\text{fs}$). Although a strong dependence of the efficiency on the lifetime is inevitable due to trigger and preselection requirements, we will try to avoid making things worse. Third, the expected S/B is worse, so we will need to treat the background more carefully. There are three main sources: fully combinatorial background, consisting of combinations of unrelated tracks and generally originating at the PV; mis-reconstructed charm or beauty hadron decays, which typically occur at a displaced vertex; and combinations of a real Λ_c^+ with other tracks to form a fake Ξ_{cc}^+ candidate. The first two classes have a smooth distribution in both $m_{\text{cand}}(\Lambda_c^+)$ and δm; the third peaks in $m_{\text{cand}}(\Lambda_c^+)$ but is smooth in δm.

We first reconstruct $\Lambda_c^+ \to pK^-\pi^+$, applying kinematic, track quality, particle identification, and vertex fit quality requirements. The decay vertex of the Λ_c^+ is required to be significantly displaced

[17] We would have quoted a value if we'd seen it, but we didn't.

[18] The price is that the selection is not statistically optimal for discovery, since we reject some signal candidates whose relative efficiency is difficult to control.

from the PV ($\chi^2 > 36$) and all three daughter tracks are required not to point to any PV in the event. A loose pointing requirement[19] is applied to the Λ_c^+ daughters of Ξ_{cc}^+ candidates, with a stricter cut used for Λ_c^+ in the normalisation mode. One of the Λ_c^+ daughter tracks must activate the calorimeter hardware trigger[20] and the Λ_c^+ candidate must activate a dedicated software trigger. This software trigger was only enabled for part of the 2011 run, hence the use of $0.65\,\text{fb}^{-1}$ rather than the full $1.0\,\text{fb}^{-1}$. A broad mass window of 2185–2385 MeV/c^2 is applied to Λ_c^+ candidates. Other than the pointing requirement mentioned above, the Λ_c^+ selection is identical for the signal and normalisation modes.

The Λ_c^+ candidates are then combined with two tracks to form a $\Xi_{cc}^+ \to \Lambda_c^+ K^- \pi^+$ candidate. Kinematic, track quality, particle identification, and vertex fit quality cuts are applied, along with requirements that the Λ_c^+ vertex be at least 10 µm downstream of the Ξ_{cc}^+ vertex, and that the Ξ_{cc}^+ vertex be displaced from the PV ($\chi^2 > 16$). The latter cut was applied in the centrally run preselection and, in combination with cuts on the pointing of the two Ξ_{cc}^+ daughter tracks, has the unpleasant effect of killing the efficiency of short-lived[21] Ξ_{cc}^+. Those Ξ_{cc}^+ candidates passing the selection are refitted with a constraint requiring them to originate at the PV.

Finally, a multivariate selector, implemented as an artificial neural network (ANN), is used to further suppress background for the Ξ_{cc}^+ channel. Nine input variables are used, eight associated with the geometry of the decay (*e.g.* the flight distance impact parameter χ^2s and the vertex quality) with the ninth being the smallest p_T of the Ξ_{cc}^+ daughters. These variables were chosen both for their ability to separate signal from background and for their relative ease of reproducibility in signal MC[22]. The relative efficiency of the ANN was approximately 56% for signal (assuming a mass of 3500 MeV/c^2 and a lifetime of 333 fs) and 4% for background.

3.3.4 Fit to the Λ_c^+ normalisation mode

We will need the yield of inclusive Λ_c^+. We use a simple 1D fit to the $pK^-\pi^+$ mass spectrum. The signal shape is described as the sum of two Gaussian functions with a common mean, and the background is parameterised as a first-order polynomial. The fit is shown in Fig. 3.10. The selected Λ_c^+ yield in the full $0.65\,\text{fb}^{-1}$ sample is $N_\text{norm} = (818 \pm 7) \times 10^3$, with an invariant mass resolution of around 6 MeV/c^2. This is taken to be fully prompt: the tight pointing requirement rejects Λ_c^+ produced in b-hadron decays.

3.3.5 Ξ_{cc}^+ yield determination method

Next, we need a method to measure the Ξ_{cc}^+ signal yield. We don't know what the mass of the state is[23], so we'll scan across the allowed range ($380 \le \delta m \le 880\,\text{MeV}/c^2$) in steps of 1 MeV/$c^2$, for a total of 501 tests. The step size is chosen to be safely smaller than the experimental resolution (see below), so that there is no risk of accidentally missing a real peak. Clearly the 501 separate measurements will not all be statistically independent; we'll discuss the statistical procedure to handle them in Sec. 3.3.7. For each mass hypothesis we'll compute a background-subtracted yield. For robustness, two different methods, described below, were used to measure the yield.

[19] The Λ_c^+ daughter of a long-lived Ξ_{cc}^+ wouldn't point exactly to PV, but the cut here is loose enough that the loss would be minimal in practice. It corresponds to a cone with an opening angle of $2 \times 11.5°$.

[20] This requirement costs us quite a lot of efficiency. The calorimeter E_T cuts are tight, especially for tracks from multibody charm decays. We could have increased the efficiency by using a broader variety of triggers—but then the efficiency ratio to the normalisation mode would have become much less certain.

[21] It also rejects strongly decaying Ξ_c^+ resonances such as the $\Xi_c^+(2980)$ and $\Xi_c^+(3055)$ which are known to decay to the $\Lambda_c^+ K^- \pi^+$ final state, but which of course don't fly any measureable distance. This is a pity, since they would have made excellent control modes.

[22] Cuts on the hadron ID likelihood ratios, for example, would have been great for separating signal from background in a multivariate selector, but because of MC-data differences it would have been very hard to calculate and validate the efficiency.

[23] We also don't know its lifetime, but that doesn't affect the yield measurement method, just the efficiency.

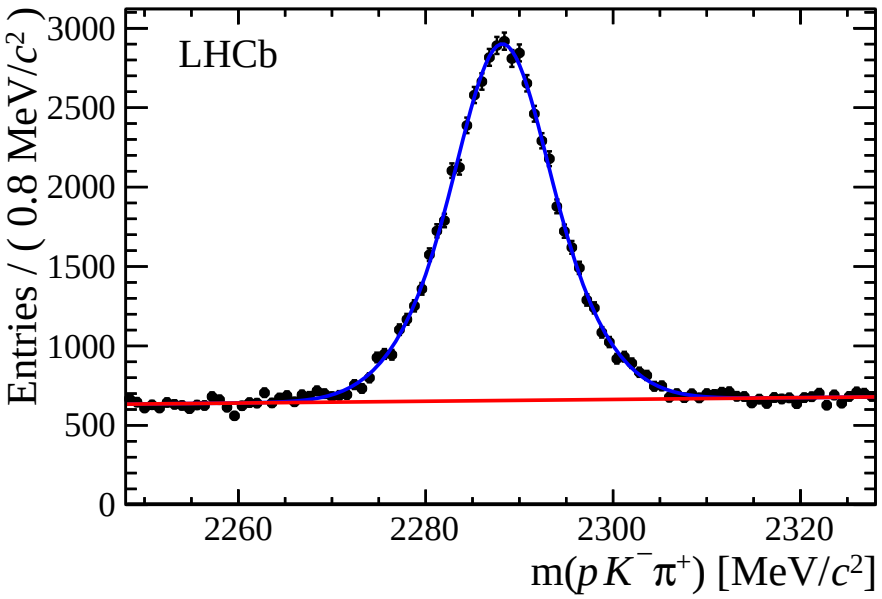

Figure 3.10: Invariant mass spectrum of $\Lambda_c^+ \to pK^-\pi^+$ candidates for 5% of the data, with events chosen at random during preselection (due to bandwidth limits for the normalisation mode). The red line shows the fitted background contribution, and the blue line the sum of Λ_c^+ signal and background.

In Fig. 3.11, we see the δm spectrum of truth-matched Ξ_{cc}^+ candidates in a sample of signal MC events. Fitting the candidates with the sum of two Gaussian functions, the resolution is found to be approximately 4.4 MeV/c^2. While this is probably reasonably close to the right number, we don't want to rely on the MC modelling the lineshape exactly: it will depend on the production kinematics, which are not known *a priori*. We also can't rely on getting the lineshape from data, since the yield is likely to be small or zero. We therefore design our yield measurement methods to be insensitive to the details of the Ξ_{cc}^+ lineshape.

For both methods, we start by defining a narrow signal window in δm and $m_{\rm cand}(\Lambda_c^+)$. We take $2273 < m_{\rm cand}(\Lambda_c^+) < 2303\,{\rm MeV}/c^2$ and $|\delta m - \delta m_0| < 10\,{\rm MeV}/c^2$, where δm_0 is the value of δm under the current Ξ_{cc}^+ mass hypothesis. Let the number of candidates inside that 2D window be N_{S+B}. We then use candidates outside the narrow 2D window to estimate the expected background N_B inside the window. The signal yield is then just $N_S = N_{S+B} - N_B$. In this way we avoid the need to model the signal shape in δm (beyond an efficiency correction for the tails[24] that are lost outside the $\pm 10\,{\rm MeV}/c^2$ window in δm). It also saves us from the various technical heartaches that come from trying to fit a small or zero signal above a small background[25]. Toy MC experiments were used to validate both methods, and to check that they produced unbiased yield estimates.

The first method is an analytic, two-dimensional sideband subtraction in $m_{\rm cand}(\Lambda_c^+)$ and δm. A two-dimensional region of width $80\,{\rm MeV}/c^2$ in $m_{\rm cand}(\Lambda_c^+)$ and width $200\,{\rm MeV}/c^2$ in δm is defined, centred around the narrow signal window. A 5×5 array of non-overlapping bins is defined within this region, with the central bin identical to the narrow signal window (see Fig. 3.12). We then assume that the background consists of two components: a combinatorial component, which is described by a two-dimensional quadratic function, and a Λ_c^+ component, which is described by the product of a signal peak in $m_{\rm cand}(\Lambda_c^+)$ and a quadratic function in δm. Under this assumption, we can fully determine the

[24] The resolution depends on the energy release, i.e. on δm. So the efficiency correction depends on δm. This isn't a big effect, but it does get noticeable towards the upper end of the δm range. In hindsight, we could have made the efficiency vary less with δm by choosing a wider window.

[25] χ^2 fits are useless in this scenario: they give biased yields when the yield per bin is small and the background is estimated from the data. Likelihood fits work after a fashion, but their yields are biased and difficult to interpret: the PDF is not allowed to go negative so when the background is small the signal yield must be bounded below at zero.

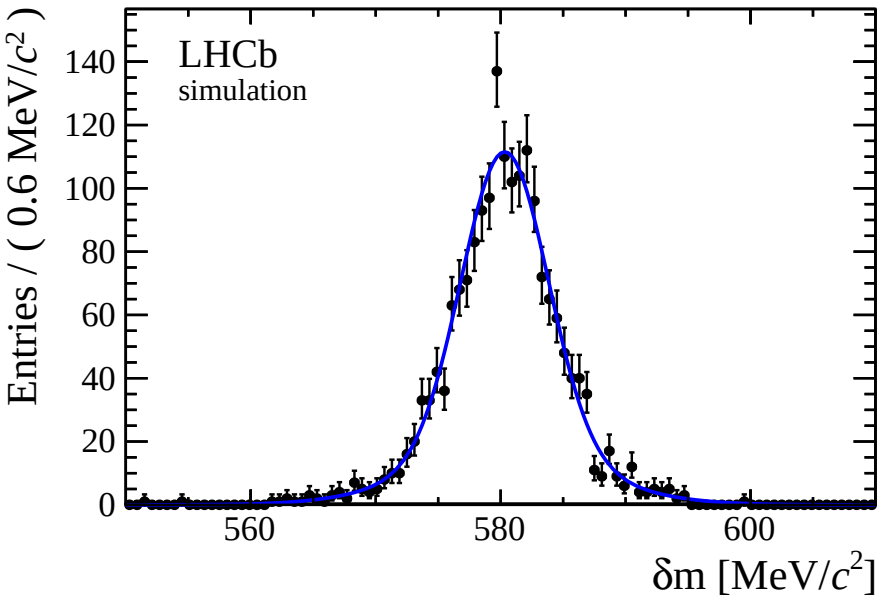

Figure 3.11: The distribution of the invariant mass difference δm, defined in Eq. 3.14, for simulated Ξ_{cc}^+ events with a Ξ_{cc}^+ mass of 3500 MeV/c^2. The solid line shows the fitted signal shape. In order to increase the available statistics, the trigger and ANN requirements are not applied in this plot.

background distribution from the 24 sideband bins, and hence evaluate its integral within the signal box analytically. This gives us both N_B and its statistical uncertainty. This method has the advantage that it requires only minor assumptions about the background distribution, which is a big plus since we can't actually look at the central part of that distribution prior to unblinding (because events that are background for one mass hypothesis may be in the signal box for a different mass hypothesis). Because of this, we adopt it as the baseline approach.

The second method is used as a cross-check. We impose a narrow window on all candidates of $2273 < m_{\rm cand}(\Lambda_c^+) < 2303\,{\rm MeV}/c^2$ to reduce the problem to a one-dimensional distribution in δm. In studies of the $m_{\rm cand}(\Lambda_c^+)$ and δm sidebands, shown in Fig. 3.13, we find that the background can be described by a function of the form

$$f(\delta m) = \begin{cases} L(\delta m;\mu,\sigma_L) & \delta m \leq \mu \\ aL(\delta m;\mu,\sigma_R) & \delta m \geq \mu \end{cases} \tag{3.15}$$

where $L(\delta m;\mu,\sigma)$ is a Landau distribution, a is chosen such that $L(\mu;\mu,\sigma_L) = aL(\mu;\mu,\sigma_R)$, and μ, σ_L, and σ_R are free parameters. So for each hypothesis δm_0, the data will be fitted with this function across the full range, $0 < \delta m < 1500\,{\rm MeV}/c^2$, excluding the signal window of width $20\,{\rm MeV}/c^2$. The fitted function is then integrated across the signal window to give the expected background N_B.

3.3.6 Efficiency calculation and systematic uncertainties

We have a procedure to measure the yields. However, we want to be able to convert them into values (or upper limits) on R, as defined in Eq. 3.12. To do this we'll need the efficiency ratio, $\varepsilon_{\rm norm}/\varepsilon_{\rm sig}$. There are some subtleties in its calculation, but since we will in the end be dominated by statistical effects we'll elide most of those. The efficiencies are factorised into components for the geometric acceptance, the reconstruction and selection, the PID cuts, the ANN selector used for the Ξ_{cc}^+ signal, and the trigger. The efficiencies are estimated from signal MC and corrected for known data-MC differences with control samples of data. Note that generating the signal MC in the first place required us to assume a model for the production (*i.e.* a distribution for Ξ_{cc}^+ in $p_{\rm T}$ and rapidity); the efficiency

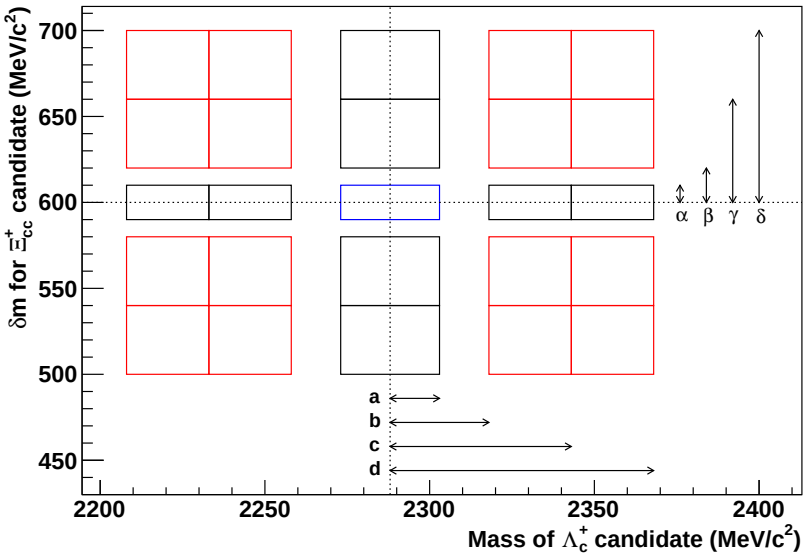

Figure 3.12: The definitions of signal and sideband boxes for the baseline (25 tiles) method, shown for an example mass hypothesis of $\delta m_0 = 600\,\mathrm{MeV}/c^2$. The narrow signal window is the blue, central box. The numerical values can vary—in particular, the central point in δm will be moved in steps.

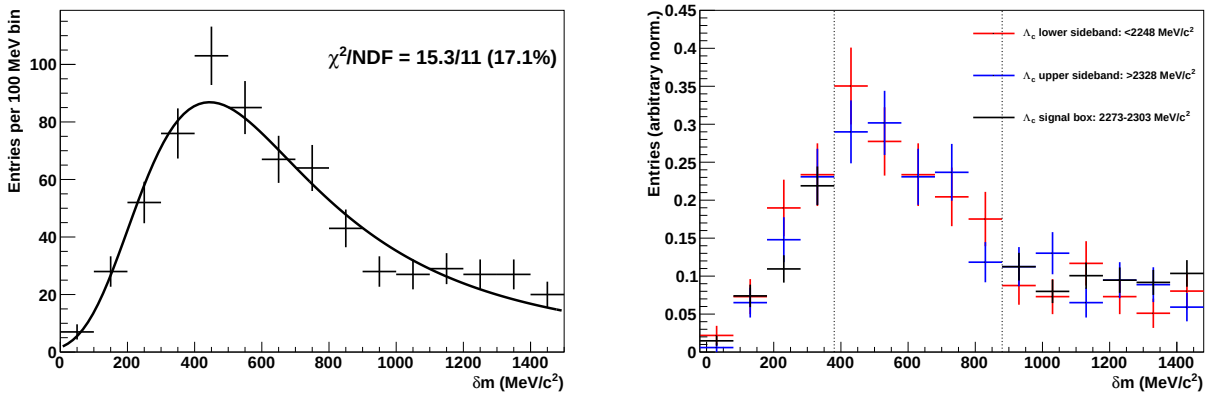

Figure 3.13: Left: Fit of a two-sided Landau distribution to the δm spectrum of data in the $m_{\mathrm{cand}}(\Lambda_c^+)$ sidebands. All events in the region $2248 < m_{\mathrm{cand}}(\Lambda_c^+) < 2328$ MeV/c^2 are excluded. Right: Comparison of the δm spectrum in the $m_{\mathrm{cand}}(\Lambda_c^+)$ sidebands (red, blue) to the spectrum in the $m_{\mathrm{cand}}(\Lambda_c^+)$ signal region (black). The blinded δm signal window is indicated by the dotted vertical lines. The three datasets are normalized to have the same integral outside the blinded region. Note that the x-axis is shifted by 20 MeV/c^2 to align the bin edges with the blinded region.

Table 3.6: Systematic uncertainties on the single-event sensitivity α, evaluated for a Ξ_{cc}^+ mass of 3500 MeV/c^2 and a lifetime of 333 fs.

Source	Size
Simulated sample size	18.0%
IP resolution	13.3%
PID calibration	11.8%
Tracking efficiency	4.7%
Trigger efficiency	3.3%
Total uncertainty	26.0%

Table 3.7: Single-event sensitivity α for different lifetime hypotheses τ, assuming $m(\Xi_{cc}^+) = 3500\,\text{MeV}/c^2$. The uncertainties quoted include statistical and systematic effects, and are correlated between different lifetime hypotheses.

τ	$\alpha\,(\times 10^{-5})$
100 fs	63 ± 31
150 fs	15 ± 5
250 fs	4.1 ± 1.1
333 fs	2.5 ± 0.6
400 fs	1.9 ± 0.5

depends fundamentally on this assumption. The model used is the GENXICC generator [131] and in the absence of a signal in experimental data we simply make an explicit assumption that it is correct.

The efficiency depends on the assumed Ξ_{cc}^+ mass and lifetime. We generate full MC for a working point at 3500 MeV/c^2 and 333 fs, and extrapolate the efficiency to other values by reweighting the kinematic distributions (for the mass) or the decay time distribution (for the lifetime)[26]. At our working point, the efficiency ratio is $\varepsilon_{\text{norm}}/\varepsilon_{\text{sig}} = 20.4$. Together with the normalisation mode yield, this implies that the single-event sensitivity (defined in Eq. 3.13) at our working point is $\alpha = 2.5 \times 10^{-5}$.

We compute systematic uncertainties on the efficiency (although in practice these will turn out to be small compared to the statistical uncertainty in data). They are evaluated at the working point and summarised in Table 3.6. Taking their sum in quadrature, the total systematic uncertainty is 26%. Additional systematic uncertainties associated with candidate multiplicity, yield measurement, and the decay model of $\Xi_{cc}^+ \to \Lambda_c^+ K^- \pi^+$, which may proceed through intermediate resonances, were considered but found to be negligible in comparison with the total systematic uncertainty. The systematic uncertainties are tested for dependence on the lifetime and mass hypotheses of the Ξ_{cc}^+. In most cases they are unaffected, but the uncertainties associated with the MC sample size and the trigger efficiency do depend on the lifetime and we take this variation into account. The values and uncertainties of the single-event sensitivity α are given for several lifetime hypotheses in Table 3.7.

Finally, we can use the values of the single-event sensitivity to calculate the expected yield for various values of the production ratio R. As explained earlier, the value of R at LHCb is not known but is expected to be of the order 10^{-5} to 10^{-4}, while the SELEX observation corresponds to $R = 9\%$. Table 3.8 shows the expected signal yield, calculated according to eq. 3.8, for various values of R and lifetime hypotheses. From studies of the sidebands in $m_{\text{cand}}(\Lambda_c^+)$ and δm, the expected background in the narrow signal window is between 10 and 20 events. Thus, no significant signal excess is expected if the value of R at LHCb is in the range suggested by theory. However, if production is greatly enhanced

[26] It turns out that the overall efficiency is pretty insensitive to the mass. It depends very strongly on the lifetime, of course.

Table 3.8: Expected value of the signal yield N_{sig} for different values of R and lifetime hypotheses, assuming $m(\Xi_{cc}^+) = 3500\,\text{MeV}/c^2$. The uncertainties quoted are due to the systematic uncertainty on α.

τ	$R = 9\%$	$R = 10^{-4}$	$R = 10^{-5}$
100 fs	140 ± 70	0.2 ± 0.1	0.02 ± 0.01
150 fs	600 ± 200	0.7 ± 0.2	0.07 ± 0.02
250 fs	2200 ± 600	2.4 ± 0.7	0.24 ± 0.07
333 fs	3600 ± 900	4.0 ± 1.0	0.40 ± 0.10
400 fs	4800 ± 1200	5.3 ± 1.4	0.53 ± 0.14

for baryon-baryon collisions at high rapidity, as reported at SELEX, a large signal might be visible. The procedure for determining the significance of a signal, or for establishing limits on R, is discussed in the following section.

3.3.7 Significance and upper limit procedures

As explained earlier, we don't know the Ξ_{cc}^+ mass so we test for the presence of a signal at numerous mass hypotheses, between $\delta m = 380\,\text{MeV}/c^2$ and $\delta m = 880\,\text{MeV}/c^2$ inclusive in $1\,\text{MeV}/c^2$ steps, for a total of 501 tests. For a given value of δm, the signal and background yields and their associated statistical uncertainties are estimated. From these, the local significance $\mathcal{S}(\delta m)$ is calculated, where $\mathcal{S}(\delta m)$ is defined as

$$\mathcal{S}(\delta m) \equiv \frac{N_{S+B} - N_B}{\sqrt{\sigma_{S+B}^2 + \sigma_B^2}} \tag{3.16}$$

and σ_{S+B} and σ_B are the estimated statistical uncertainties on the yield in the signal window and on the expected background, respectively. Since we check for a peak at multiple points, we have to take the look elsewhere effect (LEE) [132] into account. The procedure used is to generate a large number of toy experiments containing only background events, with the amount and distribution of background chosen to match the data (as estimated from sidebands). For each toy experiment, the full analysis procedure is applied in the same way as for data, and the local significance is measured at all 501 values of δm. The LEE-corrected p-value for a given $\mathcal{S}$ is then taken to be the fraction of the toy experiments that contain an equal or larger local significance at any point in the δm range.

The procedure we established before unblinding is that if no signal with an LEE-corrected significance of at least 3σ is seen, upper limits on R would be quoted. The CL_s method [133, 134] is applied to determine upper limits on R for a particular δm and lifetime hypothesis, given the observed yield N_{S+B} and expected background N_B in the signal window. The statistical uncertainty on N_B and systematic uncertainties on α are taken into account. The 95% CL upper limit is then evaluated as the value of R for which $CL_s = 0.05$. Upper limits are calculated at each of the 501 δm hypotheses, and for five lifetime hypotheses (100, 150, 250, 333, 400 fs).

3.3.8 Results

The δm spectrum in data is shown in Fig. 3.14, and the estimated signal yield in Fig. 3.15. No clear signal is found with either background subtraction method. In both cases the largest local significance occurs at $\delta m = 513\,\text{MeV}/c^2$, with $\mathcal{S} = 1.5\sigma$ in the baseline method and $\mathcal{S} = 2.2\sigma$ in the cross-check. Applying the LEE correction described above, these correspond to p-values of 99% and 53%, respectively. Since there is no significant excess above background, upper limits are set on R at the 95% CL, shown in Fig. 3.16 for the first method. These limits are tabulated in Table 3.9 for blocks of δm and the five lifetime hypotheses. The blocks are $50\,\text{MeV}/c^2$ wide, and for each block the largest (worst) upper limit seen for a δm point in that block is given. Similarly, the largest upper limit seen

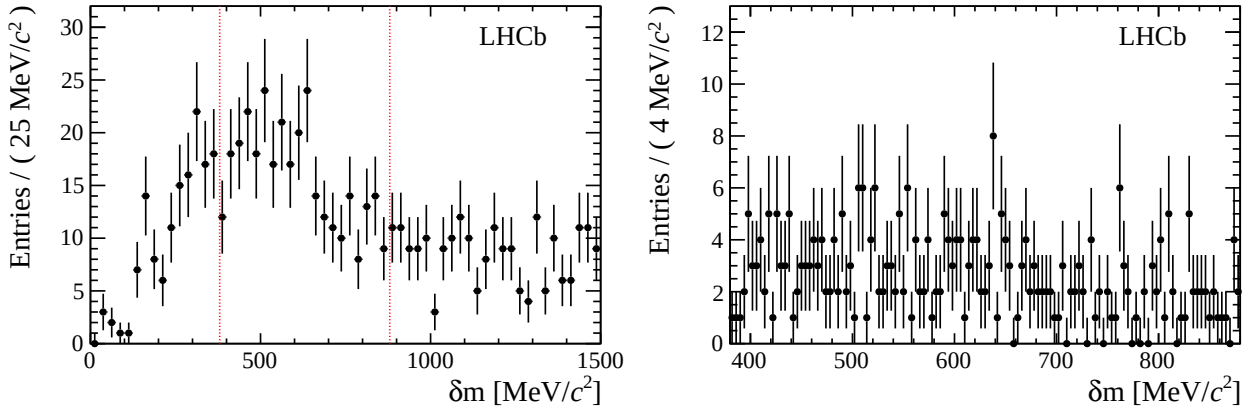

Figure 3.14: Spectrum of δm requiring $2273 < m_{\rm cand}(\Lambda_c^+) < 2303\,{\rm MeV}/c^2$. Both plots show the same data sample, but with different δm ranges and binnings. The wide signal region is shown in the right plot and indicated by the dotted vertical lines in the left plot.

Table 3.9: Largest values of the upper limits (UL) on R at the 95% CL in blocks of δm for a range of lifetime hypotheses, given in units of 10^{-3}. The largest values across the entire $500\,{\rm MeV}/c^2$ range are also shown.

	R, largest 95% CL UL in range $\times 10^3$				
δm (MeV/c^2)	100 fs	150 fs	250 fs	333 fs	400 fs
380–429	12.6	2.7	0.73	0.43	0.33
430–479	11.2	2.4	0.65	0.39	0.29
480–529	14.8	3.2	0.85	0.51	0.39
530–579	10.7	2.3	0.63	0.38	0.29
580–629	10.9	2.3	0.63	0.38	0.29
630–679	14.2	3.0	0.81	0.49	0.37
680–729	9.5	2.0	0.56	0.33	0.25
730–779	10.8	2.3	0.63	0.37	0.28
780–829	12.8	2.8	0.74	0.45	0.34
830–880	12.2	2.6	0.70	0.42	0.32
380–880	14.8	3.2	0.85	0.51	0.39

in the entire $500\,{\rm MeV}/c^2$ mass range is also given. As expected, we find that the sensitivity depends strongly on the lifetime hypothesis.

The decay $\Xi_{cc}^+ \to \Lambda_c^+ K^- \pi^+$ could proceed through an intermediate $\Sigma_c^{++} \to \Lambda_c^+ \pi^+$ resonance. Such decays would be included in the yields and limits already shown, since the decay would wind up in the same final state. But we can be a bit smarter: if there were a large Σ_c^{++} component, imposing a cut on $m(\Lambda_c^+\pi^+)$ would reject a lot of combinatoric background and hence improve our sensitivity. For $\Sigma_c(2455)^{++}$, we require that the mass offset $[m(\Lambda_c^+\pi^+) - m_{\rm cand}(\Lambda_c^+)]$ is within $\pm 4\,{\rm MeV}/c^2$ of the world-average expected value, and for the wider $\Sigma_c(2520)^{++}$ we use a $\pm 15\,{\rm MeV}/c^2$ cut. The resulting δm spectra are shown in Fig. 3.17. No statistically significant excess is present.

3.3.9 Conclusions

We carried out a search for the decay $\Xi_{cc}^+ \to \Lambda_c^+ K^- \pi^+$ with a sample of $0.65\,{\rm fb}^{-1}$ of pp collisions but found no significant signal (as was expected from theory predictions of the cross-section). We set upper limits on the Ξ_{cc}^+ cross-section times branching fraction relative to the Λ_c^+ cross-section for a range of mass and lifetime hypotheses. Because of cuts in the software trigger and preselection requiring the Ξ_{cc}^+

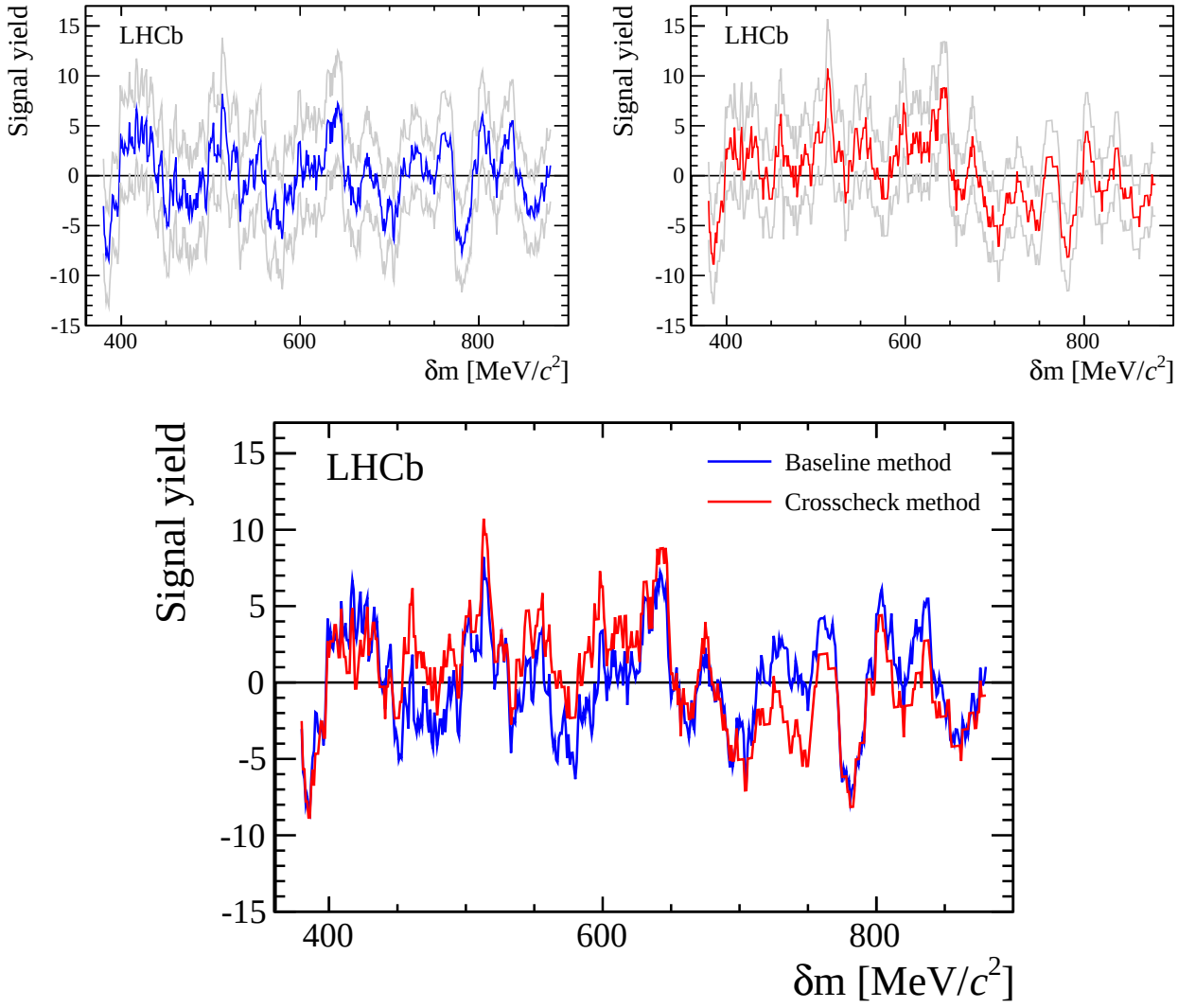

Figure 3.15: Measured signal yields as a function of δm. The upper two plots show the estimated signal yield as a dark line and the $\pm 1\sigma$ statistical error bands as light grey lines for (upper left) the baseline method and (upper right) the cross-check method. The central values of the two methods are compared in the lower plot and found to agree well.

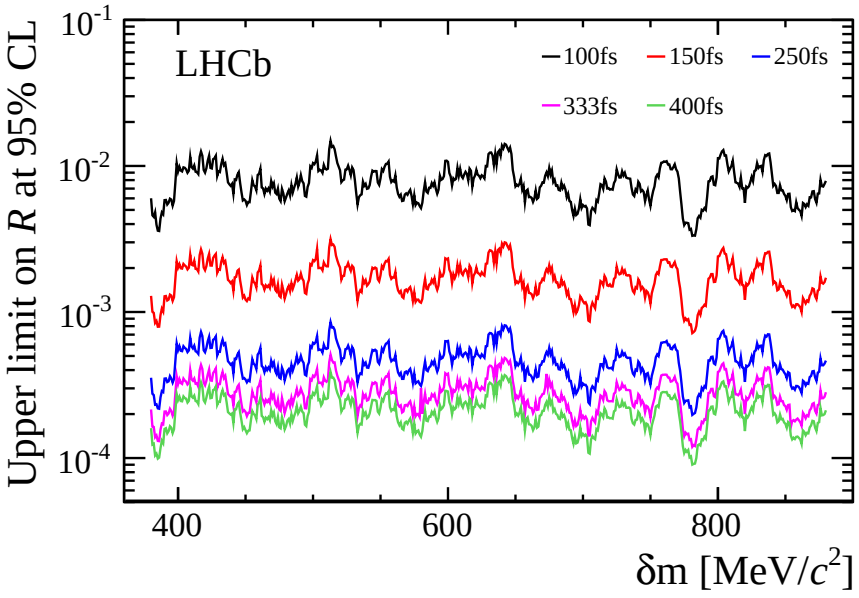

Figure 3.16: Upper limits on R at the 95% CL as a function of δm, for five Ξ_{cc}^{+} lifetime hypotheses.

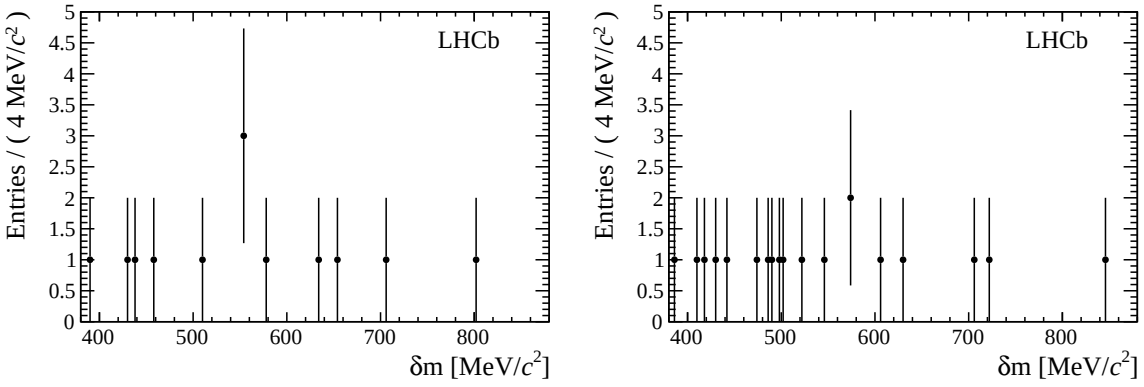

Figure 3.17: Mass difference spectrum requiring $2273 < m_{\rm cand}(\Lambda_c^+) < 2303\,{\rm MeV}/c^2$. Candidates are also required to be consistent with (left) an intermediate $\Sigma_c(2455)^{++}$, (right) an intermediate $\Sigma_c(2520)^{++}$.

decay vertex and its daughter tracks to be separated from the PV, the upper limit depends strongly on the lifetime, varying from 1.5×10^{-2} for 100 fs to 3.9×10^{-4} for 400 fs. Those limits are well below the value of R found at SELEX. But, as with previous null results, this doesn't exclude the SELEX claim: the difference could be due to the different production environment, or if the Ξ_{cc}^+ lifetime is indeed very short ($\ll 100$ fs). The good news is that LHCb's potential sensitivity is much better: a follow-on search on the full Run 1 dataset and with additional decay modes is in progress. The cuts that suppress short-lived Ξ_{cc} have been removed from the preselection. In addition, the trigger efficiency at short lifetimes is expected to be better for decay modes where the charmed hadron has a longer lifetime than the Λ_c^+ (*e.g.* $\Xi_{cc}^+ \to D^+ p K^-$ should be much more efficient than $\Xi_{cc}^+ \to \Lambda_c^+ K^- \pi^+$). There is every reason to hope that the elusive doubly charmed baryon should been visible in this analysis.

3.4 Summary and outlook

In this chapter, we've seen an overview of the spectroscopy of low-lying heavy baryon states, plus two examples of analyses investigating it. While we don't expect to find New Physics in this type of study, it is nonetheless good small-p physics. Even though the Quark Model has been around for a very long time and QCD nearly as long, spectroscopy still turns up plenty of surprises—as it should, for while the big picture is straightforward, the quantitative details are in the domain of non-perturbative QCD and require experiment as much as theory to pin down. These measurements may, in turn, be used to constrain models of QCD allowing key observables of the SM to be predicted with precision. To take a very recent example, precise measurements of the masses of the B^0 and B_s^0 mesons were among the inputs to QCD lattice calculations of hadronic matrix elements, which are necessary to obtain a number of physics parameters from experimental measurements—notably the ratio of CKM matrix elements $|V_{td}/V_{ts}|$ [135].

Chapter 4

Outlook

4.1 Machine and detector status

The first LHC run ended in early 2013. After a difficult start, it has proved a tremendous success. The data collected in 2011 and 2012 have been used for a great many analyses, not least of which is the discovery of the Higgs boson by the ATLAS and CMS collaborations. This sample still represents the bulk of the data, and new results continue to be published with them. In the field of flavour physics, these include discoveries of new states and numerous searches for New Physics. There is no hope of describing every measurement made at LHCb[1], but I will summarise some key results below. Meanwhile, the second LHC run has now started at a centre-of-mass energy of 13 TeV. The amount of data taken so far is only a fraction of the Run 1 sample, but it will soon take over as the focus of attention. For the general purpose detectors ATLAS and CMS, the difference is night and day: the increase in CM energy extends the sensitivity to NP into a regime never before probed, and even modest samples are of immediate interest. For LHCb, however, the increase in $\sqrt{s}$ brings roughly a doubling in the heavy flavour production cross-sections but does not by itself dramatically change the sensitivity. Nor will the instantaneous luminosity be much different from that seen in 2012; we are already close to the limits of the detector and its electronics. We will, though, benefit from an improved software trigger whose performance is systematically approaching that achieved offline. This is thanks both to a near-real-time calibration system and to a redesign of the trigger architecture that effectively increased the CPU time available per event[2] so that offline-quality reconstruction code could be run. Since our data-taking capacity is limited not by the output bandwidth of the farm but by the amount of offline storage available, having a better reconstruction and smarter selection will allow us to write more signal and less background. For the same reason, reductions in the event size will also translate into increased efficiencies for high-statistics modes, notably in charm. (But note the corollorary: with the increase in cross-sections, we will get twice as much signal produced but the same amount of output bandwidth in which to record it. So the trigger efficiency has to double just to keep up.)

The upshot is that for LHCb, Run 2 will be a significant improvement on Run 1. We expect to take roughly twice as much integrated luminosity (5–6 fb^{-1} *vs.* 3 fb^{-1}), with $b\overline{b}$ and $c\overline{c}$ cross-sections a factor of two larger, and a trigger efficiency that is improved for many modes. This brings us to roughly a factor of 5–10 in signal yields, but with quite a lot of variation from mode to mode depending on the trigger.

Looking further ahead, Run 2 will be followed by a long shutdown (LS2) and then by Run 3. Clearly, there would be limited interest in simply accumulating another 5–6 fb^{-1} over the course of a few years. Instead, a major programme of upgrades is planned for LS2, so that LHCb can operate at a

[1] Roughly 300 papers and 20 conference notes as of March 2016.

[2] This is not the place to get into the details, but a major factor is the introduction of deferred processing in which events passing the early trigger stages are saved to the local disks of the trigger computing farm nodes and then processed asynchronously. In this way, the higher-level software trigger can be run during the inter-fill periods when no new data is arriving; this in turn frees up CPU time during data-taking so that the lower-level software trigger can be more sophisticated.

much higher luminosity in Run 3 and increase the data sample by a further order of magnitude. Some detector subsystems will be replaced entirely, serving not only to improve their performance but also to enable them to handle the increased occupancy and output rate. The whole detector will be read out at 40 MHz and all trigger decisions will be taken in software. This removes one of the fundamental limitations of the existing architecture, namely the crude but fast L0 hardware trigger. The importance of this change is obvious at once if you consider that the current electronics is limited to a 1 MHz output but that during nominal Run 2 running we expect to produce $c\bar{c}$ pairs in the LHCb acceptance at a rate of around 1.2 MHz, and $b\bar{b}$ pairs at around 100 kHz. The hardware trigger only knows to how look for high-$p_{\rm T}$ muons tracks or calorimeter clusters, and how to count hits in the silicon detectors; it can distinguish heavy flavour events from light quark decays, and it can separate $b\bar{b}$ and $c\bar{c}$ events to a degree, but it cannot hope to distinguish between interesting and uninteresting heavy flavour decays[3]. Instead, the high-performance low-level software trigger and the deferred readout system already in place for Run 2 will be extended so handle the full 40 MHz output. In combination with a reduction in event size, this will enable an unprecedented volume of heavy flavour data to be recorded.

4.2 Key LHCb results

In the analyses so far published on the Run 1 data set, LHCb has not found a "smoking gun" indicating the presence of New Physics beyond the Standard Model. There are a number of results which are presently at the 3σ level; depending on your Bayesian prior, you can look at these either as the most promosing candidates for an observation in Run 2, or as a collection of results each of which is individually likely to be a statistical fluctuation. Either way, they are of interest and are outlined below. In addition, I will touch on results that, even though fully consistent with the SM, are nonetheless important for their ability to constrain the parameter space of NP; or which are of interest despite not sensitive to NP per se.

$B_s^0 \to \mu^+\mu^-$: [136] One of the most awaited results from the LHC Run 1 was the measurement of the branching fraction $\mathcal{B}(B_s^0 \to \mu^+\mu^-)$, which is highly suppressed in the SM (all SM diagrams are at least 1-loop, and are suppressed by helicity and CKM factors). By contrast, NP (and especially supersymmetry) could plausibly have an amplitude which is comparable to or even dominates the SM contribution. Combining the LHCb and CMS data, the decay mode was observed with a significance of 6.2σ but a value of $(2.8\,^{+0.7}_{-0.6}) \times 10^{-9}$ which is, sadly, perfectly compatible with the SM. The decay mode $B^0 \to \mu^+\mu^-$ is even more suppressed; the central value of its branching fraction is higher than expected [$(3.9^{+1.6}_{-1.4}) \times 10^{-10}$ compared to a SM value of $(1.06 \pm 0.09) \times 10^{-10}$], but the difference is not statistically significant at present. Still, precision measurements of $\mathcal{B}(B_s^0 \to \mu^+\mu^-)$ or of the ratio between B_s^0 and B^0 might reveal small discrepancies (and, if not, would further limit the SUSY parameter space).

$|V_{ub}|$ in Λ_b^0 decays: [137] The CKM parameter $|V_{ub}|$ has been measured at the e^+e^- B-factories Belle and BaBar using two classes of method: exclusive measurements of ratios of branching fractions, and inclusive measurements of all $b \to ul^-\overline{\nu}_l$ decays of B mesons. LHCb performed a measurement of the ratio of branching fractions $\mathcal{B}(\Lambda_b^0 \to p\mu^-\overline{\nu}_\mu)/\mathcal{B}(\Lambda_b^0 \to \Lambda_c^+\mu^-\overline{\nu}_\mu)$ and, with additional input for $|V_{cb}|$ and for a ratio of form factors obtained with lattice QCD, obtained $|V_{ub}| = (3.27 \pm 0.15 \pm 0.16 \pm 0.06) \times 10^{-3}$. This value is consistent with the average of previous exclusive measurements, but disagrees with the average of inclusive measurements at the 3.5σ level.

$B^0 \to K^{*0}\mu^+\mu^-$: [138] As with $B_s^0 \to \mu^+\mu^-$, this is a flavour-changing neutral current process and is suppressed in the SM. However, the topology is different: being a four-body decay, there are many more degrees of freedom in the final state, so in addition to the branching fraction itself

[3] This is already a problem for charm in Run 2: L0 rejects a good fraction of charm events more or less indiscriminately. As ever, the problems of charm today are the problems of b-physics tomorrow.

it is possible to construct a variety of angular observables describing the distribution in phase space. Among these is one known as P_5', which attracted attention previously because, in an analysis of the 2011 data, the results deviated visibly from the SM expectation in certain q^2 regions, corresponding to a local significance of 3.7σ [139]. After analysis of the $3\,\text{fb}^{-1}$ sample, the mode remains tantalizing: the local significance is still 3.7σ. Updates with further data will certainly be of interest.

R_K in $B^+ \to K^+ l^- l^+$: [140] In the SM, the coupling of electroweak interactions to leptons is universal. Aside from phase space corrections, one would therefore expect that the ratio R_K of branching fractions of $B^+ \to K^+ \mu^- \mu^+$ and $B^+ \to K^+ e^- e^+$ is unity, both overall and in any particular range of $q^2 = m^2(l^+ l^-)$. NP (such as a Z' that does not couple equally to electrons and muons) could break this universality. LHCb has measured R_K in the range $1 < q^2 < 6\,\text{GeV}^2/c^4$ with the Run 1 data and found a value of $0.745\,^{+0.090}_{-0.074} \pm 0.036$, which differs from one at a significance of 2.6σ. While this is only marginally significant, it is interesting because it is so closely related to the $B^0 \to K^{*0}\mu^+\mu^-$ anomaly discussed above. Analysis of the related ratio R_{K^*} of the branching fractions $B^0 \to K^{*0} l^- l^+$ is ongoing.

$\mathcal{B}(\overline{B}^0 \to D^{*+} l^- \bar{\nu}_l)$: [141] Belle and BaBar have previously measured the ratios of branching fractions $R_D \equiv \mathcal{B}(\overline{B}^0 \to D^+ \tau^- \bar{\nu}_\tau)/\mathcal{B}(\overline{B}^0 \to D^+ \mu^- \bar{\nu}_\mu)$ and $R_{D^*} \equiv \mathcal{B}(\overline{B}^0 \to D^{*+} \tau^- \bar{\nu}_\tau)/\mathcal{B}(\overline{B}^0 \to D^{*+} \mu^- \bar{\nu}_\mu)$, finding values in tension with the SM. The discrepancy is below 3σ for each individual measurement, but they are systematically above the SM value. LHCb has now measured R_{D^*} to be $0.336 \pm 0.027 \pm 0.030$, in agreement with the B-factory results and 2.1σ above the SM expectation. Combining the LHCb, BABAR, and Belle results, the world average value differs from the SM expectation by 3.9σ [24]. (Note that the final state $\overline{B}^0 \to D^{*+}\tau^-\bar{\nu}_\tau$, $\tau^- \to \mu^- \nu_\tau \overline{\nu}_\mu$ contains three neutrinos; making this measurement at LHCb was quite a feat!)

Exotic hadrons: Ref. [142, 109] LHCb has confirmed the existence and exotic nature of the $Z(4430)^-$ meson, which has minimal quark content $c\bar{c}d\overline{u}$ and therefore cannot be a conventional $(q_1\bar{q}_2)$ meson. This state was first observed by Belle, and was studied by LHCb in the decay $B^0 \to \psi'\pi^- K^+$, with $Z(4430)^- \to \psi'\pi^-$ appearing as an intermediate resonance. The analysis was particularly compelling, using a combination of amplitude analysis and a model-independent measurement of the phase motion of the resonance. The same techniques were applied to the related decay $\Lambda_b^0 \to J/\psi\, K^- p$, and it was shown that the structure in the $J/\psi\, p$ mass spectrum required the existence of two pentaquark resonances with minimal quark content $c\bar{c}uud$; again, this cannot be a conventional $(q_1 q_2 q_3)$ baryon state. While these states are not *forbidden* and their discovery does not constitute NP, they are nonetheless of considerable interest—the existence of pentaquarks in particular has been a matter of speculation for decades—and studies of their properties, starting with the nature of their binding, will be followed closely.

4.3 The longer term

As well as Runs 2 and 3 of the LHC, there will be a programme of heavy flavour physics at Belle-II, which is scheduled to begin data-taking at high luminosity in 2019. There is considerable complementarity between LHCb and Belle-II: while Belle-II will struggle to compete in terms of raw statistics for decays to final states containing only charged tracks[4], it will be on a more even footing for modes containing a K^0_S and will have a distinct advantage for decay modes with a γ or π^0, modes with missing particles, and inclusively reconstructed decays. The competition will be healthy for LHCb, and in many instances the combination of results allows for new or improved tests of the SM[5]. Between the

[4] Especially for charm, due to the huge LHC cross-section; and even more so for B_s^0, B_c^+, and b-baryons which are too heavy to produce at the $\Upsilon(4S)$ resonance. Belle-II is capable of running at the $\Upsilon(5S)$ to produce $B_s^0\overline{B}_s^0$ pairs, but the cross-section is not as favourable as for $B\overline{B}$ at the $\Upsilon(4S)$.

[5] The comparison of inclusive and exclusive $|V_{ub}|$ measurements discussed above is a good example. More broadly, the whole history of unitarity triangle measurements is an illustration of the power of the approach.

two experiments, we can look forward to a great increase in NP reach, with sensitivities improving by an order of magnitude or more (see Refs. [143, 144] for concrete numbers). While nothing in research is guaranteed, and Nature has been unusually protective of the Standard Model, we know that it must crack at some point and we have reason to be hopeful that heavy flavour physics will play a part in revealing the NP that lies beyond.

4.4 Perspectives at LPNHE

The analyses presented in this thesis fall into two broad categories: searches for phenomena that are sensitive to NP (in this case, *CP* violation in charm), and studies that are not sensitive to NP but which improve our understanding of the SM (in this case, baryon spectroscopy). Both kinds are important to the health of a research group. Searches for NP are the main goal of experimental high energy physics as a field at present, and are the core around which the LPNHE group is built. But while we can be confident that there is NP waiting to be discovered, the chance of finding it in any given search is slim; SM measurements allow for more modest but concrete advances in our understanding. And of course there is coupling between the two: we often have systematic uncertainties on NP measurements associated with SM processes[6].

As well as the analyses presented in this thesis (and follow-on work, discussed below), the LPNHE group is involved in two main areas: studies of multi-body charmless hadronic B-meson decays and of B decays of the form $b \to s l^+ l^-$. In both cases the interest comes from potential sensitivity to the presence of NP, which may enter via loop diagrams. We have already discussed $B^0 \to K^{*0}\mu^+\mu^-$ and the interest there is clear; there will also be follow-on work in related modes, especially lepton-flavour-violating decays such as $B^0 \to K^{*0}\mu^+e^-$.

For charmless B decays the phenomenology varies greatly from mode to mode, since the contributing diagrams and their CKM phases depend upon the final state. Recent work in this area at LPNHE has focused on decays of the form $(B^0, B_s^0) \to K^0_S h^+ h'^-$, where h and h' denote a hadron that can be either a kaon or a pion, and in particular on the decays $(B^0, B_s^0) \to K^0_S K^+ K^-$. There are several Feynman diagrams that can contribute, but the most important are tree-level decays with a $b \to u\bar{u}d$ weak transition, and penguin (loop) diagrams with a $b \to sq\bar{q}$ or $b \to dq\bar{q}$ transition. The CKM matrix element associated with the $b \to u$ vertex is small in magnitude and has a large weak phase (see Sec. 2.1). In some decays, such as $B_s^0 \to K^0_S \pi^+\pi^-$, there is no further suppression to the tree diagram and it should still dominate. For such tree-dominated modes, we have the potential to measure CKM phases in a theoretically clean way, most notably obtaining constraints on γ through $B_s^0 \to K^0_S \pi^+\pi^-$. In other decays, the tree diagram may be colour-suppressed (*e.g.* $B_s^0 \to K^0_S K^+ K^-$, where the W emission is internal) and/or further CKM-suppressed (*e.g.* $B^0 \to K^0_S K^+ K^-$, where the W converts to $\bar{u}s$) such that the penguin diagram dominates. For such penguin-dominated modes, we expect to see mixing-induced CPV, which in the SM will be no different between our charmless $b \to (s/d)q\bar{q}$ and the charmful $b \to sc\bar{c}$ (*e.g.* the well-known $B^0 \to J/\psi K^0_S$ and $B_s^0 \to J/\psi\phi$). However, if there are additional contributions from NP loop diagrams, these could change the behaviour of the charmless modes—but would not have a significant impact on the $b \to sc\bar{c}$ modes where the SM diagram would still dominate. Thus, we can test for the presence of NP by comparing results from the charmless decays to the $b \to sc\bar{c}$ control modes.

Both of the charmless analyses discussed above (constraints on γ, mixing-induced CPV in penguin-dominated modes) are long-term projects. They require time-dependent amplitude analyses, for which there are several preparatory steps, notably time-integrated amplitude analyses to build a decay model,

[6] To take just one example, when studying direct *CP* violation the yield asymmetries that we observe depend on the underlying *CP* asymmetries that we want to determine but also on the particles' production asymmetries. In Sec. 2.6 we had to work hard to cancel out these production asymmetries; the double-difference method adopted got rid of them, but at the price of losing sensitivity to the individual asymmetries $A_{CP}(D^0 \to K^-K^+)$ and $A_{CP}(D^0 \to \pi^-\pi^+)$. A better understanding of the production asymmetry (and of detector effects such as efficiency asymmetries) would have increased our sensitivity to NP.

and study of the time acceptance of these modes at LHCb and how to take it into account[7]. They will also benefit from larger yields than are available at present—not only because of the tiny branching fractions of CKM-suppressed charmless decays, but also because of the reduced K^0_S reconstruction efficiency of LHCb[8]. For both of these reasons, these analyses have begun with observations and measurements of branching fractions [146] in the Run 1 data. While it may be possible to do a trial run with the Run 1+2 data, the full time-dependent analyses will come into their own after the upgrade when an order of magnitude more events will be available.

As well as this long-term analysis project, I plan to carry out a number of smaller, more self-contained analyses with the data already collected[9]

- First, there is a very natural follow-on to the Ξ_{cc}^+ search presented in Sec. 3.3. The original analysis used only one decay mode, and only $0.65\,\text{fb}^{-1}$ of data. Since then, the full Run 1 data sample has been reprocessed with a greater range of modes and a more efficient preselection. There is good discovery potential here, and quite a bit of interest from the theory community.

- Second, it would be straightforward to extend the study of $\Xi_b^0\pi^-$ presented in Sec. 3.2 to the isospin partner final state, $\Xi_b^-\pi^+$. This would allow the CMS observation of the Ξ_b^{*0} to be confirmed, and its mass and width to be measured with much better precision.

- Third, there is a wide variety of other studies that could be carried out in the Ξ_b system. In particular, by analogy with the charm system we might expect to see narrow resonances in the $\Xi_b\pi^-\pi^+$ final state decaying via an intermediate Ξ_b' or Ξ_b^*. Ultimately, we may be limited by the production cross-section (which tends to drop rapidly with mass) and the efficiency to reconstruct multiple soft pions.

- Fourth, one can carry out a search for baryon number violation by looking for Ξ_b^0 oscillations. These might occur in models of NP in which the flavour interactions were entirely diagonal [147, 148], which would allow BNV without violating current constraints on the proton lifetime. The experimental signature at LHCb would be a particle produced as a Ξ_b^0 that decays to an antibaryon final state (or vice versa). The $\Xi_b^{(\prime,*)-} \to \Xi_b^0\pi^-$ sample presented in Sec. 3.2 is ideal for this, since the soft pion tags the initial flavour in a very clean way. Of course, even if such an effect were present it would likely be invisible in the Run 1 sample of only a few hundred events, but the groundwork will be laid for upgrade studies with much higher statistics.

... and I am equally sure that new, interesting, and unanticipated analyses will pop up over the coming years as we take more data.

[7] Roughly speaking, this means either a fully time-unbiased selection from the trigger to the ntuple, or a method to correct for it. Such a correction could come from Monte Carlo, if the systematic uncertainties are tolerable; otherwise a data-driven correction such as swimming [145] is needed.

[8] The origin of this problem is pure physics: K^0_S have a finite lifetime, with $c\tau = 2.7\,\text{cm}$ in the rest frame. Due to the large boost at LHCb, many will fly for several metres in the lab frame. But to calculate the momentum of the daughter tracks, we need to measure their position both upstream and downstream of the magnet. Any K^0_S that decay after the TT station (see Fig. 1.1) will be lost. Note also that K^0_S which decay between the VELO and the TT will have poorer momentum and vertex resolution than the minority which decay inside the VELO.

[9] Several of these are in progress at the time of writing, and there is a non-zero risk that some public results will be available before the HDR soutenance.

Appendix A

Acknowledgement of collaborators

Each of the analyses presented in this document was carried out in close collaboration with one or more colleagues. Specificially:

$D^+ \to K^-K^+\pi^+$**:** The analysis in paper [40] was done in collaboration with my student Hamish Gordon (Oxford); Sandra Amato, Erica Polycarpo, and Danielle Martins Tostes (UFRJ); Carla Gobel and Josue Molina (PUC); and Alberto Reis (CBPF).

ΔA_{CP}**:** The analysis on $0.37\,\text{pb}^{-1}$ in conference note [48] and that on $0.6\,\text{fb}^{-1}$ in paper [49] were both done in collaboration with Guy Wilkinson (Oxford); and Angelo Carbone and Vincenzo Vagnoni (Bologna). The analysis on $1.0\,\text{fb}^{-1}$ in conference note [50] was done in collaboration with the above plus Stefano Perazzini (Bologna), Chris Thomas (Oxford), and Evelina Gersabeck (Heidelberg)

Ξ_b**:** The analysis in paper [84] was done in collaboration with Steve Blusk (Syracuse).

Ξ_{cc}**:** The analysis in paper [108] was done in collaboration with Patrick Spradlin (Glasgow); Yuanning Gao, Feng Zhang, and Liang Zhong (Tsinghua).

None of these papers would have been possible without the work of a large number of collaborators, notably the design, construction, and operation of the LHCb detector; offline data reconstruction and processing; tuning and development of the Monte Carlo simulation; and the collaboration's internal review process. Neither would they have been possible without the construction and operation of the LHC itself, or the support of numerous governments and funding agencies. I dare not attempt an exhaustive list, but should note in particular STFC (which supported my work at Oxford) and the Université Pierre et Marie Curie and CNRS (which support my work at UPMC).

Appendix B

Extra material

This appendix contains extra material which is relevant but not critical to the analyses discussed in this document.

B.1 Ξ_b feed-down

With a very specific configuration of other excited Ξ_b states, it is possible to produce a narrow peak in the $\Xi_b^0\pi^-$ mass spectrum without invoking a $\Xi_b^{\prime -}$ state. This can occur for the decay chain:

$$\Xi_b^{**-} \to \Xi_b^{\prime 0}\pi^-,\ \Xi_b^{\prime 0} \to \Xi_b^0\pi^0$$

where the Ξ_b^{**-} is the $J^P = 1/2^-$ state analagous to the $\Xi_c(2790)$. If the decays are close to threshold, the tracks will be kinematically correlated such that combining the Ξ_b^0 daughter with the π^- from the Ξ_b^{**-} (and ignoring the π^0) would produce a structure in the $m(\Xi_b^0\pi^-)$ spectrum. In order for this feed-down to produce a fake peak consistent with what we see in data, several criteria must be fulfilled:

1. The process $\Xi_b^{\prime -} \to \Xi_b^0\pi^-$ must be below threshold, i.e. $m(\Xi_b^{\prime -}) < m(\Xi_b^0) + m(\pi^-)$. Otherwise we would still see a real $\Xi_b^{\prime -}$ peak.

2. The process $\Xi_b^{**-} \to \Xi_b^{\prime 0}\pi^-$ must be above threshold by $3.653 \pm 0.018 \pm 0.006\,\mathrm{MeV}/c^2$, in order to produce a peak where we see it in data, i.e. $m(\Xi_b^{**-}) = m(\Xi_b^{\prime 0}) + m(\pi^-) + 3.65\ \mathrm{MeV}/c^2$.

3. The process $\Xi_b^{\prime 0} \to \Xi_b^0\pi^0$ must be above threshold but by a very small amount. This follows from the fact that the width of the feed-down peak increases rapidly with the Q-value yet the peak observed in data is very narrow. If the decay to $\Xi_b^0\pi^0$ were below threshold then it would instead go 100% to $\Xi_b^0\gamma$ with a much larger Q-value so that the feed-down peak would be broad; if the decay to $\Xi_b^0\pi^0$ were much above threshold then the feed-down peak would again be broad. From toy MC studies we estimate that this means the $\Xi_b^{\prime 0}$ is at most $2\,\mathrm{MeV}/c^2$ above threshold, so: $0 < m(\Xi_b^{\prime 0}) - m(\Xi_b^0) - m(\pi^0) \lesssim 2\,\mathrm{MeV}/c^2$.

4. Combining conditions 1 and 3, it follows that $m(\Xi_b^{\prime -}) - m(\Xi_b^{\prime 0}) < m(\pi^-) - m(\pi^0) = 4.6\,\mathrm{MeV}/c^2$. This does not leave much room, given the typical isospin splittings seen in other Ξ_b and Ξ_c systems. (But does not totally exclude the feed-down hypothesis, since the hyperfine corrections can reduce the isospin splitting relative to that seen in the ground state.)

5. The isospin partner process $\Xi_b^{**0} \to \Xi_b^{\prime -}\pi^+$ must be below threshold, else we'd see a corresponding peak in the wrong-sign spectrum, so: $m(\Xi_b^{**0}) - m(\Xi_b^{\prime -}) - m(\pi^+) < 0$.

If we collect the above constraints and in addition impose:

$$\begin{aligned} m(\Xi_b^-) - m(\Xi_b^0) &= 5.92 \pm 0.60 \pm 0.23\ \mathrm{MeV}/c^2 \\ m(\Xi_b^{*0}) - m(\Xi_b^-) - m(\pi^+) &= 14.84 \pm 0.74 \pm 0.28\ \mathrm{MeV}/c^2 \\ m(\Xi_b^{*-}) - m(\Xi_b^0) - m(\pi^-) &= 23.96 \pm 0.12 \pm 0.06\ \mathrm{MeV}/c^2 \end{aligned}$$

then we have most of the constraints necessary to fully determine the spectrum of low-lying Ξ_b states. We generate toy MC with these values (Gaussian-fluctuated within their errors) and in addition generate

$$\begin{aligned} m(\Xi_b^{\prime 0}) - m(\Xi_b^0) &= \text{Gaus}(\mu = 135.0, \sigma = 10.0) \\ m(\Xi_b^{\prime -}) - m(\Xi_b^{\prime 0}) &= \text{Gaus}(\mu = 4.0, \sigma = 2.0) \\ m(\Xi_b^{**-} - m(\Xi_b^{**0}) &= \text{Gaus}(\mu = 3.0, \sigma = 2.0) \end{aligned}$$

indicating Gaussian random distributions with the mean and standard deviation shown. These last three are deliberately generated within fairly wide ranges. We then require that the toy spectra fulfil the five conditions set out above, which rejects a large fraction of the toys. Note that we apply only the conditions above so that, for example, some of the surviving toys have $m(\Xi_b^{\prime 0}) > m(\Xi_b^{\prime -})$, which is not terribly likely but in principle not excluded by the data. The splittings are highly constrained, and in this scenario we estimate

$$\begin{aligned} m(\Xi_b^{**-}) - m(\Xi_b^0) &= 279.0 \pm 0.5 \text{ MeV}/c^2 \\ m(\Xi_b^{\prime 0}) - m(\Xi_b^0) &= 135.8 \pm 0.5 \text{ MeV}/c^2 \\ m(\Xi_b^{\prime -}) - m(\Xi_b^0) &= 138.3 \pm 1.0 \text{ MeV}/c^2. \end{aligned}$$

Bibliography

[1] R. D. Peccei and H. R. Quinn, *CP Conservation in the Presence of Instantons*, Phys. Rev. Lett. **38** (1977) 1440.

[2] R. D. Peccei and H. R. Quinn, *Constraints Imposed by CP Conservation in the Presence of Instantons*, Phys. Rev. **D16** (1977) 1791.

[3] BaBar, J. P. Lees *et al.*, *Measurement of an Excess of $\bar{B} \to D^{(*)}\tau^-\bar{\nu}_\tau$ Decays and Implications for Charged Higgs Bosons*, Phys. Rev. **D88** (2013) 072012, arXiv:1303.0571.

[4] LHCb collaboration, A. A. Alves Jr. *et al.*, *The LHCb detector at the LHC*, JINST **3** (2008) S08005.

[5] LHCb collaboration, R. Aaij *et al.*, *LHCb detector performance*, Int. J. Mod. Phys. **A30** (2015), no. 07 1530022, arXiv:1412.6352.

[6] LHCb collaboration, R. Aaij *et al.*, *Measurement of the track reconstruction efficiency at LHCb*, JINST **10** (2015) P02007, arXiv:1408.1251.

[7] R. Aaij *et al.*, *Performance of the LHCb Vertex Locator*, JINST **9** (2014) P09007, arXiv:1405.7808.

[8] R. Arink *et al.*, *Performance of the LHCb Outer Tracker*, JINST **9** (2014) P01002, arXiv:1311.3893.

[9] F. Archilli *et al.*, *Performance of the muon identification at LHCb*, JINST **8** (2013) P10020, arXiv:1306.0249.

[10] R. Aaij *et al.*, *The LHCb trigger and its performance in 2011*, JINST **8** (2013) P04022, arXiv:1211.3055.

[11] M. Adinolfi *et al.*, *Performance of the LHCb RICH detector at the LHC*, Eur. Phys. J. **C73** (2013) 2431, arXiv:1211.6759.

[12] A. A. Alves Jr. *et al.*, *Performance of the LHCb muon system*, JINST **8** (2013) P02022, arXiv:1211.1346.

[13] BaBar, Belle, A. J. Bevan *et al.*, *The Physics of the B Factories*, Eur. Phys. J. **C74** (2014), no. 11 3026, arXiv:1406.6311.

[14] Particle Data Group, K. A. Olive *et al.*, *Review of particle physics*, Chin. Phys. **C38** (2014) 090001.

[15] X. Chang *et al.*, *LHCb $\triangle A_{CP}$ of D Meson and R-Parity Violation*, arXiv:1201.2565.

[16] BaBar Collaboration, B. Aubert *et al.*, *Evidence for D^0-$\overline{D}^0$ mixing*, Phys. Rev. Lett. **98** (2007) 211802, arXiv:hep-ex/0703020.

[17] Belle Collaboration, M. Staric *et al.*, *Evidence for D^0-$\overline{D}^0$ mixing*, Phys. Rev. Lett. **98** (2007) 211803, arXiv:hep-ex/0703036.

[18] A. A. Petrov, *Long-distance effects in charm mixing*, arXiv:1312.5304.

[19] M. A. Shifman and M. B. Voloshin, *On Annihilation of Mesons Built from Heavy and Light Quark and anti-B0 <—> B0 Oscillations*, Sov. J. Nucl. Phys. **45** (1987) 292, [Yad. Fiz.45,463(1987)].

[20] A. F. Falk *et al.*, *The D^0-$\overline{D}^0$ mass difference from a dispersion relation*, Phys. Rev. **D69** (2004) 114021, arXiv:hep-ph/0402204.

[21] E. Golowich, J. Hewett, S. Pakvasa, and A. A. Petrov, *Implications of D^0-$\overline{D}^0$ mixing for new physics*, Phys. Rev. **D76** (2007) 095009, arXiv:0705.3650.

[22] S. Bianco, F. L. Fabbri, D. Benson, and I. Bigi, *A Cicerone for the physics of charm*, Riv. Nuovo Cim. **26N7** (2003) 1, arXiv:hep-ex/0309021.

[23] M. Bobrowski, A. Lenz, and T. Rauh, *Short distance D^0-$\overline{D}^0$ mixing*, arXiv:1208.6438.

[24] Heavy Flavor Averaging Group (HFAG), Y. Amhis *et al.*, *Averages of b-hadron, c-hadron, and τ-lepton properties as of summer 2014*, arXiv:1412.7515, and online update at http://www.slac.stanford.edu/xorg/hfag.

[25] LHCb Collaboration, R. Aaij *et al.*, *Observation of D^0-$\overline{D}^0$ oscillations*, Phys. Rev. Lett. **110** (2013) 101802, arXiv:1211.1230.

[26] LHCb collaboration, R. Aaij *et al.*, *Measurement of D^0-$\overline{D}^0$ mixing parameters and search for CP violation using $D^0 \to K^+\pi^-$ decays*, Phys. Rev. Lett. **111** (2013) 251801, arXiv:1309.6534.

[27] CDF Collaboration, T. A. Aaltonen *et al.*, *Observation of D^0-$\overline{D}^0$ mixing using the CDF II detector*, Phys. Rev. Lett. **111** (2013) 231802, arXiv:1309.4078.

[28] Belle Collaboration, B. R. Ko *et al.*, *Observation of D^0-$\overline{D}^0$ mixing in e^+e^- collisions*, Phys. Rev. Lett. **112** (2014) 111801, arXiv:1401.3402.

[29] M. Gersabeck *et al.*, *On the interplay of direct and indirect CP violation in the charm sector*, J. Phys. **G39** (2012) 045005, arXiv:1111.6515.

[30] Belle Collaboration, T. Peng *et al.*, *Measurement of D^0-$\overline{D}^0$ mixing and search for indirect CP violation using $D^0 \to K^0_S\pi^+\pi^-$ decays*, Phys. Rev. **D89** (2014) 091103, arXiv:1404.2412.

[31] LHCb collaboration, R. Aaij *et al.*, *Measurements of indirect CP asymmetries in $D^0 \to K^-K^+$ and $D^0 \to \pi^-\pi^+$ decays*, Phys. Rev. Lett. **112** (2014) 041801, arXiv:1310.7201.

[32] A. L. Kagan and M. D. Sokoloff, *On indirect CP violation and implications for D^0-$\overline{D}^0$ and B^0_s-$\overline{B}^0_s$ mixing*, Phys. Rev. **D80** (2009) 076008, arXiv:0907.3917.

[33] I. I. Bigi, *No pain, no gain: On the challenges and promises of charm studies*, arXiv:0907.2950.

[34] M. Bobrowski, A. Lenz, J. Riedl, and J. Rohrwild, *How large can the SM contribution to CP violation in D^0-$\overline{D}^0$ mixing be?*, JHEP **1003** (2010) 009, arXiv:1002.4794.

[35] M. Bobrowski, *Charm mixing in the Standard Model: the inclusive approach*, arXiv:1302.4208.

[36] Y. Grossman, A. L. Kagan, and Y. Nir, *New physics and CP violation in singly Cabibbo suppressed D decays*, Phys. Rev. **D75** (2007) 036008, arXiv:hep-ph/0609178.

[37] G. Hiller, M. Jung, and S. Schacht, *SU(3)-flavor anatomy of non-leptonic charm decays*, Phys. Rev. **D87** (2013) 014024, arXiv:1211.3734.

[38] B. Bhattacharya, M. Gronau, and J. L. Rosner, *CP asymmetries in singly-Cabibbo-suppressed D decays to two pseudoscalar mesons*, Phys. Rev. **D85** (2012) 054014, arXiv:1201.2351.

[39] LHCb collaboration, R. Aaij *et al.*, *Prompt charm production in pp collisions at sqrt(s)=7 TeV*, Nucl. Phys. **B871** (2013) 1, arXiv:1302.2864.

[40] LHCb, R. Aaij *et al.*, *Search for CP violation in $D^+ \to K^-K^+\pi^+$ decays*, Phys. Rev. **D84** (2011) 112008, arXiv:1110.3970.

[41] CLEO Collaboration, G. Bonvicini *et al.*, *Updated measurements of absolute D^+ and D^0 hadronic branching fractions and $\sigma(e^+e^- \to D\overline{D})$ at $E_{\rm cm} = 3774$ MeV*, Phys. Rev. **D89** (2014) 072002, arXiv:1312.6775.

[42] BaBar Collaboration, J. P. Lees *et al.*, *Search for direct CP violation in singly Cabibbo-suppressed $D^\pm \to K^+K^-\pi^\pm$ decays*, Phys. Rev. **D87** (2013) 052010, arXiv:1212.1856.

[43] I. Bediaga *et al.*, *On a CP anisotropy measurement in the Dalitz plot*, Phys. Rev. **D80** (2009) 096006, arXiv:0905.4233.

[44] CLEO Collaboration, P. Rubin *et al.*, *Search for CP Violation in the Dalitz-Plot Analysis of $D^+ \to K^-K^+\pi^+$*, Phys. Rev. **D78** (2008) 072003, arXiv:0807.4545.

[45] LHCb collaboration, R. Aaij *et al.*, *Search for CP violation in $D^+ \to \phi\pi^+$ and $D_s^+ \to K_S^0\pi^+$ decays*, JHEP **1306** (2013) 112, arXiv:1303.4906.

[46] M. Williams, *Observing CP Violation in Many-Body Decays*, Phys. Rev. **D84** (2011) 054015, arXiv:1105.5338.

[47] LHCb, R. Aaij *et al.*, *Measurements of CP violation in the three-body phase space of charmless $B^\pm$ decays*, Phys. Rev. **D90** (2014) 112004, arXiv:1408.5373.

[48] LHCb collaboration, *A search for time-integrated CP violation in $D^0 \to h^+h^-$ decays and a measurement of the D^0 production asymmetry*, Jun, 2011. LHCb-CONF-2011-023.

[49] LHCb, R. Aaij *et al.*, *Evidence for CP violation in time-integrated $D^0 \to h^-h^+$ decay rates*, Phys. Rev. Lett. **108** (2012) 111602, arXiv:1112.0938.

[50] LHCb collaboration, *A search for time-integrated CP violation in $D^0 \to K^-K^+$ and $D^0 \to \pi^-\pi^+$ decays*, Mar, 2013. LHCb-CONF-2013-003.

[51] CDF, T. Aaltonen *et al.*, *Measurement of CP–violating asymmetries in $D^0 \to \pi^+\pi^-$ and $D^0 \to K^+K^-$ decays at CDF*, Phys. Rev. **D85** (2012) 012009, arXiv:1111.5023.

[52] I. I. Bigi, A. Paul, and S. Recksiegel, *Conclusions from CDF Results on CP Violation in $D^0 \to \pi^+\pi^-$, K^+K^- and Future Tasks*, JHEP **06** (2011) 089, arXiv:1103.5785.

[53] T. Feldmann, S. Nandi, and A. Soni, *Repercussions of flavour symmetry breaking on CP violation in D-meson decays*, JHEP **1206** (2012) 007, arXiv:1202.3795.

[54] LHCb collaboration, R. Aaij *et al.*, *Measurement of CP asymmetry in $D^0 \to K^-K^+$ and $D^0 \to \pi^-\pi^+$ decays*, JHEP **1407** (2014) 041, arXiv:1405.2797.

[55] CDF Collaboration, T. Aaltonen *et al.*, *Measurement of the difference of CP–violating asymmetries in $D^0 \to K^+K^-$ and $D^0 \to \pi^+\pi^-$ decays at CDF*, Phys. Rev. Lett. **109** (2012) 111801, arXiv:1207.2158.

[56] Belle, B. R. Ko, *Direct CP violation in charm at Belle*, PoS **ICHEP2012** (2013) 353, arXiv:1212.1975.

[57] J. Brod, A. L. Kagan, and J. Zupan, *Size of direct CP violation in singly Cabibbo-suppressed D decays*, Phys. Rev. **D86** (2012) 014023, arXiv:1111.5000.

[58] J. Brod, Y. Grossman, A. L. Kagan, and J. Zupan, *A consistent picture for large penguins in $D \to \pi^+\pi^-$, K^+K^-*, JHEP **1210** (2012) 161, arXiv:1203.6659.

[59] LHCb, R. Aaij *et al.*, *Measurement of the difference of time-integrated asymmetries in $D^0 \to K^-K^+$ and $D^0 \to \pi^-\pi^+$ decays*, arXiv:1602.03160, submitted to Phys. Rev. Lett.

[60] LHCb, R. Aaij *et al.*, *Measurement of the D+/- production asymmetry in 7 TeV pp collisions*, Phys. Lett. **B718** (2013) 902, arXiv:1210.4112.

[61] LHCb, R. Aaij *et al.*, *Model-independent measurement of mixing parameters in $D^0 \to K_S\pi^+\pi^-$ decays*, arXiv:1510.01664.

[62] LHCb, R. Aaij *et al.*, *Measurements of prompt charm production cross-sections in pp collisions at $\sqrt{s} = 13\,\text{TeV}$*, arXiv:1510.01707.

[63] LHCb, R. Aaij *et al.*, *Measurement of mixing and CP violation parameters in two-body charm decays*, JHEP **04** (2012) 129, arXiv:1112.4698.

[64] LHCb, R. Aaij *et al.*, *Measurement of indirect CP asymmetries in $D^0 \to K^-K^+$ and $D^0 \to \pi^-\pi^+$ decays using semileptonic B decays*, JHEP **04** (2015) 043, arXiv:1501.06777.

[65] LHCb Collaboration, R. Aaij *et al.*, *Search for CP violation in $D^\pm \to K^0_S K^\pm$ and $D^\pm_s \to K^0_S\pi^\pm$ decays*, JHEP **1410** (2014) 25, arXiv:1406.2624.

[66] LHCb, R. Aaij *et al.*, *Measurement of the time-integrated CP asymmetry in $D^0 \to K^0_S K^0_S$ decays*, arXiv:1508.06087.

[67] LHCb collaboration, R. Aaij *et al.*, *Search for CP violation in $D^0 \to \pi^-\pi^+\pi^0$ decays with the energy test*, arXiv:1410.4170.

[68] LHCb collaboration, R. Aaij *et al.*, *Search for CP violation using T-odd correlations in $D^0 \to K^+K^-\pi^+\pi^-$ decays*, JHEP **1410** (2014) 5, arXiv:1408.1299.

[69] LHCb collaboration, R. Aaij *et al.*, *Search for CP violation in the decay $D^+ \to \pi^-\pi^+\pi^+$*, Phys. Lett. **B728** (2014) 585, arXiv:1310.7953.

[70] LHCb Collaboration, R. Aaij *et al.*, *Model-independent search for CP violation in $D^0 \to K^-K^+\pi^-\pi^+$ and $D^0 \to \pi^-\pi^+\pi^+\pi^-$ decays*, Phys. Lett. **B726** (2013) 623, arXiv:1308.3189.

[71] N. Isgur and M. B. Wise, *WEAK TRANSITION FORM-FACTORS BETWEEN HEAVY MESONS*, Phys. Lett. **B237** (1990) 527.

[72] N. Isgur and M. B. Wise, *Weak Decays of Heavy Mesons in the Static Quark Approximation*, Phys. Lett. **B232** (1989) 113.

[73] N. Isgur and M. B. Wise, *Spectroscopy with heavy quark symmetry*, Phys. Rev. Lett. **66** (1991) 1130.

[74] M. Gell-Mann, *A Schematic Model of Baryons and Mesons*, Phys. Lett. **8** (1964) 214.

[75] G. Zweig, *An SU(3) model for strong interaction symmetry and its breaking, Part 1*, , CERN-TH-401.

[76] G. Zweig, *An SU(3) model for strong interaction symmetry and its breaking, Part 2*, , CERN-TH-412, Published in 'Developments in the Quark Theory of Hadrons'. Volume 1. Edited by D. Lichtenberg and S. Rosen. Nonantum, Mass., Hadronic Press, 1980. pp. 22-101.

[77] S. Okubo, *Note on unitary symmetry in strong interactions*, Prog. Theor. Phys. **27** (1962) 949.

[78] M. Gell-Mann, *Symmetries of baryons and mesons*, Phys. Rev. **125** (1962) 1067.

[79] S. Gasiorowicz and J. L. Rosner, *Hadron spectra and quarks*, Am. J. Phys. **49** (1981) 954.

[80] A. De Rujula, H. Georgi, and S. L. Glashow, *Hadron Masses in a Gauge Theory*, Phys. Rev. **D12** (1975) 147.

[81] E. Klempt and J.-M. Richard, *Baryon spectroscopy*, Rev. Mod. Phys. **82** (2010) 1095, arXiv:0901.2055.

[82] CLEO, M. Artuso *et al.*, *Observation of new states decaying into Lambda+(c) pi- pi+*, Phys. Rev. Lett. **86** (2001) 4479, arXiv:hep-ex/0010080.

[83] Belle, K. Abe *et al.*, *Experimental constraints on the possible J**P quantum numbers of the Lambda(c)(2880)+*, Phys. Rev. Lett. **98** (2007) 262001, arXiv:hep-ex/0608043.

[84] LHCb, R. Aaij *et al.*, *Observation of two new Ξ_b^- baryon resonances*, Phys. Rev. Lett. **114** (2015) 062004, arXiv:1411.4849.

[85] CMS collaboration, S. Chatrchyan *et al.*, *Observation of a new Ξ_b baryon*, Phys. Rev. Lett. **108** (2012) 252002, arXiv:1204.5955.

[86] M. Karliner, B. Keren-Zur, H. J. Lipkin, and J. L. Rosner, *The quark model and b baryons*, Annals Phys. **324** (2009) 2, arXiv:0804.1575.

[87] R. Lewis and R. M. Woloshyn, *Bottom baryons from a dynamical lattice QCD simulation*, Phys. Rev. **D79** (2009) 014502, arXiv:0806.4783.

[88] D. Ebert, R. N. Faustov, and V. O. Galkin, *Masses of heavy baryons in the relativistic quark model*, Phys. Rev. **D72** (2005) 034026, arXiv:hep-ph/0504112.

[89] X. Liu *et al.*, *Bottom baryons*, Phys. Rev. **D77** (2008) 014031, arXiv:0710.0123.

[90] E. E. Jenkins, *Model-independent bottom baryon mass predictions in the $1/N_c$ expansion*, Phys. Rev. **D77** (2008) 034012, arXiv:0712.0406.

[91] M. Karliner, *Heavy quark spectroscopy and prediction of bottom baryon masses*, Nucl. Phys. Proc. Suppl. **187** (2009) 21, arXiv:0806.4951.

[92] J.-R. Zhang and M.-Q. Huang, *Heavy baryon spectroscopy in QCD*, Phys. Rev. **D78** (2008) 094015, arXiv:0811.3266.

[93] Z.-G. Wang, *Analysis of the $\frac{3}{2}^+$ heavy and doubly heavy baryon states with QCD sum rules*, Eur. Phys. J. **C68** (2010) 459, arXiv:1002.2471.

[94] Z. S. Brown, W. Detmold, S. Meinel, and K. Orginos, *Charmed bottom baryon spectroscopy from lattice QCD*, Phys. Rev. **D90** (2014) 094507, arXiv:1409.0497.

[95] A. Valcarce, H. Garcilazo, and J. Vijande, *Towards an understanding of heavy baryon spectroscopy*, Eur. Phys. J. **A37** (2008) 217, arXiv:0807.2973.

[96] A. Limphirat, C. Kobdaj, P. Suebka, and Y. Yan, *Decay widths of ground-state and excited Ξ_b baryons in a nonrelativistic quark model*, Phys. Rev. **C82** (2010) 055201.

[97] LHCb, R. Aaij *et al.*, *Precision Measurement of the Mass and Lifetime of the Ξ_b^- Baryon*, Phys. Rev. Lett. **113** (2014) 242002, arXiv:1409.8568.

[98] LHCb, R. Aaij *et al.*, *Precision measurement of the mass and lifetime of the Ξ_b^0 baryon*, Phys. Rev. Lett. **113** (2014) 032001, arXiv:1405.7223.

[99] J. D. Jackson, *Remarks on the phenomenological analysis of resonances*, Nuovo Cim. **34** (1964) 1644.

[100] J. Blatt and V. Weisskopf, *Theoretical nuclear physics*, John Wiley & Sons, 1952.

[101] S. S. Wilks, *The large-sample distribution of the likelihood ratio for testing composite hypotheses*, Annals Math. Statist. **9** (1938) 60.

[102] BaBar collaboration, J. P. Lees *et al.*, *Measurement of the $D^*(2010)^+$ natural line width and the $D^*(2010)^+ - D^0$ mass difference*, Phys. Rev. **D88** (2013) 052003, Erratum ibid. **D88** (2013) 079902, arXiv:1304.5009.

[103] BaBar collaboration, J. P. Lees *et al.*, *Measurement of the $D^*(2010)^+$ meson width and the $D^*(2010)^+ - D^0$ mass difference*, Phys. Rev. Lett. **111** (2013) 111801, Erratum ibid. **111** (2013) 169902, arXiv:1304.5657.

[104] BaBar, B. Aubert *et al.*, *Measurement of the spin of the Omega- hyperon at BABAR*, Phys. Rev. Lett. **97** (2006) 112001, arXiv:hep-ex/0606039.

[105] BaBar, B. Aubert *et al.*, *Measurement of the Spin of the Xi(1530) Resonance*, Phys. Rev. **D78** (2008) 034008, arXiv:0803.1863.

[106] J. D. Richman, *An experimenter's guide to the helicity formalism*, , CALT-68-1148.

[107] LHCb collaboration, R. Aaij *et al.*, *Observation of a resonance in the $\Xi_b^-\pi^+$ mass spectrum*, LHCb-PAPER-2016-010, to be submitted to JHEP.

[108] LHCb, R. Aaij *et al.*, *Search for the doubly charmed baryon Ξ_{cc}^+*, JHEP **1312** (2013) 090, arXiv:1310.2538.

[109] LHCb, R. Aaij *et al.*, *Observation of $J/\psi p$ Resonances Consistent with Pentaquark States in $\Lambda_b^0 \to J/\psi K^- p$ Decays*, Phys. Rev. Lett. **115** (2015) 072001, arXiv:1507.03414.

[110] J.-R. Zhang and M.-Q. Huang, *Doubly heavy baryons in QCD sum rules*, Phys. Rev. **D78** (2008) 094007, arXiv:0810.5396.

[111] D.-H. He *et al.*, *Evaluation of spectra of baryons containing two heavy quarks in bag model*, Phys. Rev. **D70** (2004) 094004, arXiv:hep-ph/0403301.

[112] Z.-G. Wang, *Analysis of the $\frac{1}{2}^+$ doubly heavy baryon states with QCD sum rules*, Eur. Phys. J. **A45** (2010) 267, arXiv:1001.4693.

[113] D. Ebert, R. N. Faustov, V. O. Galkin, and A. P. Martynenko, *Mass spectra of doubly heavy baryons in the relativistic quark model*, Phys. Rev. **D66** (2002) 014008, arXiv:hep-ph/0201217.

[114] V. V. Kiselev and A. K. Likhoded, *Baryons with two heavy quarks*, Physics-Uspekhi **45** (2002), no. 5 455.

[115] A. P. Martynenko, *Ground-state triply and doubly heavy baryons in a relativistic three-quark model*, Phys. Lett. **B663** (2008) 317, arXiv:0708.2033.

[116] S. S. Gershtein, V. V. Kiselev, A. K. Likhoded, and A. I. a. Onishchenko, *Spectroscopy of doubly heavy baryons*, Phys. Rev. **D62** (2000) 054021.

[117] D. B. Lichtenberg, R. Roncaglia, and E. Predazzi, *Mass sum rules for singly and doubly heavy flavored hadrons*, Phys. Rev. **D53** (1996) 6678, arXiv:hep-ph/9511461.

[118] C.-H. Chang, C.-F. Qiao, J.-X. Wang, and X.-G. Wu, *Estimate of the hadronic production of the doubly charmed baryon Xi(cc) under GM-VFN scheme*, Phys. Rev. **D73** (2006) 094022, arXiv:hep-ph/0601032.

[119] C. C. Hsi, L. Tong, L. Xue-Qian, and W. Yu-Ming, *Lifetime of doubly charmed baryons*, Communications in Theoretical Physics **49** (2008), no. 4 993.

[120] V. V. Kiselev, A. K. Likhoded, and A. I. Onishchenko, *Lifetimes of doubly charmed baryons: Xi(cc)+ and Xi(cc)++*, Phys. Rev. **D60** (1999) 014007, arXiv:hep-ph/9807354.

[121] B. Guberina, B. Melić, and H. Štefančić, *Inclusive decays and lifetimes of doubly-charmed baryons*, The European Physical Journal C-Particles and Fields **9** (1999), no. 2 213.

[122] SELEX collaboration, M. Mattson *et al.*, *First observation of the doubly charmed baryon Ξ_{cc}^+)*, Phys. Rev. Lett. **89** (2002) 112001, arXiv:hep-ex/0208014.

[123] SELEX collaboration, A. Ocherashvili *et al.*, *Confirmation of the double charm baryon $\Xi_{cc}^+(3520)$ via its decay to pD^+K^-*, Phys. Lett. **B628** (2005) 18, arXiv:hep-ex/0406033.

[124] S. P. Ratti *et al.*, *New results on c-baryons and a search for cc-baryons in FOCUS*, Nuclear Physics-Section B-PS-Proceedings Supplements **115** (2003) 33.

[125] BaBar collaboration, B. Aubert *et al.*, *Search for doubly charmed baryons Ξ_{cc}^+ and Ξ_{cc}^{++} in BaBar*, Phys. Rev. **D74** (2006) 011103, arXiv:hep-ex/0605075.

[126] Belle collaboration, R. Chistov *et al.*, *Observation of new states decaying into $\Lambda_c^+ K^- \pi^+$ and $\Lambda_c^+ K_S^0 \pi^-$*, Phys. Rev. Lett. **97** (2006) 162001, arXiv:hep-ex/0606051.

[127] LHCb, R. Aaij *et al.*, *Observation of J/ψ pair production in pp collisions at $\sqrt{s} = 7TeV$*, Phys. Lett. **B707** (2013) 52, arXiv:1109.0963.

[128] LHCb, R. Aaij *et al.*, *Observation of double charm production involving open charm in pp collisions at $\sqrt{s}$ = 7 TeV*, JHEP **06** (2012) 141, arXiv:1205.0975, [Addendum: JHEP03,108(2014)].

[129] J. P. Ma and Z. G. Si, *Factorization approach for inclusive production of doubly heavy baryon*, Phys. Lett. **B568** (2003) 135, arXiv:hep-ph/0305079.

[130] C.-H. Chang, J.-P. Ma, C.-F. Qiao, and X.-G. Wu, *Hadronic production of the doubly charmed baryon Ξ_{cc} with intrinsic charm*, J. Phys. **G34** (2007) 845, arXiv:hep-ph/0610205.

[131] C. H. Chang, J. X. Wang, and X. G. Wu, *GENXICC2. 0: An upgraded version of the generator for hadronic production of double heavy baryons Ξ_{cc}, Ξ_{bc} and Ξ_{bb}*, Computer Physics Communications **181** (2010), no. 6 1144.

[132] L. Lyons, *Open statistical issues in Particle Physics*, Ann. Appl. Stat. **2** (2008) 887.

[133] A. L. Read, *Presentation of search results: The CL(s) technique*, J. Phys. **G28** (2002) 2693.

[134] G. Cowan, K. Cranmer, E. Gross, and O. Vitells, *Asymptotic formulae for likelihood-based tests of new physics*, Eur. Phys. J. **C71** (2011) 1554, arXiv:1007.1727.

[135] Fermilab Lattice, MILC, A. Bazavov *et al.*, *$B_{(s)}^0$-mixing matrix elements from lattice QCD for the Standard Model and beyond*, arXiv:1602.03560.

[136] LHCb, CMS, V. Khachatryan *et al.*, *Observation of the rare $B_s^0 \to \mu^+\mu^-$ decay from the combined analysis of CMS and LHCb data*, Nature **522** (2015) 68, arXiv:1411.4413.

[137] LHCb, R. Aaij *et al.*, *Determination of the quark coupling strength $|V_{ub}|$ using baryonic decays*, Nature Phys. **11** (2015) 743, arXiv:1504.01568.

[138] LHCb, T. L. Collaboration, *Angular analysis of the $B^0 \to K^{*0}\mu^+\mu^-$ decay*, .

[139] LHCb, R. Aaij *et al.*, *Measurement of Form-Factor-Independent Observables in the Decay $B^0 \to K^{*0}\mu^+\mu^-$*, Phys. Rev. Lett. **111** (2013) 191801, arXiv:1308.1707.

[140] LHCb, R. Aaij *et al.*, *Test of lepton universality using $B^+ \to K^+\ell^+\ell^-$ decays*, Phys. Rev. Lett. **113** (2014) 151601, arXiv:1406.6482.

[141] LHCb, R. Aaij *et al.*, *Measurement of the ratio of branching fractions $\mathcal{B}(\bar{B}^0 \to D^{*+}\tau^-\bar{\nu}_\tau)/\mathcal{B}(\bar{B}^0 \to D^{*+}\mu^-\bar{\nu}_\mu)$*, Phys. Rev. Lett. **115** (2015) 111803, arXiv:1506.08614, [Addendum: Phys. Rev. Lett. 115, 159901 (2015)].

[142] LHCb, R. Aaij *et al.*, *Observation of the resonant character of the $Z(4430)^-$ state*, Phys. Rev. Lett. **112** (2014) 222002, arXiv:1404.1903.

[143] LHCb Collaboration, R. Aaij *et al.*, *Implications of LHCb measurements and future prospects*, Eur. Phys. J. **C73** (2013) 2373, arXiv:1208.3355.

[144] T. Aushev *et al.*, *Physics at Super B Factory*, arXiv:1002.5012.

[145] V. V. Gligorov *et al.*, *Swimming: A data driven acceptance correction algorithm*, J. Phys. Conf. Ser. **396** (2012) 022016.

[146] LHCb, R. Aaij *et al.*, *Study of $B^0_{(s)} \to K^0_S h^+ h'^-$ decays with first observation of $B^0_s \to K^0_S K^\pm \pi^\mp$ and $B^0_s \to K^0_S \pi^+\pi^-$*, JHEP **10** (2013) 143, arXiv:1307.7648.

[147] C. Smith, *Proton stability from a fourth family*, Phys. Rev. **D85** (2012) 036005, arXiv:1105.1723.

[148] G. Durieux, J.-M. Gerard, F. Maltoni, and C. Smith, *Three-generation baryon and lepton number violation at the LHC*, Phys. Lett. **B721** (2013) 82, arXiv:1210.6598.